Fabricio de Abreu Bozzi

Vector Sensors for Underwater Acoustic Communications

Fabricio de Abreu Bozzi

Vector Sensors for Underwater Acoustic Communications

Ph.D. Thesis in Electronics and Telecommunications (Signal Processing)

Developed under supervision of:

Prof. Sérgio Manuel Machado Jesus

UAlg FCT
UNIVERSIDADE DO ALGARVE
FACULDADE DE CIÊNCIAS E TECNOLOGIA

UNIVERSITY OF ALGARVE

FACULTY OF SCIENCES AND TECHNOLOGY

2022

Vector Sensors for Underwater Acoustic Communications

Declaração de autoria do trabalho

Declaro ser o autor deste trabalho, que é original e inédito. Autores e trabalhos consultados estão devidamente citados no texto e constam da listagem de referências bibliográficas incluída.

Fabricio de Abreu Bozzi

To Lorana

&

To my parents

Acknowledgements

Name:	Fabricio de Abreu Bozzi
College:	Faculty of Sciences and Technology
University:	University of Algarve
Supervisor:	Sérgio Manuel Machado Jesus, Full Professor at the Faculty of Sciences and Technology, University of Algarve
Thesis title:	Vector sensors for underwater acoustic communications

Abstract

Acoustic vector sensors measure acoustic pressure and directional components separately. A claimed advantage of vector sensors over pressure-only arrays is the directional information in a collocated device, making it an attractive option for size-restricted applications. The employment of vector sensors as a receiver for underwater communications is relatively new, where the inherent directionality, usually related to particle velocity, is used for signal-to-noise gain and intersymbol interference mitigation. The fundamental question is how to use vector sensor directional components to benefit communications, which this work seeks to answer and to which it contributes by performing: analysis of acoustic pressure and particle velocity components; comparison of vector sensor receiver structures exploring beamforming and diversity; quantification of adapted receiver structures in distinct acoustic scenarios and using different types of vector sensors. Analytic expressions are shown for pressure and particle velocity channels, revealing extreme cases of correlation between vector sensors' components. Based on the correlation hypothesis, receiver structures are tested with simulated and experimental data. In a first approach, called vector sensor passive time-reversal, we take advantage of the channel diversity provided by the inherent directivity of vector sensors' components. In a second approach named vector sensor beam steering, pressure and particle velocity components are combined, resulting in a steered beam for a specific direction. At last, a joint beam steering and passive time-reversal is proposed, adapted for vector sensors. Tested with two distinct experimental datasets, where vector sensors are either positioned on the bottom or tied to a vessel, a broad performance comparison shows the potential of each receiver structure. Analysis of results suggests that the beam steering structure is preferable for shorter source-receiver ranges, whereas the passive time-reversal is preferable for longer ranges. Results show that the joint beam steering and passive time-reversal is the best option to reduce communication error with robustness along the range.

Keywords: Vector sensors, underwater acoustic communications, directional sensors, underwater acoustics.

Nome: Fabrício de Abreu Bozzi
Faculdade: Faculdade de Ciências e Tecnologia
Universidade: Universidade do Algarve
Orientador: Sérgio Manuel Machado Jesus, Professor Catedrático da Faculdade de Ciências e Tecnologia, Universidade do Algarve
Título da Tese: Sensores vetoriais para comunicações acústicas submarinas

Resumo

Sensores vetoriais acústicos (em inglês, *acoustic vector sensors*) são dispositivos que medem, além da pressão acústica, a velocidade de partícula. Esta última, é uma medida que se refere a um eixo, portando, está associada a uma direção. Ao combinar pressão acústica com componentes de velocidade de partícula pode-se estimar a direção de uma fonte sonora utilizando apenas um sensor vetorial. Na realidade, "um" sensor vetorial é composto de um sensor de pressão (hidrofone) e um ou mais sensores que medem componentes da velocidade de partícula. Como podemos notar, o aspecto inovador está na medição da velocidade de partícula, dado que os hidrofones já são conhecidos. As duas tecnologias mais utilizados para medição da velocidade de partícula são: via gradiente de pressão ou via sensores inerciais, onde a primeira provem uma estimativa e a segunda uma medida verdadeira. A partir destes tipos de tecnologias, dão-se os nomes mais conhecidos dos sensores vetoriais, chamados de *pressure-gradient* ou *accelerometer-based vector sensors*. Obviamente que cada tecnologia possui vantagens e desvantagens, mas resumidamente, pode-se dizer que o modelo baseado em gradiente de pressão é mais adequado para instalações fixas, dado que ele é mais imune ao movimento e ao ruído de arraste, enquanto que sua faixa dinâmica de operação é limitada. Por outro lado, os baseados em acelerômetros possuem uma banda de operação mais ampla e são frequentemente utilizados para baixa frequência ($< 1\,\text{kHz}$), mas possuem problemas de ruído de arraste, por isso são mais adequados para instalações como em boias à deriva.

A partir da compreensão básica dos sensores vetoriais, que como percebemos, consiste na informação direcional "extra", resta perguntar como tirar proveito desta informação para as comunicações. O problema das comunicações consiste na baixa relação sinal ruído (SNR), que está relacionado com a atenuação do sinal transmitido ao longo do meio, ou seja, a perda por propagação, e na interferência intersimbólica (ISI), que está relacionado com a distorção que o canal acústico causa no sinal recebido. A literatura tem mostrado que os componentes de pressão e velocidade de partícula tem sido utilizados de forma independentes em estruturas "padrões" de comunicação. Observou-se que como os canais direcionais estão arranjados de forma ortogonal, os sinais recebidos podem ser diversos, em amplitude e fase, o que lembra o conceito de diversidade espacial, já utilizado em arranjos de sensores de pressão. Portanto, de forma similar, a ideia é que quanto mais diversos e maior o número canais disponíveis, maior a probabilidade de recuperar e decodificar o sinal recebido. Entretanto, o que ainda não se compreende completamente é como explicitamente tirar proveito dos canais direcionais. Neste sentido questiona-se, qual abordagem utilizar, seja via filtro casado (ou combinação passiva de tempo reverso), ou equalizadores de múltiplos canais, ou conformação de feixes. Outro aspecto que se coloca se refere às estruturas receptoras já utilizadas para arranjos de pressão que poderiam ser propriamente adaptadas para as características dos componentes direcionais. Além disso, as vantagens ou limitações de cada método ainda não foram comparativamente demonstradas. Portanto, estas questões elencadas serviram de

base para o desenvolvimento do doutorado, que tencionou a responder, ainda que de forma particular, cada uma delas.

Em uma primeira fase, e de forma a convencionar nomenclaturas e definições usadas para os sensores vetoriais, conceitos de medição ou estimação da velocidade de partícula, e diretividade dos sensores vetoriais são abordados. Esta fundamental abordagem, dirigida somente para sensores vectoriais, é seguida pelos desafios dos sistemas de comunicações para com canais submarinos. Desta forma, uma abordagens estatística dos componentes dos sensores vetoriais é feita para um caso de estudo para águas rasas. Baseado nas particularidades dos canais direcionais, analisados via correlação, estruturas receptoras são apresentadas.

Dentre variadas opções de estruturas receptoras, este trabalho se restringiu a três: combinação passiva de tempo reverso (passive time-reversal, PTR); conformação de feixes rotacionada (beam steering); e a combinação destas últimas duas. A estrutura PTR testada, embora com algumas modificações nos estágios de processamento, baseia-se no PTR convencional, e é utilizada como referência. Esta estrutura é apresentada como uma forma de se explorar o ganho de diversidade nos cenários onde os componentes apresentem baixa correlação. A segunda estrutura baseia-se na conformação de feixes, onde a ideia é explorar componentes altamente correlacionados e prover um aumento de SNR. Nesta estrutura, quando o sensor vetorial possui componente vertical, três diferentes saídas são geradas de forma a realçar a correlação. Por último, a estrutura conjunta tende a explorar ambos cenários de correlação, que em dados experimentais podem apresentar uma correlação intermediária. Esta estrutura conjunta é adaptada, onde os componentes horizontais do sensor vetorial são ponderados para o PTR de acordo com a informação da direção estimada da fonte. Desta forma, pretende-se atenuar possíveis componentes ruidosos, além de ter a combinação das saídas do beam steering e do PTR feitas por um equalizador de múltiplos canais.

Dados de dois experimentos de campo utilizando os dois tipos de sensores vetoriais são utilizados para quantificar e validar as referidas estruturas. Em um primeiro experimento (MakaiEx), utiliza-se um arranjo de sensor vetoriais baseado em acelerômetros amarrado a um navio à deriva e uma fonte sonora de fundo transmitindo sinais de comunicações. Uma simulação prévia deste cenário acústico utilizando modelagem numérica mostrou que a estrutura beam steering poderia ser vantajosa em curtas distância ($<300\,\mathrm{m}$) enquanto a baseada no PTR para distâncias maiores. Com aproximada aderência, esta relação foi verificada com os dados reais do MakaiEx. Além disso, os resultados de desempenho foram bastante satisfatórios quando utilizada a estrutura conjunta, onde o erro de bit foi reduzido aproximadamente dez vezes, comparado com as estruturas individuais. A usual comparação com um arranjo de sensores de pressão também é feita, onde se demonstrou que um único sensor vetorial pode superar o desempenho de um arranjo de $40\,\mathrm{cm}$ com quatro sensores de pressão. Entretanto, mostra-se que o método conjunto alcança um desempenho ainda melhor.

O segundo experimento (EMSO) contou com um sensor vetorial baseado a gradiente de pressão posicionado no fundo do mar com uma fonte sonora amarada a um navio. O desempenho das estruturas receptoras foi quantificado para diversas distâncias e direções, onde foi possível analisar a capacidade de focalização dos sensores vetoriais nos quatro quadrantes geográficos. Um constante ganho de desempenho foi notado para a estrutura beam steering mostrando robustez e indicando que o desempenho poderia ser previsto em diferentes cenários acústicos. A estrutura combinada apresentou o melhor desempenho para todas as estações de transmissão, o que indicou o beneficio de se ponderar os canais do PTR com a informação da direção da fonte.

Com base nas análises teóricas e resultados com dados simulados e experimentais o presente trabalho mostrou evidências para defender:

- Os componentes dos sensores vetoriais podem ser explorados via diversidade ou formação de feixes, embora explorar os dois em conjunto gerou o melhor desempenho.

- A estrutura que utiliza o método PTR tem seu melhor desempenho quando os componentes são diversos, ou descorrelacionados, e desempenho reduzido ao beam steering quando os componentes são relacionados. Entretanto, imprecisões na estimação da resposta ao impulso do canal, e variação do mesmo, degrada seu desempenho, onde a estrutura beam steering é então preferível.

- A utilização de um único sensor vetorial pode alcançar desempenho similar ou superior a um pequeno arranjo de sensores de pressão. Embora tal comparação dependa da característica geométrica do arranjo de sensores de pressão, é seguro afirmar o benefício em termos de tamanho. Além disso, é verificado que estruturas adaptadas para sensores vetoriais pode prover melhores desempenhos comparadas as estruturas padrões.

- Interpretações da diversidade de canais dos sensores vetoriais como sendo diversidade espacial, pode não ser adequada. A ortogonalidade dos componentes que são inerentemente direcionais pode ser a melhor forma de compreensão.

- O uso da informação da direção da fonte, via estimativa da direção de chegada, se mostrou vantajosa. Esta informação é utilizada na estrutura beam steering e na estrutura conjunta. Enquanto que na estrutura beam steering o desempenho é relacionado com a capacidade de focalização, na estrutura conjunta a ponderação dos componentes horizontais dão mais peso aos componentes voltados para a direção da fonte. É notado que ao utilizar um sensor vetorial 3D, a utilização da estimativa de elevação não reduz o erro, além do ângulo de elevação não ser estimado com acurácia. Por outro lado um incremento da SNR e consequente redução do erro é verificada ao focalizar à direção da fonte no plano horizontal.

Por fim, este trabalho tende a contribuir nos seguintes aspectos:

- Reforça o propício uso dos componentes direcionais do sensor vetorial, onde a correlação entre pressão acústica e velocidade de partícula ajuda na compreensão e como combinar vantajosamente os componentes em estruturas receptoras

- Propõem uma estrutura conjunta, adaptada para sensor vetoriais, e a compara com estruturas padrões. É possível verificar que estruturas adaptadas apresentam melhor desempenho que um arranjo pequeno de pressão e estruturas padrões.

- Mostra uma ampla comparação, utilizando um único sensor vetorial ou combinando vários sensores vetoriais. Dois diferentes tipos de sensores vetoriais em dois diferentes experimentos são investigados.

Palavras-chave: Sensor vetorial, comunicações acústicas submarinas, sensores direcionais, acústica submarina.

Contents

List of Figures

List of Tables

Chapter 1

Introduction

***Synopsis**: This chapter discusses about underwater acoustic communications and acoustic vector sensors, describing the state of the art, the motivation, challenges, and perspectives of using vector sensors for communications. Section 1.1 presents the state of the art, first treating communications and vector sensors separately, then showing how researchers have been taking advantage of vector sensors to benefit communications. Section 1.2 presents the work's motivation, challenges, objectives, and open questions that this work intends to address. Finally, section 1.3 presents the thesis organization.*

A healthy ocean is fundamental for supporting life on our planet. Recent advances in ocean exploration are crucial for understanding how society may use resources in a sustainable way. The trade-off between ocean exploitation and marine life biodiversity conservation is not easy to be established since many geo-strategic and economic interests are at play. In recent years, we have seen a boost in engineering innovation, ranging from robotics to remote sensing, which may contribute to sustainable exploitation under rigorous monitoring in order to minimize the impacts of human activities. However, compared to land, large regions of the ocean are still unknown because of harsh conditions, great depths, and because
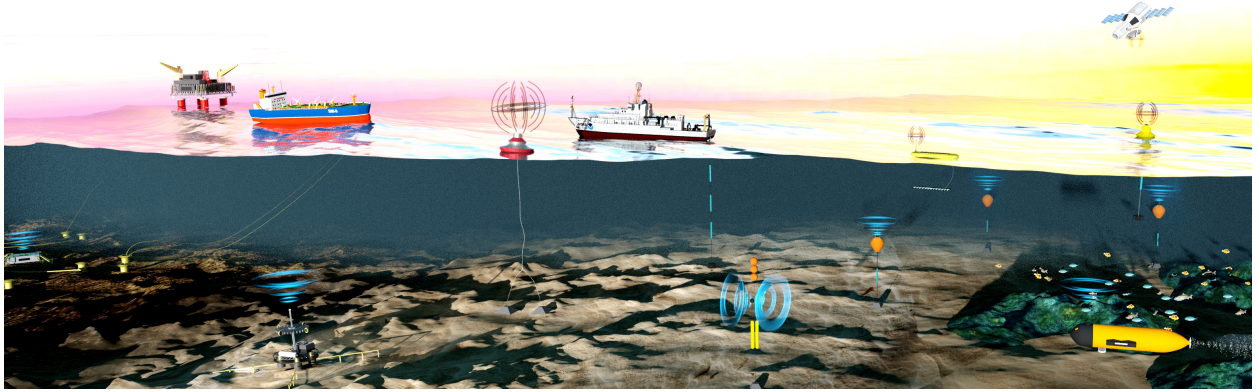
Figure 1.1: Ocean assets (from left to right): an oil and gas extraction system with bottom pipelines, a floating platform, and an oil tanker ship; a tsunami alarm system with bottom geophones and surface buoy; a research vessel with a towed array of acoustic sensors; bottom-moored and surface-drifting buoys with acoustic sensors; wave-glider; autonomous underwater vehicle; satellite.

these regions are remote and vast. Whereas airborne remote sensing technology provides synoptic information about the ocean surface (or a thin layer beneath it), the ocean interior is largely unexplored and uncharted. Therefore, the water column, the ocean bottom, and the support conditions for marine life can only be effectively monitored through arrays of distributed in-situ platforms, sensors, and probes.

Figure 1.1 shows a non-exhaustive range of platforms and instruments, many of which have dual use for both ocean exploration/exploitation and environmental monitoring or early warning. A common characteristic of most of these systems is that they need power and capabilities to send and receive data. Connectivity through communications enables downlink information for command and control and uplink of in-situ biological, chemical, physical, and archaeological parameters or images. Depending on horizontal distances, underwater sensors may now form small networks where platforms are network nodes. Underwater, point-to-point communications may be based on electromagnetic waves in centimeters of range, optical transducers at tens of meters, or acoustic waves at 100 meters, kilometers,

or more. Generally, at practical horizontal distances and from bottom to surface (or vice-versa), reliable communications require underwater acoustics since only acoustic waves travel appreciable distances underwater.

Underwater acoustics (UWA) is the science of sound in water, investigating how sound (the pressure field) propagates and interacts with the surface and bottom boundaries [1]. It has been demonstrated that, for the underwater medium, electromagnetic waves are entirely extinguished in a few meters, so sound is preferred for long-range transmission. In ocean shallow water, roughly speaking for water depths $< 200\,\mathrm{m}$, and except for very low frequencies (e.g.,$<10\,\mathrm{Hz}$), the ocean behaves as an acoustic waveguide, bounded by the sea surface and bottom, whose boundary interaction may cause severe attenuation and interference in the sound wave [2]. Conversely, in deep water, the upward refracting sound speed profile ensures that fewer acoustic paths reach the seabed, where they would lose energy to penetration into the seabed, which enables extremely long range propagation. Thus, it is important to note that designing an underwater system, the understanding of UWA is crucial. The simple direct transfer of airborne techniques to the underwater acoustic domain is expected to fail due to how sound propagates through the underwater medium, referred to as the underwater channel.

Wireless underwater acoustic communication (UWAC) is an important tool in ocean exploration, facilitating underwater platform operation and contributing to efficient data collection. Experts in communications used to say that UWAC is one of the most challenging fields, where low data rates and high bit error are unavoidable. Basically, the underwater channel distorts and attenuates the transmitted message, and the communication system should compensate for such impacts on the receiver in order to recover the message. Several

techniques to cope with the underwater channel and improve communications performance have been proposed [3]. Using arrays of pressure sensors is a classical way that explores spatial filtering capabilities. However, it is already known that the performance depends on the array geometry, which usually requires deploying several sensors along the water column. Thus, considering the recently increased usage of unmanned underwater platforms, which require light, compact, and power-efficient acoustic sensors, long arrays may not be the preferable solution. In general, small vehicles/underwater stations are able to employ only one or a few acoustic sensors as part of acoustic modems.

Acoustic modems are devices able to transmit and receive information among submerged underwater platforms and surface assets, which may be organized in a communication network topology [4]. These devices can be posed on the seafloor, attached to mooring buoys, or onboard moving platforms. Moreover, they may carry one transducer, which transmits and receives the signal, or may have one transducer, acting as a projector, and one hydrophone as the receiver [5]. However, considering the use of a single omnidirectional hydrophone (scalar measurement) in the modem reception stage, no spatial filtering capability can be obtained, and the performance may be limited, e.g., by not exploring a directional gain. Thus, an attractive option is to use sensors that respond to a vector measure of the acoustic field, called acoustic vector sensors.

The generic term "vector sensor (VS)" refers to a device that provides directional components related to their measured axis, additionally to acoustic pressure. The directional components usually come from the measurement of particle motion, velocity, or acceleration, along one, two, or three axes. Providing multiple components, beamforming or diversity methods can be adapted to vector sensor components, exploring now a steerable directional

gain or diversity of individual directional components. Thus, using a vector sensor in acoustic modems is a solution that fits the tendency of compactness with a performance gain provided by directional components. The following section shows a historical perspective regarding the use of vector sensors and underwater communications.

1.1 State of the art

This section presents three topics: underwater acoustic communications, applications of vector sensors for underwater acoustics, and vector sensors for underwater communications.

1.1.1 Underwater acoustic communications

The challenge in underwater acoustic communications (UWAC) consists of achieving the highest possible data rate, according to the objective of robustness and range. In the past, the navy financed most UWAC studies due to the need for communication with submerged submarines [6]. However, with the Oil & Gas industry expansion, the use of underwater communication became prominent for controlling and monitoring equipment and systems. In this field, acoustic modems are preferable to cables due to the ease of deployment, flexibility, and maintenance. Moreover, applications in marine research, oceanography, and geology have included modems on board of unmanned underwater platforms (UUVs), seafloor stations, and earthquake monitoring systems for tsunami warning. Thus, we can notice that such applications require underwater communications systems that go from transmitting a simple control signal (e.g., on/off command) to a real-time video.

A notable review paper in the 80s presents the achievements in the UWAC for high data rate transmission, which at that time refers to rates about a few kilobits/s [6]. The issues

related to the available bandwidth and reverberation reveal challenges of UWAC, still present nowadays. Underwater channels have a limited bandwidth due to the absorption in high-frequency (>10 kHz) and long-range low-frequency (anthropogenic and ambient,<2 kHz) noise. Reverberation due to the surface-bottom backwave interaction and surface turbulence reduces the available bandwidth, also limiting the communicating data rate. The modest data rate, varying from 10 bit/s in shallow water to 1 kbit/s in deep water, was published in the ages where non-coherent frequency shift keying (FSK) modulation was predominant [6].

The underwater channel temporal variability (time-varying channels) is another issue that impacts the design of a communication system. Time-varying channels are due to the sound propagation changes and also the source-receiver dynamic (Doppler effect). Improvements to cope with the channel variability in short (<1 km), medium, and long ranges (20-2000 km) focused on synchronization issues [7]. Synchronization in a multipath environment is a complicated task. Since the sound wave reaches the receiver through many paths of distinct lengths, the transmitted signal arrives at the receiver at different times, and with different amplitudes and phases. The difficulty arises because there is not always a discernible principal arrival. Hence, the initial timing can be represented in several ways, such as the first or largest arrival, or the average of some most energetic arrivals. Thus, since the synchronization choice impacts the receiver performance, a joint synchronization and equalization is proposed, where an adaptive Kalman equalizer is implemented [7]. Although recognized as a fast converging equalizer (10 interactions to converge), when tested with experimental data, the rapid changes in the underwater channel and source-receiver fluctuation result in poor performance, from which solution exploring diversity techniques has started to be investigated.

The basic idea of diversity is to replicate the same information at the receiver. It is also interpreted as a redundancy technique [3]. Time diversity is achieved by transmitting the same signal in different and appropriate time slots. This technique is straightforward, whereas it causes the reduction of the effective transmission rate due to the repetition of the information in time.

Another option takes advantage of frequency diversity, where different carriers transmit the same information. Frequency diversity induces an efficient intersymbol interference (ISI) mitigation, resulting from the multiple arrivals at different times, in which one symbol interferes with the subsequent symbol. However, frequency diversity may cause two problems: a power inefficiency caused by possible high peak-to-average of the transmitted signal; and non-efficient bandwidth usage.

Besides time and frequency diversities, spatial diversity is presented as a promising approach to improve the reliability in UWAC [8]. As the underwater environment has limited bandwidth and the designed system may be power limited, a multichannel receiver provides more information. In other words, spatial diversity provides copies of the same information, modified by independent paths. The communication performance depends on the number of transmitters and receivers, which have to be more than one. Combining multiple channels may result in both an increase in signal-to-noise ratio (SNR) and ISI mitigation. Thus, the use of hydrophone arrays as a receiver, forming a single-input multiple-output (SIMO) system, has started to be adopted extensively in UWAC since the 90s. Moreover, the employment of coherent modulation schemes in the underwater environment has shown to be a possibility.

Coherent modulation is an attractive option in band-limited channels due to efficient

bandwidth usage. A simple way to see this efficiency comes from the ratio of the bit rate over the bandwidth $r = \frac{2log_2 M}{N}$, where M is the constellation size and N is the dimensionality of the constellation [3]. For M-phase shift keying (PSK), N = 2, and the bandwidth efficiency increases as M increases. On the other hand, for M-FSK, $r = \frac{2log_2 M}{M}$, so, as M increases the bandwidth efficiency decreases. Thus, coherent modulation increases bandwidth efficiency, which makes it preferable for underwater systems if the objective is to improve the data rate. However, temporal channel variability causes strong phase fluctuation, which may be prohibitive for coherent modulation due to the phase tracking error. Besides channel variability, ISI increases with higher rates, if the symbol periods become shorter. Thus, various studies have proposed different approaches integrating coherent modulation with optimized phase tracking and synchronization, and adaptive multichannel combining by using multichannel decision feedback equalizer (DFE) or passive time-reversal (PTR) [9, 10, 11, 12, 13, 14].

The theory and the experimental results have shown the advantage of using an efficient bandwidth signal modulation, which makes it possible to achieve higher data-rate than those found in non-coherent modulation [9, 10]. One of the proposed receivers' shortcomings is the system's complexity related to signal processing. Phase tracking and synchronization require a well-calibrated second-order phase-locked loop (PLL), and a known channel probe is necessary for channel estimation, limiting the effective data rate [11]. Another shortcoming is the employment of long arrays, where deployment logistics and maintenance usually require a large vessel. However, when using an array of pressure sensors, beamforming or passive-time reversal methods may take advantage of array gain or diversity gain.

In this context, the passive time-reversal approach, also called phase-conjugation when

performed in frequency domain, has been widely investigated in UWAC [12, 15, 16, 17]. The idea of "active" time reversal is to transmit a signal from a sound source and receive this signal in an array. Then, the received signal in each element of the array is time-reversed and transmitted back. This procedure, based on sound propagation reciprocity, causes a retro-focusing at the source location [18]. In the "passive" version, play-back is performed synthetically by software or hardware [17]. The method is computationally simple, although channel estimation, equalization, and phase tracking algorithms are usually necessary [14, 15]. In the PTR classical form, it is assumed that the underwater channel does not change between the moment the probe is received and information carrying signal is received, which may not be guaranteed due to temporal variability and source-receiver movement. Thus, performance can be severely degraded if channels' coherence time is short compared to the demodulated packet duration [12]. A recursive procedure to track the channel fluctuation was proposed, where satisfactory experimental results were presented for small channels' fluctuations [14].

Since the pressure-sensor array geometry directly impacts communication performance, a rich investigation relating coherence and the array geometry was performed by Yang [13]. The use of beamforming is found to be preferable for small arrays, where channel correlation is high. In contrast, diversity is better explored for largely-spaced arrays, where the channel correlation may be low. The same author compares the passive time-reversal to multichannel DFE [12]. The DFE is a nonlinear equalizer that cancels contributions of previously detected symbols to current symbol in order to eliminate ISI, using an estimate of the channel impulse response function. The channel can be estimated wither from known "pilot" symbols used in an initial probe sequence (in a "training" mode), or previously detected information

symbols (in a decision directed mode). It is considered a practical equalizer, although it is not optimum in the sense of minimizing the probability of error in the detector. Theoretical and at-sea results show that the DFE usually outperforms the PTR when the number of sensors is small, although a correct filter setting is necessary for convergence, and the performance may vary depending on the channel time spread.

Whereas SIMO systems using DFE and PTR have been tested at sea, during the last decade, studies have also shown successfully experimental results of airborne modulation schemes, such as orthogonal frequency-division multiplexing (OFDM) employed underwater [19, 20, 21]. Indeed, the recent high-performance low-power computing technology greatly impacts the advance of such techniques, which, previously, were only suited to specialized hardware, such as digital signal processors (DSPs) and field programmable gate arrays (FPGAs). An example is the frequency-hopped JANUS modulated signal, which has advantages regarding standardization and interoperability, counting yet with open-source codes, i.e., it can be easily implemented on hardware of opportunity [22, 23, 24]. Thus, with a mature interoperability standard for the underwater acoustic physical layer, new applications arise, where acoustic modems are required to work integrated into networks of fixed or mobile nodes. The new directions for the next generation of underwater wireless technologies may face four priorities: applications, physical layer, networks, and implementation [25].

Regarding emerging applications, the increase usage of UUVs and autonomous underwater vehicles (AUVs) has demanded intelligent solutions. For those mobile assets, long-range communication allows guidance, status updates, and sharing on-the-fly sensors' information [26, 27]. Mobile platforms are also restricted in size, weight, and energy consumption, which explains why many do not employ acoustic communications on board and, when they

do, these are based on very simple low-power single transducer modems [5]. Thus, it is clear that a focused design for those mobile platforms is necessary. Regarding the physical layer, standardization in the statistical channel modeling is still necessary, where typical and categorized channels could be directly employed to test structure performance. Solutions have already been proposed, such as channel sounding [28, 29]. This method consists of in-situ estimation of the channel impulse response, which is then used as a replay of the underwater channel. Although the replay-based method can represent the environment with fair accuracy, the channel catalog is still limited [29]. Regarding networks, several works have proposed and employed underwater protocols. However, the lack of understanding of which scenario favors which architecture still restricts its usage. Open-access data and benchmark applications could mitigate such issues. Finally, the implementation of acoustic communications systems has been greatly favored by the leap in computing technology, although, in terms of transducer technology, most of the research persists on conventional acoustic pressure sensors (omnidirectional hydrophones). Thus, by exploring vector sensors for underwater communications, the present work contributes especially to the advance of emerging applications and for the progress of solutions that use different transduction mechanisms.

1.1.2   Vector sensors for underwater acoustics

The development of electromechanical devices, which can measure pressure and particle velocity of the acoustic field, dates back to the 30s. At that time, Olson [30] presented a study of a ribbon microphone. The microphone was designed to measure a body displacement that was proportional to the particle motion. The device was based on a suspended baffled ribbon suspended in a magnetic field. The pressure difference on each side of the ribbon

resulted in a sensitive measurement of the sound wave direction, i.e., a directional pattern. This device, called velocity microphone, is the basis of recent microphones used in audio studios and on stage, where it is required high-quality, flat frequency response in the audible band, and mitigation of audience noise.

For the underwater environment, Leslie et al. [31] presented a neutrally buoyant inertial sensor in 1956. In this study, mathematical expressions were derived for the motion of a rigid uniform sphere in an underwater sound field. The idea was to show that the velocity of a rigid neutrally buoyant sphere was equal to the particle velocity when the sphere was moving in the water. A velocity sensor, a magnetic structure with a moving coil, was fixed inside the sphere. The experimental result showed a dipole directionality for frequencies below 2 kHz. This device, also called velocity hydrophone, was probably the precursor of practical vector sensors for underwater acoustics.

The wide use of vector sensors in underwater acoustic applications was first seen in directional frequency analysis and recording (DIFAR) sonobuoy in the 60s [32]. Measuring particle velocity components in the 2D horizontal plane, a DIFAR sonobuoy is a device developed to detect and classify underwater sources. Usually, this sonobuoy is launched by a helicopter or a ship, which receives and analyzes the acoustic data remotely via a radio link. Generally, the acoustic data come from one or a few vector sensors immersed in the ocean by a cable attached to a drifting buoy.

Employed by the US Navy for undersea warfare, this device presents several benefits compared to the conventional sonar of surface ships. The first is the negligible self-noise since the sonobuoy is drifting freely. Second is the low-frequency ($< 1 \, \text{kHz}$) directional capability of vector sensors, which is useful for both detection and classification. Moreover, ambiguity

problems presented in line arrays of pressure sensors are reduced due to the vector sensor's directional azimuth capability. Additionally, DIFAR has become a low-cost instrument in the military marketplace, where the US manufacturers have produced more than four million units [32, 33].

It was evident that the principal interest in vector sensors was due to their directional information with a small aperture array. This directionality, provided by the particle motion or its derivatives, is still a topic of research, as evident from the series of studies regarding direction-of-arrival (DoA) estimation.

Nehorai and Paldi [34] developed an analytical model of the angle estimation error using the Cramer-Rao Bound (CRB) for an array of vector sensors. The model shows the decoupled noise power between pressure and velocity components of an ideal co-located sensor. Moreover, the intensity-based and velocity covariance-based algorithms for direction-finding are presented. These techniques have the advantage of performing an instantaneous estimation of the source direction and can be applied to narrow and wide-band sources.

Motivated by applications of vector sensors in hull-mounted sonar, the interference of the medium on the DoA estimation was studied [35]. The presented results shows that if sensors are mounted on a rigid hull, the pressure is forced to zero (at low frequencies). Thus, if pressure sensors are used, they must be offset from the rigid hull. Particle velocity, on the other hand, is not forced to zero. Although the model assumes ideal boundary conditions, such as isotropic, homogeneous fluid, and plane-wave, which may not guarantee its practical application, the applicability in hull-mounted sonar is shown to be possible. The use of vector sensors in towed array sonar was also investigated [36]. The advantages of using vector sensors in towed arrays are the grating lobes suppression, the solution to the left-

right ambiguity of uniform linear array (ULA), and the improvement of DoA estimation in the end-fire direction (parallel to the array axis).

Relevant considerations in vector sensor measurements is the plane-wave far-field assumption. In this condition, particle velocity measurement is usually converted into a directional pressure-equivalent (see section 2.1). Most studies assume this condition, which is not valid if the source and vector sensor are up to one wavelength close to each other or it is not in a plane-wave condition (near to the surface or bottom) [37]. For these conditions, there is a complex-phase difference between pressure and velocity channels, and the conversion (pressure-equivalent) is not direct [38]. Thus, knowledge of the scenario (position, water depth, and frequency) is necessary to analyze the vector sensor data correctly. Moreover, the assumption of isotropic noise and the lack of interference between particle velocity channels may not represent reality, making experimental data the most reliable way to investigate the anisotropy presented in the pressure and particle velocity components.

One can notice that spatial signal processing theory, usually applied to scalar sensors, has started to be adapted to include the extra particle velocity information [39]. Much work has been done on this subject, taking advantage of additive or multiplicative channel combining methods [34, 40, 41, 42], or even exploiting signal and noise subspace domains [43], higher-order array manifold [44], or artificial intelligence [45]. Examples are the beamforming techniques, such as Capon and subspace-based high-resolution ESPRIT, which were adapted in a novel structure that includes the particle velocity fields [43, 46, 47]. The algorithms may provide a gain up to $10\,\text{dB}$ compared to an array of scalar sensors. A beam steering method has been employed for sonar applications, and researchers have closely investigated optimization for the steered beam output using vector sensors' components [41, 44]. One possible

approach, referred to as hippioids, uses products of cardioids to narrow the beamwidth [41]. However, the non-linear operation may impact the beam response when multiple interferences are present, which reduces its benefits. Recently, a wide comparison study using a higher-orders array manifold has proved that the first-order linear combination from beam steering is still a robust and straightforward option for steerability [44].

Vector sensors have also been used for geo-acoustic parameter estimation. Seabed properties, such as sediment compressional speed, density, and compressional attenuation, are usually the estimated parameters of the seismic acoustic mapping. A Bartlett estimator, based on particle velocity measurements, is proposed by Santos et al. [48] to estimate these parameters. The results presented show a new possibility to explore vector sensors using high-frequency signals ($>5\,$kHz). In this sense, the dual accelerometer vector sensor (DAVS) was designed to improve the seismic geo-acoustic estimation. Designed by Jesus and Felisberto [49], the DAVS has two accelerometers and one resin-encapsulated hydrophone. Its geometric architecture makes it possible to form a beam (steered) to the bottom while attenuating the direct and surface reflection paths, which enhance the bottom ray [50].

Recently, the DAVS was employed in a shallow water experiment to record biological and anthropogenic noise [37]. Researchers have increased interest in vector sensors for marine biology due to the extra information on particle motion or particle velocity. Its measure is considered a link to explain the behavior of fish and invertebrates in an area [51]. Azigrams, an image plot where directions are related to a colormap, have been used as an interesting way to display marine life with directional information [52]. Moreover, since some species of fish and invertebrates respond to particle motion, vector sensors have been used to quantify the impact of anthropogenic noise on marine life.

1.1.3   Vector sensors for underwater acoustic communications

For UWAC, vector sensors are relatively new, considering that the first published paper using vector sensors as a receiver for underwater communications was presented by Abdi et al. [53] in 2007. This study compares the performance between a vector sensor and a pressure sensor array. Although the work does not use experimental signals, it utilizes an experimental shallow-water sound-speed profile to model the underwater channel. The study considers a single vector sensor as a SIMO system and performs a zero-forcing equalizer. Simulation results show the superior performance of the vector sensor in the proposed scenarios, which are justified due to the smaller values of the RMS-delay spread (DS) for particle velocity components than for pressure component. Thus, the work shows vector sensors as a new possibility for communication systems.

That first work has served as a precursor of some theoretical studies presented in [54, 55, 56]. These studies address vector sensors' channel correlation, considering UWAC multipath issues [54]. Analytical expressions took into account vector sensor spacing, frequency, and angle-of-arrival (AoA) spreading. Important insights, under Gaussian distribution assumption and small AoA spreading, show that pressure and particle velocity components can be totally uncorrelated. What makes sense for spherically isotropic noise, presented in [57], may also be applied for symmetric AoA signals in vector sensor components. Moreover, even if not so emphasized in that work, an interesting relationship is that vector sensor components may also be totally correlated, which generalizes the results for an intensity sensor, mostly considered in DoA studies.

Although analytical expressions help to understand the characteristics of particle velocity

components, practical receiver structures for UWAC were not addressed in [54, 55, 56], and a receiver for a SIMO system was then proposed [58]. That receiver, based on PTR, is tested with experimental data. Communication performance results have shown that a single vector sensor outperforms a 40 cm pressure-only array for short (<300 m) and medium ranges (>800 m). Such results suggest that particle velocity components can provide a new form of diversity, similar to an array of spatially separated pressure sensors.

Besides the attempts to explore diversity between vector sensor components, authors have also proposed the use of beamforming approaches to improve SNR and, consequently, enhance communication performance [59, 60]. However, details of the experiments, receiver structures, and data analysis are reduced. Even if such studies serve as an initial proof-of-concept, the presented results, based on just a single transmission, are not conclusive.

In summary, studies of vector sensors as a receiver for UWAC have focused on comparing vector sensor performance with pressure-only arrays. These studies show the size benefit of a compact sensor. However, some aspects could also be analyzed, such as the comparison of receiver structures and adaptation of structures designed for vector sensors rather than standard ones. Thus, this work intends to discuss such aspects, showing how to combine vector sensors' components advantageously.

1.2   Work motivation

Reliable underwater acoustic communications provide convenient support for untethered submerged platforms for ranges beyond, say, 100 m [26]. Fixed or mobile submerged platforms need to communicate either to other submerged platforms or to surface stations. Mobile platforms in particular, e.g., AUVs and gliders, are particularly challenging for UWAC because

underwater acoustic channels are continuously varying due to changing spatial characteristics of the propagation media [61]. Those mobile assets are restricted in size and weight, as they need maneuverability and low-power consumption, which limits them to use only a simple acoustic transducer modem [5, 62]. Typically, such acoustic transducers have an omnidirectional or a fixed directional pattern, from which this study differs, proposing the use of higher-order sensors, known as acoustic vector sensors, with steerable directional capability compared to their omnidirectional counterparts.

Vector sensors have been widely used for sonar applications to mitigate the left-right ambiguity of line arrays and provide a directional gain even for low-frequency signals (under 300 Hz) [63]. It is notorious and expected that most of the literature on vector sensors addresses the direction-finding issues since a compact collocated device can outperform ordinary pressure sensors or enhance the gain of a pressure array [34, 64, 65]. Although DoA methods may provide accurate direction estimation, the use of this information for the benefit of underwater acoustic communications is not directly explored.

The use of vector sensors for UWAC is relatively recent, and vector sensors' components are used as a single-input multiple-output system, acting itself as an equalizer [53, 58]. Usually, the components are considered as independent channels, and a matched-filter combining is used, implemented as versions of multichannel equalizers [53] or passive-time reversal [58]. In such approaches, the advantage of the vector sensor over the pressure sensor is clearly explained by its intrinsic directionality, both by filtering multipath when the horizontal component is used and by exploring channel diversity, which in theory, could be provided by the vertical component in far-field scenarios.

Since the employment of standard structures shown in the literature is nonexclusive for

vector sensors, e.g., they may also be used for a pressure-only array, we may think if a specific design for vector sensors, taking advantage of the directional information, could enhance the achieved performance. Understanding particle velocity components is essential to take advantage of correlated and uncorrelated channels and to design receiver structures to explore such correlation scenarios properly. Whereas a single vector sensor beam pattern response is well understood, its impact on the communication performance is unclear since SNR and ISI may affect directional and omnidirectional components differently.

Thus, some general questions have guided this work:

1. How particle velocity information may be used to increase the performance of an acoustic communication receiver?

2. Signal processing techniques, such as beamforming and passive time-reversal, differ by the assumption of the input signal/channel knowledge. Thus, how particle velocity components are explored in such methods? Moreover, may short or long range acoustic scenarios favor one method rather than the other?

3. How is the vector sensor performance in typical underwater communication bandwidth (say 2 to 15 kHz) compared to an array of pressure sensors?

4. Knowing that spatial diversity is achieved with a spaced array of pressure sensors, which means that different paths provide different acoustic channels, how can a single vector sensor provide diversity as a collocated device?

5. Can source direction estimation provide any benefit? How to use this information?

These and other questions motivate this study. Since vector sensors and communications

are two distinct areas of study, it is fair to say that this work is more focused on vector sensors and their characteristics in underwater acoustics. Thus, we do not emphasize the development of coding techniques or equalizers, although receiver structure adaptation is proposed for performance enhancement.

In summary, answering those previous questions, this work aims to explain the influence of the acoustic particle velocity component in receivers for underwater communications. Moreover, the development and comparison of receivers that take advantage of particle velocity may help to understand how to combine vector sensor components advantageously. Finally, since experimental data provides the most reliable way to explore anisotropic propagation conditions, this work shows two field experiments, each one with a different vector sensor technology.

1.3   Thesis outline

The following chapters present: vector sensor technologies; analysis of vector sensor channels; the tested and proposed methods; results; and conclusions. Chapter 2 shows two common types of vector sensors used for underwater communications, where particle velocity measurement is clearly explained, and a brief discussion regarding vector sensor directivity is made. Chapter 3 briefly reviews acoustic communication systems in the context of multichannel systems. Moreover, the data model and analytical expressions for vector sensor channel correlation are developed and analyzed. Chapter 4 shows the receiver structures, where standard passive time-reversal is used with vector sensor components, a beam steering method is presented as a straightforward practical receiver, and the joint beam steering and passive time-reversal is proposed as an adaptation for taking advantage of both previous

methods. Chapter 5 show the results of two field experiments and a case study simulation, where the tested receiver structures are compared and analyzed. Finally, Chapter 6 presents the conclusion, the summary of activities, contributions, and prospective.

Chapter 2

Vector sensor technologies

Synopsis*: This chapter discusses aspects related to vector sensor technologies. A source of misunderstanding is related to the existent types of vector sensors and their nomenclatures. The literature becomes cumbersome, when occasionally authors mix the conversion technology with the directional characteristic of vector sensor. Thus, this chapter aims to define important characteristics used in the following chapters, such as pressure-gradient vector sensors, accelerometer-based vector sensors, particle velocity, pressure-equivalent particle velocity, and related conversion technologies. Moreover, a brief discussion regarding directionality is also presented.*

In the present work, a "vector sensor (VS)" is a generic device sensitive to both the magnitude and direction of the acoustic wave. A vector sensor separately measures the acoustic pressure and directional components, usually by sensing or estimating the particle velocity. While acoustic pressure has been used in major underwater acoustic applications, the use of particle velocity was more restricted to military applications and is still unconventional for some underwater applications. In order to clarify the principle of vector sensors, this chapter concisely explains the transduction physics behind pressure-gradient

and accelerometer-based vector sensors, two common types of vector sensors reported in the literature of acoustic transducers.

Electroacoustic transducers are devices that convert electrical energy into acoustical energy or vice-versa [66]. In the underwater environment, a projector is an active device, whereas the hydrophone is a passive one. These are the underwater "version" of the loudspeaker and the microphone in the airborne sound, respectively.

Even though electroacoustic devices date back to the 19th century, a new era for underwater transducers spurs from advances in piezoelectric materials after 1950. The lead zirconate titanate (PZT) ceramic is an example of piezoelectric material used in most underwater sound transducers. Normally, the output voltage of a piezoelectric ceramic hydrophone is proportional to the acoustic pressure, which is a scalar quantity. However, a workaround in the piezoelectric hydrophones design makes it to respond to the acoustic particle velocity (also called velocity hydrophones [66]).

2.1   Particle velocity

In acoustics, particle displacement, velocity, or acceleration may be defined in terms of continuum mechanics [38]. The size of a particle is not a fixed value. However, it is considered large enough to represent a continuous volume and small enough not to affect the acoustic parameters in a volume. If we consider an homogeneous, isotropic, and non-viscous medium, the particles move around an equilibrium point. The directional proprieties of the particle make it an attractive measure of the acoustic field.

A fundamental acoustic equation is given by the Euler's equation or equation of particle motion:

$$\nabla p = -\rho_0 \frac{\partial \mathbf{v}}{\partial t} = -j\omega\rho_0 \mathbf{v}, \tag{2.1}$$

that can be rearranged to:

$$\mathbf{v} = -\frac{1}{j\omega\rho_0}\nabla p, \tag{2.2}$$

where ∇ is the gradient operator, p is the pressure, ρ_0 is the medium static density, $\mathbf{v}$ is the particle velocity vector, t is time, and ω is the angular frequency. The minus signal means that the reference points to the source (opposite to the wave propagation direction). Note that each component of the pressure gradient is proportional to the acoustic acceleration in (2.1). Thus, this is indicative that gradient (pressure-gradient) and inertial (acceleration) quantities are related to each other if the field is totally acoustic, e.g., does not include vibration or turbulence. Thus, since the ocean environment and acoustic applications usually add some "turbulence" effect, which is a non-acoustic source, these equations may not be valid or may include errors in describing the acoustic field.

The spherical acoustic field is defined as $p = \frac{p_0}{r}e^{j(\omega t \pm kr)}$, where p_0 is a reference pressure, $k = \omega/c = 2\pi/\lambda$, and r is the source-receiver distance. Solving (2.2) for the pressure leads to:

$$\mathbf{v} = -\frac{1}{\rho_0 c}\left(1 - \frac{j}{kr}\right)p = -\frac{1}{z}\,p, \tag{2.3}$$

where the complex impedance is

$$z = -\frac{\rho_0 c}{1 + \frac{j}{kr}}, \tag{2.4}$$

which indicates a phase difference between pressure and particle velocity. Note that for small values of kr (near-field, k$r \ll 1$), the phase difference between pressure and particle velocity is 90°. On the other hand, if kr is considered large (far-field and plane-waves, k$r \gg 1$),

particle velocity and pressure are nearly in phase. Thus, under the latter condition, (2.3) becomes:

$$p_v = -\rho_0 c\ \mathbf{v}, \tag{2.5}$$

where the product $\rho_0 c$ is the acoustic impedance and p_v is the so-called, pressure-equivalent particle velocity (index v is used to refer to particle velocity). Replacing (2.5) in (2.1) using Cartesian coordinates:

$$p_{vx} = \frac{1}{jk}\frac{\partial p}{\partial x},\ \ p_{vy} = \frac{1}{jk}\frac{\partial p}{\partial y},\ \ p_{vz} = \frac{1}{jk}\frac{\partial p}{\partial z}. \tag{2.6}$$

Equations (2.5) and (2.6) show two approaches to obtain pressure-equivalent particle velocity, either by using a velocity-sensitive sensor in (2.5) or by using a pressure-gradient sensor in (2.6). The former sensor is usually based on inertial sensors, commonly referred to as accelerometer-based, and the latter uses pairs of hydrophones. Other transducer designs to measure particle velocity have been developed, but pressure-gradient and accelerometer-based are the most reported in the literature.

2.1.1   Pressure-gradient vector sensor

One approach to measure particle velocity is using a pair of hydrophones. If the hydrophones are identical and small in comparison to the spacing s between them, s is small compared to the wavelength (say $s/\lambda \ll 1$), and a wave-front arrives with angle θ referred to the sensors' axis, then subtracting the pressure outputs gives [66]:

$$\Delta p(\omega) = p_1 - p_2,$$

$$= p_0 e^{jk\frac{s}{2}\cos\theta} - p_0 e^{-jk\frac{s}{2}\cos\theta},$$

$$= j2p_0 \sin\left(k\frac{s}{2}\cos\theta\right),$$

$$\Delta p(\omega) \approx j p_0 k s \cos\theta = j p_0 2\pi \frac{s}{\lambda} \cos\theta. \tag{2.7}$$

Thus, (2.7) has a beam pattern with cosine directivity, 90° of phase shift, and a 6 dB/octave slope in the frequency response. Considering a first-order differential approximation $\frac{\partial p}{\partial s} \approx \frac{\Delta p}{s}$, for one axis in (2.6), we have:

$$p_v = \frac{1}{jk'} \frac{j p_0 k s \cos\theta}{s'}, \tag{2.8}$$

where the superscript $[]'$ represents estimated values, since c and s may be approximated values. In (2.8), if $k' = k$ and $s' = s$, then:

$$p_v = p_0 \cos\theta, \tag{2.9}$$

indicating the intrinsic directionality of particle velocity. However, notice that (2.9) shows a cosine (or dipole) ambiguity, which is not interesting for DoA estimation purposes and may not be advantageous for communications. Thus, an additional centralized hydrophone is commonly used, providing a phase reference. Summing one hydrophone to (2.9) leads to a $(\delta + \cos\theta)$ term, which is a cardioid-like depending on a δ design factor. This last operation is the reason for a vector sensor to include the additional hydrophone, where its impact on the vector sensor directivity is shown in section 2.2.

Besides the directivity provided by the pressure-gradient vector sensor, some advantages of using this type of vector sensor are:

- The hydrophones can be used as a scalar pressure array, in which the sum of outputs still results in an omnidirectional response, or as a vector sensor by subtracting the outputs;

- Hydrophones can be produced in a very small size, which results in a compact sensor;

- Ideally, hydrophones are insensitive to acceleration (in practice, this may not be verified, but compared to accelerometers they are less sensitive [64]). Thus, they are less affected by mechanical vibrations or noise flow.

On the other hand, pressure-gradient sensors are limited by:

- The hydrophones must be well-matched in both amplitude and phase response. Thus, accurate design and calibration are necessary;

- Since the response is dependent on the spacing between hydrophones, it acts as a two-element aperture array, or viewed to as an "aperture" sensor [64]. Reducing the size, consequently the spacing between sensors, the dynamic range may be significantly reduced due to the subtraction (see $\Delta p \propto s/\lambda$ in (2.7)). Thus, to achieve the dipole-like directionality, there is a trade-off between spacing and a feasible response. Moreover, reducing the spacing between the hydrophones increases the chances of interference between them (electronic and mechanical);

- Must have low electronic self-noise since the dynamic range is reduced by subtraction.

Due to the use of a pair of hydrophones, which produces a cosine pattern, this vector sensor model is also called a dipole vector sensor. For estimating azimuth and elevation angles, three pairs of hydrophones orthogonally-oriented are required. Since the number of hydrophones increases, there are more possibilities of mismatch between hydrophones, which can be a design problem. An alternative to this type of technology is to use inertial devices.

2.1.2   Inertial sensors

Inertial sensors designed for underwater acoustics have their output directly related to the motion of a sensor body. The type of the design (transducer technology) defines whether the output is proportional to the motion, velocity, or acceleration. Unlike the subtract operation made in pressure-gradient vector sensors, inertial sensors detect the net force or the particle motion over a body.

Accelerometers are transducer devices commonly used for the vector measure of the acoustic field. Piezoelectric accelerometers are classified as inertial sensors [66]. Ideally, they are insensitive to pressure but sensitive to motion. Usually, their sensitivity is the result of net forces or particle motion.
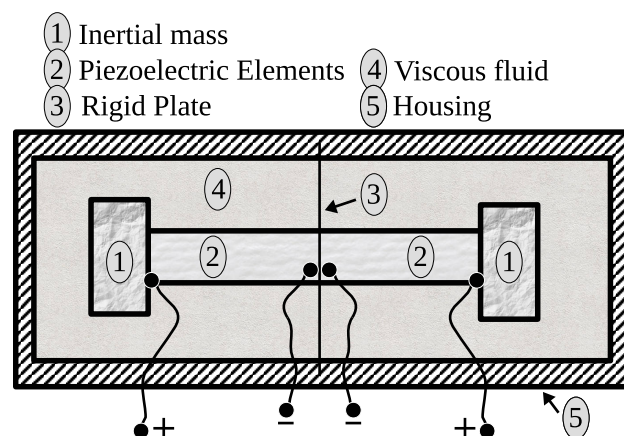
Figure 2.1: Accelerometer for net force detection, adapted from [66]

Figure 2.1 illustrates a pair of accelerometers attached to a center plate. The inertial mass responds to the motion, and the piezoelectric bar generates a proportional output voltage. The piezoelectric elements have a reverse polarity that leads to a positive voltage, which corresponds to the acceleration, in opposite terminals when compression or expansion is verified. Note that accelerometers detect the net force (consequently, the acceleration) due to the differential pressure, while the dipole in the previous section detects the pressure

difference.

Inertial sensors may allow flat and wide frequency bandwidth, and large dynamic range. However, they respond to motion regardless it is provided by acoustic waves, turbulence, or vibration. Thus, some practical issues arise:

- Due to the susceptibility to flow noise, particle motion is better measured if the device is freely moving in the environment;

- As inertial sensors do not distinguish between acoustic and non-acoustic disturbance, a suspension must be provided to guarantee isolation from the structure-born vibration and to permit movement with the acoustic field;

- Isolation in the low-frequency (<10Hz) operation may be a challenge;

- Measuring vertical particle acceleration needs a complex surface-motion isolation system. As an example, a small variation in the hydrostatic pressure due to the surface motion causes a large oscillation in the vertical measurement of the acceleration;

In summary, each type of vector sensor has its particular sensitivity characteristics and practical limitations. Moreover, the knowledge of transduction technology is relevant to explain observed effects on experimental data analysis. For instance, the susceptibility to noise may differ in inertial sensors and pressure-gradient sensors. Thus, it is crucial to know the advantages and disadvantages of each sensor for its correct usage.

2.2   Vector sensors directionality

The directional information provided by one vector sensor is an attractive characteristic of a compact sensor. Several studies have shown the superior performance of vector sensors

in spatial filtering when compared to an array of pressure sensors [33, 34, 67]. Moreover, comparisons between an array of vector sensors and pressure sensors for DoA have shown improvement in directivity, sidelobe suppression, grating-lobes mitigation, and, consequently, SNR enhancement [32, 39]. Here, a brief study of directionality is presented to highlight such characteristics when a single vector sensor or a VSA is employed.

A useful measure of performance of a pressure-only array is quantified through the aperture directivity, defined as [68]:

$$D = \frac{P(\theta_0, \phi_0)}{\frac{1}{4\pi} \int_0^\pi \int_0^{2\pi} \sin\phi P(\theta, \phi) d\theta d\phi}, \tag{2.10}$$

where, θ_0 and ϕ_0 are the steering direction, and $P(\theta, \phi)$ is the power pattern. The aperture directivity shows the ratio between the maximum and the average power pattern, or peak to average sidelobe level, where the power pattern refers to the square magnitude of the beam pattern. This relation can be used for a simple and limited comparison between pressure-only arrays (array gain) and vector sensors (directional gain) in a free-field medium. For a uniform weighted linear array of N pressure sensors (spacing of $\lambda/2$, where λ is the wavelength), the directivity is proportional to the number of sensors, $D = N$, which means that more focus is achieved as the number of sensors increases. However, for one vector sensor, $D = D_p + D_{vx} + D_{vy} + D_{vz}$, where, $D_p = 1$, $D_{vx} = 3\cos^2\theta_0\cos^2\phi_0$, $D_{vy} = 3\sin^2\theta_0\cos^2\phi_0$, $D_{vz} = 3\sin^2\phi_0$. Thus, (2.10) reduces to $D = 4$, for equal weighting, which gives a gain of $6\,\mathrm{dB}$ (viewed as directivity index, $DI = 10\log_{10} D$) [63, 65]. This relation shows that four pressure sensors are needed with a spacing of $\lambda/2$ to achieve an equivalent gain of one vector sensor.

As shortly stated in section 2.1.1, the combination of pressure and one-axis particle

velocity component leads to a $(\delta + \cos\theta)$ term. Fig. 2.2 (a) shows the impact of δ on the directivity (or radiation pattern) for an one-axis vector sensor. One can verify the dipole ambiguity for $\delta = 0$, which is attenuated as δ increases. The cardioid-like shape is obtained for $\delta = 1$, where a null is observed at the backside. The directional filtering capability degrades for $\delta \gg 1$, where the omnidirectional pressure component becomes predominant. Fig. 2.2 (b) shows the steering capability using a two-axis vector sensor. In this illustration, $\delta = 1$, and we are weighting the vector sensor components as: $\delta + \cos\theta\cos\theta_0 + \sin\theta\sin\theta_0 = \delta + \cos(\theta - \theta_0)$. A detailed explanation regarding the employment of this steering approach is presented in section 4.2. Here, the objective is to show that a steered beam pattern in a desired direction θ_0 is achieved with a single vector sensor.
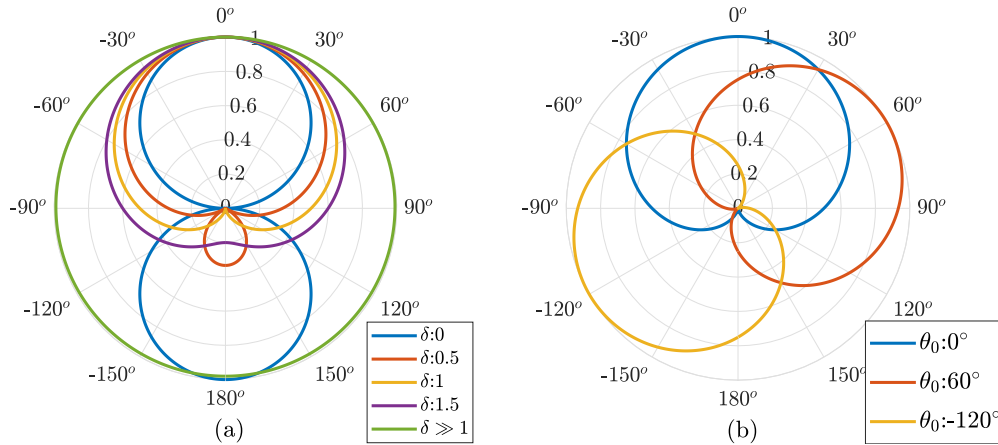
Figure 2.2: Normalized directivity patterns: for a one-axis vector sensor varying δ (a); and for a two-axis vector sensor weighting the components according to θ_0 (b).

A generalized analysis extending a single vector sensor can be performed for a VSA. Assuming a homogeneous medium and far-field plane-wave condition, an array of L vector sensors is illustrated in Fig. 2.3. Each vector sensor has four outputs (pressure and three orthogonal particle velocity components) and vertical spacing r_i from the origin taken as reference. The source direction is represented by the azimuth $\theta_s \in [-\pi, \pi]$, and elevation $\phi_s \in$

$\left[\frac{-\pi}{2}, \frac{\pi}{2}\right]$. Moreover, the source emits a narrow-band sinusoidal signal at angular frequency ω_0. Thus, the output of the VSA is given by:

$$y_{pv} = [y_{p_1} y_{v_{x_1}} y_{v_{y_1}} y_{v_{z_1}}, \cdots, y_{p_L} y_{v_{x_L}} y_{v_{y_L}} y_{v_{z_L}}]^T, \tag{2.11}$$

where the index $[]_p$ and $[]_v$ stand for pressure and pressure equivalent particle velocity components, respectively. Thus, the output y_{p_1} refers to the first pressure sensor, and $y_{v_{x_L}}$ refers to the L-th x-axis particle velocity component.
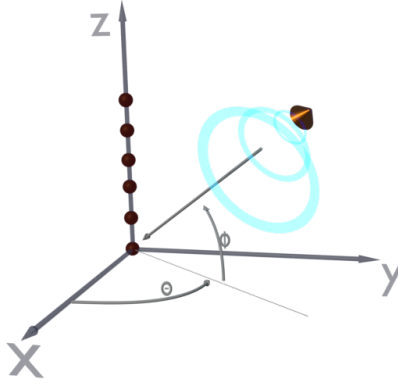
Figure 2.3: Uniform linear array (ULA) of vector sensors

Considering the normalized pressure-equivalent particle velocity, the acoustic field in rectangular coordinates is given by:

$$y_{pi}(\omega_0, \theta_s, \phi_s) = e^{-j\mathbf{k}_s \mathbf{r}_i},$$

$$y_{v_{xi}}(\omega_0, \theta_s, \phi_s) = e^{-j\mathbf{k}_s \mathbf{r}_i} \cos\theta_s \cos\phi_s,$$

$$y_{v_{yi}}(\omega_0, \theta_s, \phi_s) = e^{-j\mathbf{k}_s \mathbf{r}_i} \sin\theta_s \cos\phi_s, \tag{2.12}$$

$$y_{v_{zi}}(\omega_0, \theta_s, \phi_s) = e^{-j\mathbf{k}_s \mathbf{r}_i} \sin\phi_s,$$

where the wave-number $\mathbf{k} = -\frac{2\pi}{\lambda}\mathbf{u}$, the unitary vector $\mathbf{u} = [\cos\theta\cos\phi, \sin\theta\cos\phi, sin\phi]^T$, and the sensor position $\mathbf{r} = [r_x, r_y, r_z]$. Thus, (2.12) can be rewritten as:

$$\mathbf{y}_{pv}(\omega_0, \theta_s, \phi_s) = \begin{bmatrix} 1 \\ \mathbf{u}(\theta_s, \phi_s) \end{bmatrix} \otimes e^{-i\mathbf{k}_s \mathbf{r}_i}, \tag{2.13}$$

where $\otimes$ is the Kronecker product. The array manifold $\mathbf{w}$ for the VSA can be defined as [68]:

$$\mathbf{w}(\omega_0, \theta, \phi) = \begin{bmatrix} 1 \\ \mathbf{u}(\theta, \phi) \end{bmatrix} \otimes e^{-i\mathbf{k}\mathbf{r}_i}. \tag{2.14}$$

Thus, the beam pattern for a VSA is given by:

$$B_{pv}(\omega_0, \theta, \phi) = |\mathbf{w}^H(\omega_0, \theta, \phi)\mathbf{y}_{pv}(\omega_0, \theta_s, \phi_s)|^2. \tag{2.15}$$

Figure 2.4 shows the beam pattern simulation of a vector sensor uniform linear array (ULA). There are nine vector sensors, and the spacing of the sensors is $\lambda/3$. The simulated source direction is $(\theta_s, \phi_s) = (90°, 45°)$. Fig. 2.4 (a) shows the normalized energy detection in an azimuth-elevation surface using only the pressure sensors (i.e., equivalent to zeroing the $\mathbf{y}_v$ components in (2.13)). Note the well-known azimuth ambiguity issue. Fig. 2.4 (b) shows the normalized energy detection where the maximum energy coincides with the source direction. Moreover, the azimuth ambiguity problem in ULA is solved due to the directional information of x-y particle velocities.
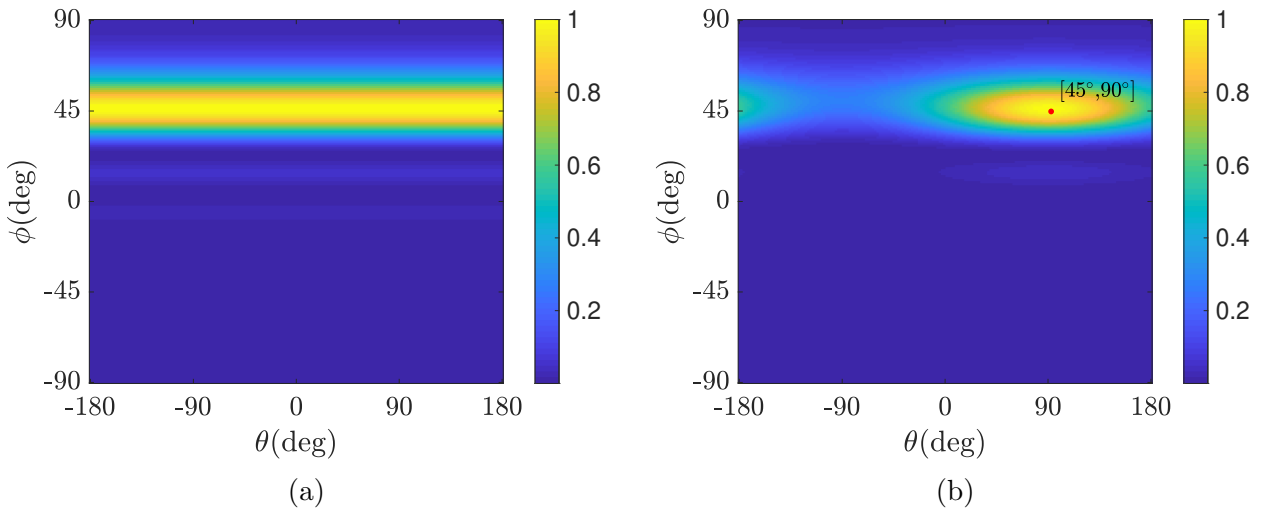
Figure 2.4: Normalized beam pattern for: a ULA with nine pressure-only sensors (a); and a ULA with nine vector sensors (b). Both tested arrays have a spacing of $\lambda/3$, source direction $(\theta_s, \phi_s) = (90°, 45°)$.

A spacing analysis can be performed for a constant azimuth angle $(\theta_s = 90°)$ by varying

the spacing of sensors from $\lambda/150$ to λ. Note that such analysis is analogous to a frequency

variation since $\lambda = c/f$. For the previous array configuration, the beam pattern is shown in

the spacing-elevation surface of Fig. 2.5. Comparing the pressure-only array in Fig. 2.5 (a)

with the VSA in Fig. 2.5 (b), one can notice the side-lobes reduction using the VSA, and

the grating-lobes (spatial aliasing), which start to appear for spacing $d > \lambda/2$, are mitigated

using the VSA.
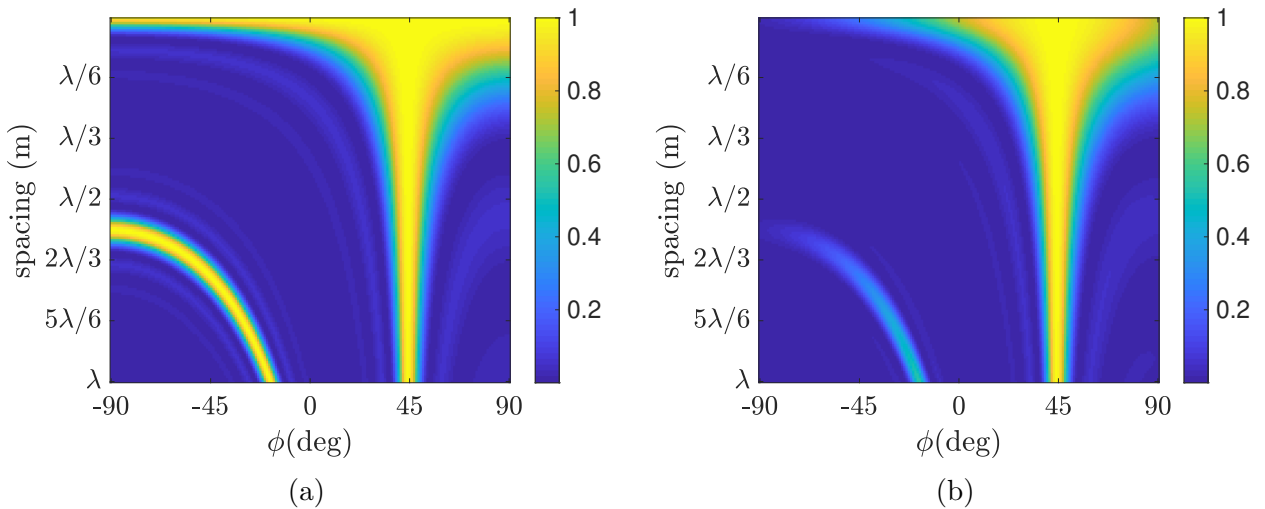
Figure 2.5: Beam pattern for variable sensor element spacing: a ULA with nine pressure-only sensors (a); and a ULA with nine vector sensors (b). In both tested arrays, the source direction is $(\theta_s, \phi_s) = (90°, 45°)$.

One last analysis uses only one vector sensor, where the simulated source direction was set

to $(\theta_s, \phi_s) = (90°, 45°)$ in Fig. 2.6 (a) and $(\theta_s, \phi_s) = (-90°, -45°)$ in Fig. 2.6 (b). The spatial

half-power bandwidth is about $\Delta\theta = 100°$ in azimuth and $\Delta\phi = 80°$ in elevation, which

may be considered a poor spatial resolution. However, compared to an omnidirectional

hydrophone, it can be considered an attractive option. Moreover, using only one vector

sensor, the beam-pattern is frequency-independent (see (2.12) for $\mathbf{r} = [0, 0, 0]$). In practice,

as described in [40, 64], for pressure-gradient vector sensors, the frequency dependence is

related to the difference operation, and for accelerometer-based vector sensors, piezoelectric

materials also have frequency dependency.
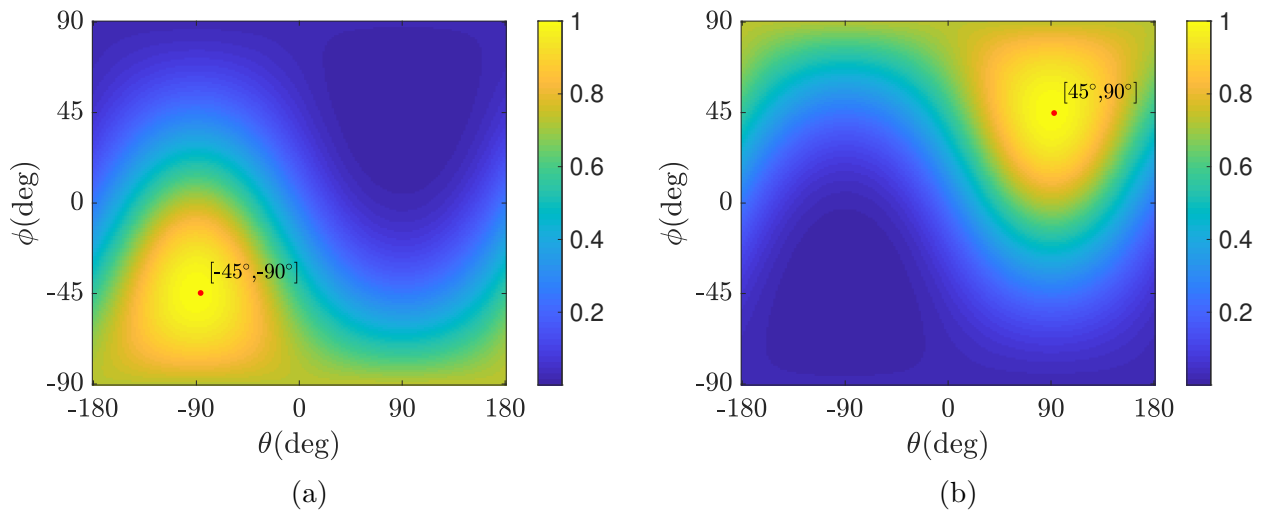
Figure 2.6: One vector sensor beam pattern. Source direction: $(\theta_s, \phi_s) = (-90°, -45°)$ (a); and $(\theta_s, \phi_s) = (90°, 45°)$ (b).

In summary, several analyses of the beam pattern can be performed, such as varying the number of sensors, spacing or frequency, and bearing. However, the presented review highlights the directionality characteristics of a vector sensor or VSA, which are sufficient for this study's scope.

Chapter 3

Vector sensor channel analysis

Synopsis: *This chapter analyzes vector sensor components from a statistical perspective. A brief review of underwater acoustic communication systems is presented in section 3.1. The two following sections present the data model and vector sensor channel correlation. The analysis of this latter section helps to understand the receiver structures proposed and tested in Chapter 4.*

3.1 Communication systems with vector sensors

This section presents an overview of underwater acoustic communication systems where a vector sensor is used as a receiver. The objective is to show basic elements of communication systems, the challenges of the underwater acoustic channel, and how vector sensors are integrated in the usual communication signal processing chain.

3.1.1 Transmitting stage

In Fig. 3.1, the "Information" block is the desired message to be transmitted. Preferably, the message should be short or compressed efficiently. The "Encoder" block transforms the message (analog or digital sources) to a sequence of binary digits (source encoder or data
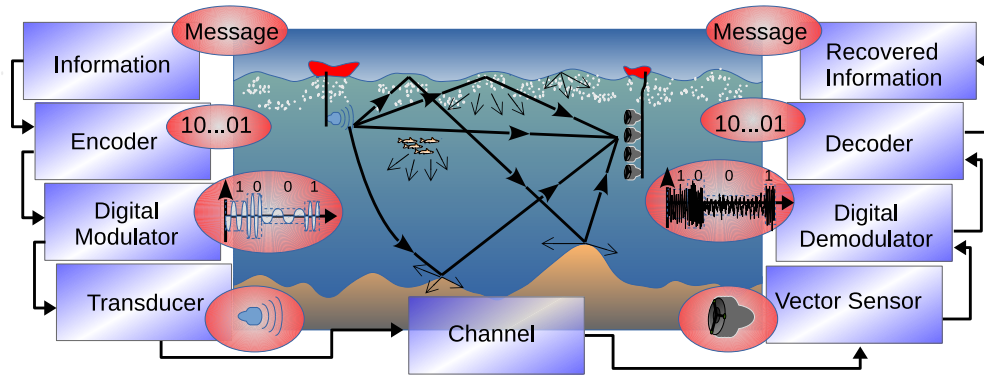
Figure 3.1: Underwater communication system using vector sensor as a receiver

compression) and inserts some redundancy into the binary sequence to overcome channel's distortion or ambient noise (channel encoder). Source and channel encoders are techniques to improve the system's reliability [3]. Then, the "Digital Modulator" converts the binary sequence into a higher-frequency signal to be transmitted through the underwater medium. The "Transducer" is the physical device, which in this example, acts as a projector, converting the electrical signal to a mechanical wave. Then, the acoustic wave propagates through the underwater medium, simply called "Channel".

3.1.2   Underwater acoustic channel

Figure 3.1 shows a simple representation of a ray-trace sound wave propagation. This figure intends to show some anisotropic characteristics of the underwater channel and how a transmitted signal is impacted along depth and range. Some effects can be noticed:

- Refraction and reflection: sound propagates in straight or smoothly curved paths, according to the sound speed profile and the boundary interfaces;

- Surface effects: turbulence, bubbles, schools of fish with air-filled swim bladders, breaking waves, and ship cavitation make the sound scatter randomly [69];

- Bottom effects: energy may propagate into many layers of materials resulting in sound reflection, transmission and attenuation [70].

In order to test and quantify performance of communication structures by using simulation, all these effects should be included in acoustic models. Three common models represent most communication systems, where the simplest one adds noise, usually Gaussian, to a deterministic signal. In this model, the channel causes only attenuation and thus, is not suitable for testing ISI issues.

The second model treats the acoustic channel as a linear filter. The signal at the receiver is given by:

$$r(t) = s(t) \otimes h(t) + n(t), \tag{3.1}$$

where $r(t)$ is the signal output, $s(t)$ is the signal input, $h(t)$ the channel impulse response (CIR) represented as a linear filter, $n(t)$ is the additive noise, and $\otimes$ stands for convolution in time. This last representations is useful for an initial analysis of communication systems. For instance, in this work, an acoustic numerical model provides the CIR of pressure and particle velocity components, which is used to obtain the vector sensor received signals. The drawback is that time and frequency spread may be difficult to be represented. For instance, Doppler due to surface motion or due to changing bathymetry as source and/or receiver movement over range-dependent bathymetry produce Doppler spread, which is more difficult to model. One last approach is to represent time-varying channels as a time-variant linear filter. In this model, the output signal is

$$\begin{aligned} r(t) &= s(t) \otimes h(t, \tau) + n(t), \\ &= \int_{-\infty}^{\infty} h(t, \tau) s(t - \tau) d\tau + n(t), \end{aligned} \tag{3.2}$$

where $h(t, \tau)$ is the time-delay CIR. (3.2) can be rewritten in terms of the channel's time-frequency dispersion characteristics. Thus, (3.2) becomes:

$$r(t) = \int_{-\infty}^{\infty} \int_{-\infty}^{\infty} S_H(\tau, \nu) s(t - \tau) e^{j2\pi\nu t} d\tau d\nu + n(t), \tag{3.3}$$

where, S_H is the spread function (delay-Doppler), and ν is the Doppler frequency. Time-varying channels shown in (3.2) and (3.3) can be represented as a deterministic or stochastic process, although, the deterministic description may not be feasible for a wide variety of operating conditions. Thus, $h(t, \tau)$ and $S_H(\tau, \nu)$ are random processes, generally restricted to a wide-sense stationary uncorrelated scattering (WSSUS) assumption [71]. This statistic perspective is developed in section 3.3, where analytical expressions considering the second-order statistics are developed.

3.1.3   Receiving stage

In Fig. 3.1, the "Vector Sensor" is the receiver device. As described in Chapter 2, it measures scalar acoustic pressure and directional components, e.g., particle velocity. Thus, a communication system that contains a vector sensor receiver may be seen as a SIMO system. The "Digital Demodulator" translates the received signal into a sequence that is an estimation of the transmitted sequence, and the "Decoder" uses the information of the channel encoder and source encoder to rebuild the original sequence.

3.2   Data model

The general system equation for a single vector sensor can be defined as:

$$r_p = h_p \otimes s + w_p,$$

$$r_{vx} = h_{vx} \otimes s + w_{vx},$$

$$r_{vy} = h_{vy} \otimes s + w_{vy}, \tag{3.4}$$

$$r_{vz} = h_{vz} \otimes s + w_{vz},$$

where $r_{(p/v)}$ are the received pressure/particle velocity signals, s is the transmitted signal, $h_{(p/v)}$ are the pressure (p) and the particle velocity (v) channel impulse response, and $w_{(p/v)}$ is the additive noise. Indexes x and y refer to horizontal directions, and z to the vertical. The symbol $\otimes$ stands for time convolution. As shown in section 2.2, (3.4) can be generalized for the l-th vector sensor, where $r_l = [r_{pl} \; r_{vxl} \; r_{vyl} \; r_{vzl}]$.

The underwater CIR can be modeled as delay (τ) and angle (γ) dependent. Consider two pressure sensors $(n = 1, 2)$ placed in 2D geometric space $(y, z) : [(0, z_1), (\epsilon, z_1 + L)]$ as shown in Fig. 3.2, where L and ϵ are vertical and horizontal sensor spacing, respectively.
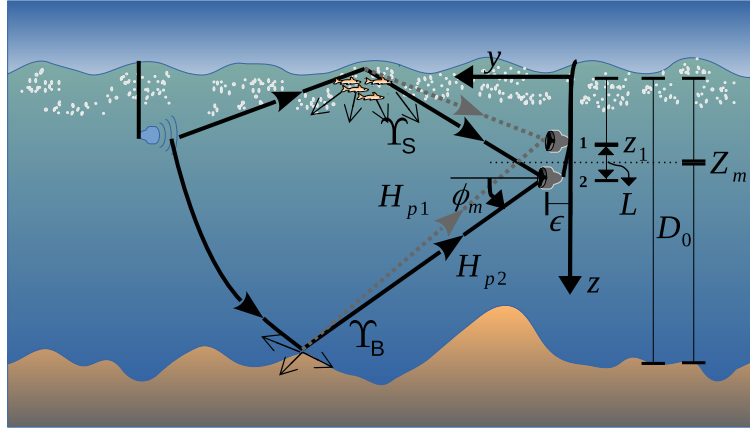
Figure 3.2: Illustration of an acoustic scenario where two pressure sensors are placed in 2D geometric space $(y, z) : [(0, z_1), (\epsilon, z_1 + L)]$. ϵ is a small displacement in range, while L is the vertical spacing. Z_m is the surface/bottom vertical distance (depending on ϕ_m) to the geometric center between sensors. Υ_B and Υ_S are bottom/surface scattering normalization factors.

Moreover, $L \ll \min(z_1, D_0 - z_1)$ (far from boundaries), where D_0 is the water depth. Each

pressure component h_{pn} can be written as [54]:

$$h_{pn}(\tau, \gamma) = \Upsilon_n \sum_{m=1}^{M} a_{nm}^p \delta(\gamma - \gamma_{nm}) \delta(\tau - \tau_{nm}), \qquad (3.5)$$

where m is the path number, δ is the Dirac delta function, n is the pressure sensor index, and Υ is a scattering normalization factor. In (3.5), a_{nm}^p is a complex value that contains the phase (ψ_{nm}) and the scattering amplitude. One can notice that γ_{nm} is the elevation or the azimuth angle in 2D space or a pair of azimuth and elevation angles in 3D space. Doppler shift is not considered in (3.5) for simplicity. Taking the Fourier transform in respect to τ, (3.5) becomes:

$$H_{pn}(f) = \Upsilon_n \sum_{m=1}^{M} a_{nm}^p e^{j\psi_{nm}} e^{jk([x_n, y_n, z_n] * \mathbf{u})} e^{-j\omega\tau_{nm}}, \qquad (3.6)$$

where $\mathrm{u} = [u_x, u_y, u_z]^T = [\cos(\phi_{nm})\cos(\theta_{nm}), \cos(\phi_{nm})\sin(\theta_{nm}), \sin(\phi_{nm})]^T$ is the unitary vector at receiver pointing towards the source. Azimuth and elevation angles are represented by $(\theta, \phi) : ([-\pi, \pi], [-\pi/2, \pi/2])$, where $\phi = \pi/2$ is the bottom direction, and (x_n, y_n, z_n) are the sensor's position. $\mathrm{k}^2 = k_x^2 + k_y^2 + k_z^2$ $(|\mathrm{k}| = \omega/c)$ is the wave vector, $\omega = 2\pi f$, is the angular frequency, and c is the sound speed.

Using $p_v = \frac{1}{jk}\frac{\partial p}{\partial s}$ from (2.6) in (3.6) and returning to (τ, γ) domain, the CIR of particle velocity can be seen as:

$$h_{vn}(\tau, \gamma) = \Upsilon_n \sum_{m=1}^{M} a_{nm}^v \delta(\gamma - \gamma_{nm}) \delta(\tau - \tau_{nm}) u_{(x/y/z)}, \qquad (3.7)$$

where comparing (3.7) to (3.5), the differences are a_{nm}^v and $u_{(x/y/z)}$, which designate pressure-equivalent particle velocity and the sine/cosine radiation pattern, respectively.

The three parameters (a^p, γ, τ) in (3.5) were considered deterministic to obtain (3.6). However, as exposed in section 3.1.2, the deterministic representation is less effective because it does not take the variability of the underwater channel into account, so a stochastic process

is preferable, where second-order statistic functions are necessary, as shown in the following section.

3.3 Vector sensor channel correlation

Analysis of vector sensor channel correlation can be made using (3.6), where a closed-form expression can be adopted. If a small angle spread is assumed, $\phi_{1m} \approx \phi_{2m} = \phi_m$, $\psi_{1m} \approx \psi_{2m} = \psi_m$, $a_{1m} \approx a_{2m} = a_m$, $\Upsilon_1 \approx \Upsilon_2 = \Upsilon$, and $\tau_{1m} \approx \tau_{2m} = \tau_m$. Thus, (3.6) becomes:

$$
\begin{aligned}
H_{p1}(f) &= \Upsilon \sum_{m=1}^{M} a_m^p e^{j\psi_m} e^{jk(z_1 \sin \phi_m)} e^{-j\omega \frac{Z_m}{c \sin \phi_m}}, \\
H_{p2}(f) &= \Upsilon \sum_{m=1}^{M} a_m^p e^{j\psi_m} e^{jk(\epsilon \cos \phi_m + (z_1 + L) \sin \phi_m)} e^{-j\omega \frac{Z_m}{c \sin \phi_m}},
\end{aligned}
\tag{3.8}
$$

where Z_m is the surface/bottom vertical distance to the geometric center between sensors. Now, we can define the pressure correlation (p index omitted) as [54]:

$$
C(\Delta f, L) = E[H_2(f + \Delta f) H_1^*(f)].
\tag{3.9}
$$

Considering uniform distribution of all phases ψ_m over $[0, 2\pi)$ interval, $E[e^{j\psi_m} e^{-j\psi_{m'}}] = 0$, $\forall\, m \neq m'$, and $E[e^{j\psi_m} e^{-j\psi_{m'}}] = 1$ if $m = m'$. Thus, (3.9) becomes:

$$
C(\Delta f, L) = \Upsilon^2 \sum_{m=1}^{M} E\left[a_m^2 e^{jk(\epsilon \cos \phi_m + L \sin \phi_m)} \times\ e^{-j\Delta\omega \frac{Z_m}{c \sin \phi_m}} \right],
\tag{3.10}
$$

where $\Delta\omega = 2\pi(f + \Delta f)$. Then, defining a AoA probability density function (PDF) as:

$$
\sum_{m=1}^{M} \left(\frac{E[a_m^2]}{M} \right) = \int_{\phi} w(\phi) \partial\phi,
\tag{3.11}
$$

(3.10) becomes (M omitted for convenience):

$$
C(\Delta f, L) = \Upsilon^2 \int_{\phi=0}^{2\pi} w(\phi) e^{jk(\epsilon \cos \phi + L \sin \phi)} e^{-j\Delta\omega \frac{Z}{\sin \phi}} \partial\phi.
\tag{3.12}
$$

Since small AoA spread is considered, a Gaussian PDF can be employed as a case study (see [54] and references therein for large angle spreads). Thus, one can define:

$$w(\phi) = \frac{1}{\sqrt{2\pi\sigma^2}}e^{-\frac{(\phi-\mu)^2}{2\sigma^2}}, \ 0 \leq \phi \leq 2\pi, \tag{3.13}$$

where σ is the angle spread and μ is the mean AoA. Replacing (3.13) in (3.12), for $\Delta f = 0$, results in

$$C(0, L) = \Upsilon^2 e^{j(k\epsilon\cos\mu+kL\sin\mu)}e^{-\frac{\sigma^2}{2}(-k\epsilon\sin\mu+kL\cos\mu)^2}, \tag{3.14}$$

where, for $\epsilon \to 0$, $C(0,0) = 1$, as expected. The gradient of (3.9) leads to pressure/particle velocity correlation:

$$\begin{aligned}
C^{py}(\Delta f, L) &= \frac{1}{jk}\frac{\partial C(\Delta f, L)}{\partial \epsilon}, \\
C^{pz}(\Delta f, L) &= \frac{1}{jk}\frac{\partial C(\Delta f, L)}{\partial L}, \\
C^{yz}(\Delta f, L) &= -\frac{1}{k^2}\frac{\partial^2 C(\Delta f, L)}{\partial \epsilon \partial L},
\end{aligned} \tag{3.15}$$

where only the y and z correlations are presented since x and y components are equivalent. Then, using (3.14) for $\epsilon \to 0$:

$$\begin{aligned}
C^{py}(0, L) =&\ \Upsilon^2[\cos\mu - j\sigma^2 kL\cos\mu\sin\mu]e^{jkL\sin\mu-\frac{\sigma^2}{2}(kL\cos\mu)^2}, \\
C^{pz}(0, L) =&\ \Upsilon^2[\sin\mu + j\sigma^2 kL\cos^2\mu]e^{jkL\sin\mu-\frac{\sigma^2}{2}(kL\cos\mu)^2}, \\
C^{zy}(0, L) =&\ \Upsilon^2[(1-\sigma^2)\sin\mu\cos\mu + \sigma^4 k^2 L^2\sin\mu\cos^3\mu- \\
&\ j\sigma^2 kL\cos\mu(\sin^2\mu - \cos^2\mu)]e^{jkL\sin\mu-\frac{\sigma^2}{2}(kL\cos\mu)^2}.
\end{aligned} \tag{3.16}$$

The development of these correlation expressions considers generalized M arrivals. However, an interesting approach is to separate the M arrivals into bottom and surface arrivals, as presented in [54]. Using (3.16) for a single vector sensor ($L = 0$):

$$C^{py}(0, 0) = \Lambda\cos\mu_b + (1-\Lambda)\cos\mu_s,$$

$$C^{pz}(0, 0) = \Lambda\sin\mu_b + (1-\Lambda)\sin\mu_s, \tag{3.17}$$

$$C^{zy}(0, 0) = \Lambda(1-\sigma_b^2)\sin\mu_b\cos\mu_b + (1-\Lambda)(1-\sigma_s^2)\sin\mu_s\cos\mu_s,$$

where, bottom arrivals have mean elevation angles μ_b (positive by definition) and AoA spread σ_b, while surface arrivals have mean elevation angles μ_s (negative by definition) and AoA spread σ_s. Moreover, $\Upsilon_B = \left(\frac{\Lambda}{B}\right)^{\frac{1}{2}}$ is defined as the bottom power scattering normalization, where Λ is the normalized amount of power that comes from B bottom arrivals. Similarly, $\Upsilon_S = \left(\frac{1-\Lambda}{S}\right)^{\frac{1}{2}}$, where $1 - \Lambda$ is the power that comes from S surface arrivals. Even if (3.17) is restricted to Gaussian PDF for small-angle spread, it shows that pressure and particle velocity channels present a sine/cosine pattern, and particle velocity channel cross-correlation presents a sine/cosine product pattern, which is weighted by the angle spread.
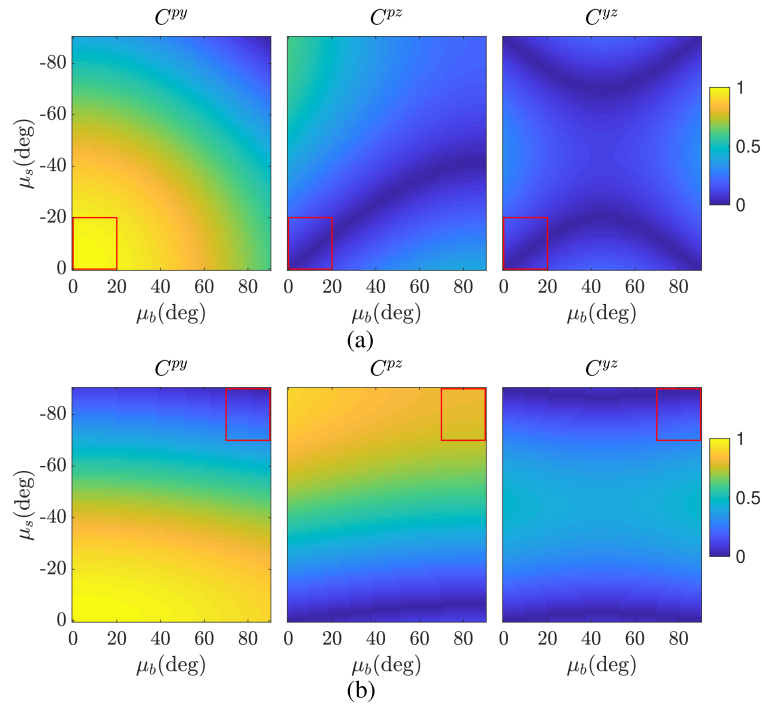
Figure 3.3: Pressure and particle velocity channel cross-correlations for varying bottom/surface mean value arrivals (μ_b and μ_s), using (3.17). Bottom and surface arrival spreads (σ_b and σ_s) are $10°$ and $1°$, respectively. Far-field scenario with bottom power scattering $\Lambda = 0.4$ (a), and close-range scenario with $\Lambda = 0.1$ (b).

Expressions shown in (3.17) can be visualized in Fig. 3.3 for varying bottom and surface arrival angles. Different from the analysis shown in [54], where the focus was on the correlation between spaced vector sensor components, here, a single collocated vector sensor is

analyzed. Fig. 3.3 (a) represents a far-field scenario and shows that pressure and horizontal particle velocity correlation (C^{py}) are highly correlated (> 0.8) for predominant horizontal arrivals, which can be represented by angles not steeper than 20° as shown by red boxes. In this figure, C^{py} would be lower than 0.5 for steeper arrivals from 45° to 90°, which can represent late arrivals. For C^{pz}, a low level of correlation is verified, which can be explained due to the sine symmetry, $\sin(-\mu) = -\sin(\mu)$, resulting in C^{pz} nearly zero for symmetric arrivals (it is not zero since $\Lambda = 0.4$). Finally, particle velocity components cross-correlation present small values. This can be explained by the orthogonality between vertical and horizontal channels. Thus, analysis of Fig. 3.3 (a) suggests that pressure and the horizontal components are suitable for methods that explore channel coherence. Otherwise, as the correlation between pressure and the vertical component is low, diversity methods may be preferable.

The correlation analysis for close-range scenarios can be made by analyzing Fig. 3.3 (b). In this case, μ_b and μ_s are steeper (close to $\pm 90°$, as shown in red boxes). The correlation between pressure and horizontal particle velocity is low (<0.5), as C^{py} is cosine dependent. The opposite is verified for pressure and vertical particle velocity correlation, which is highly correlated (>0.8) as it is sine-dependent and Λ presents low values. On the other side, horizontal and vertical particle velocity correlation present small values due to orthogonality.

Thus, these two extreme scenarios show that correlations among vector sensor components are variable, and receiver structures may explore vector sensor outputs according to a high/low cross-correlation assumption.

Chapter 4

Methods

Synopsis: As shown in Chapter 3, vector sensor components may be either correlated, where the vector sensor is treated as an intensity sensor, or uncorrelated, where diversity channel combining techniques may be preferable. This chapter presents receiver structures based on passive time-reversal or beam steering methods in order to take advantage of each correlation scenario. A joint beam steering and passive time-reversal receiver structure is then proposed since, in practice, vector sensor channel correlation may present intermediary values. By quantifying and comparing such receiver structures, this work seeks to contribute to the understanding of advantageous ways to combine the vector sensors components.

4.1   Vector sensor passive time-reversal

Figure 4.1 shows the receiver structure, named vs-ptr. This receiver comprises noise normalization, Doppler compensation, time-reversal convolution, and a multichannel decision feedback equalizer (DFE). In the following diagrams and expressions, it is considered that each vector sensor has four outputs, although, for 2D vector sensors, only two directional components are considered, which may be the two horizontal components (x,y) or one horizontal and one vertical, depending on the vector sensor orientation.
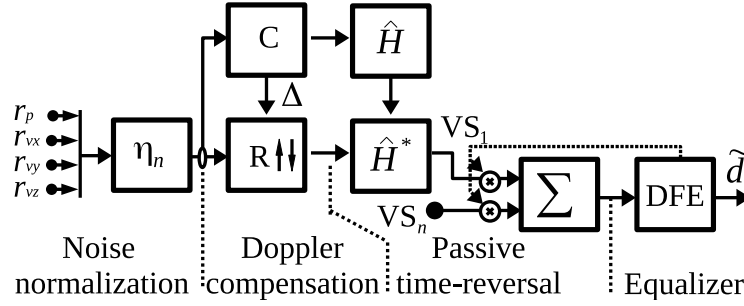
Figure 4.1: Vector sensor passive time-reversal receiver. $\hat{H}$ is the estimated channel impulse response, and $[]^*$ stands for conjugate. Notice that the four matched-filter outputs are drawn as a single path for each vector sensors.

The first step shown in Fig. 4.1 is noise normalization. Analytic expressions for spherical isotropic noise show that noise on vector sensor channels is uncorrelated, and ideally, noise power for the pressure component is equal to the sum of particle velocity noise power [57]. However, vector sensor noise caused by flow-induced, turbulence, or self-noise (e.g., electronic) generally makes the isotropic assumption inconsistent [64]. Moreover, difficulties arise due to non-isotropic noise originating from non-acoustic interference, which may completely degrade the radiation pattern and, consequently, the directional gain of vector sensors [63]. While vector sensor noise analysis can be performed with experimental data, a *priori* noise statistics prediction is a challenging task [72]. Moreover, when it comes to vector sensors, another noise issue regards the sensors' technology, in which pressure-gradient and accelerometer-based have different sensitivity [34, 64].

Thus, in practice, noise analysis in experimental data is needed, and normalization is advantageous to reduce noisy channels' degradation. One possible normalization approach is to use the output noise variance [58], which is estimated using a training sequence, the estimated CIR, and the received signals. However, since CIR estimation may depend on the configuration setup (replica, windowing, and threshold), it may not be efficient for

noisy channels. Here, we adopt a noise normalization where the objective is to balance the channels according to the input noise variance. The noise variance is calculated in the signal bandwidth during the interval without transmission. The weight (η) for the n-th channel is given by:

$$\eta_n = \frac{\frac{1}{\sigma_n^2}}{\sum_{i=1}^{N} \frac{1}{\sigma_i^2}}, \tag{4.1}$$

where σ_i^2 is the noise power of the i-th vector sensor component with N channels. The result of (4.1) can be equivalently obtained by the maximum likelihood estimation (MLE) (see Appendix A). The effect of this denoising approach is felt in the radiation pattern, which tends to a cardioid-like pattern [73].

The second step is Doppler compensation. Phase tracking and correction using estimated channels and hard decision past symbols have been used for Doppler compensation [58, 74]. However, that approach needs a training sequence that is too long (1600 symbols) for the used signal transmitted. Thus, another method that requires a shorter training sequence is used.

Here, the approach is based on the ambiguity function method using a block Doppler estimation [75]. A bank of correlators, represented as C in Fig. 4.1, is used to estimate the CIR. Interleaved m-sequence packets are used as replicas in this estimation, and the time compression/expansion (Δ) is estimated between two subsequent packets. In practice, the use of one horizontal particle velocity component to estimate Δ is preferable instead of all channels. This avoids possible fluctuation in the Δ estimation caused by late arrivals [73].

The third step in Fig. 4.1 is the passive time-reversal. PTR has been used in vector sensor receivers as an attempt to explore diversity [58, 59]. Diversity provided by a single vector

sensor is interpreted as spatial diversity by authors [59, 74]. However, spatial diversity is usually referred to spatially separated sensors (i.e., spacing longer than a wavelength) [13], which is not the case of a single vector sensor. The inherent directionality of vector sensor components (or orthogonality) shown in the correlation analysis (see section 3.3) is the key of vector sensor diversity. The n-th matched-filter output is given as:

$$p_n(t) = \hat{h}_n^*(-t)z_n(t). \tag{4.2}$$

where z_n is the n-th Doppler compensated component (i.e., z_p, z_{vx}, z_{vy}, and z_{vz}, respectively). The last step in Fig. 4.1 is a multichannel decision feedback equalizer (DFE) used for ISI mitigation, which has shown advantages when used with the PTR structure [76]. A second-order phase-locked loop (PLL) is embedded in the DFE for carrier-phase tracking. Moreover, an adaptive recursive least-square (RLS) algorithm is used to update the coefficient of N feed-forwards and one feedback filter [3]. Although the standard RLS is being used here, future optimization approaches may explore directional channels as cost functions in the adaptive process. The DFE soft output can be written as:

$$\hat{d}(k) = p(k) + q(k) = \sum_{n=1}^{N} \mathbf{w}_n^{\text{ff}}(k)\mathbf{p}_n(k)e^{-j\delta_n} + \mathbf{w}^{\text{fb}}(k)\tilde{d}(k), \tag{4.3}$$

where $\mathbf{w}^{\text{ff}}$ and $\mathbf{w}^{\text{fb}}$ are the feed-forward and feedback coefficient vectors, δ_n is the estimated carrier-phase, and $\tilde{d}$ is the hard decision output. The RLS adaptation is performed by calculating:

$$
\begin{aligned}
e(k) &= d(k) - \hat{d}(k), \\
\mathbf{K}(k) &= \frac{\mathbf{U}(k-1)\mathbf{y}(k)}{\lambda + \mathbf{y}^H(k)\mathbf{U}(k-1)\mathbf{y}(k)}, \\
\mathbf{U}(k) &= \frac{\mathbf{U}(k-1) - \mathbf{K}(k)\mathbf{y}^H(k)\mathbf{U}(k-1)}{\lambda}, \\
\mathbf{w}(k) &= \mathbf{w}(k-1) + \mathbf{K}(k)e^H(k),
\end{aligned}
\tag{4.4}
$$

where e is the error, d is the known training symbols ($\tilde{d}$ is used for running mode), and the vector $\mathbf{K}$ is the Kalman gain [3]. $\mathbf{U}$ is a matrix initialized as $\gamma\mathbf{I}$, where $\mathbf{I}$ is the identity matrix and γ is an empiric real value. The vector $\mathbf{y}$ is composed of input signals, $\mathbf{p}_n e^{-j\delta_n}$ and $\tilde{d}$, in which $\mathbf{y} = [\mathbf{p}_1 e^{-j\delta_1}, \cdots, \mathbf{p}_N e^{-j\delta_N}, \tilde{d}]^T$. λ is the RLS forget factor, and $\mathbf{w} = [\mathbf{w}_1^{\mathrm{ff}}, \cdots, \mathbf{w}_N^{\mathrm{ff}}, \mathbf{w}^{\mathrm{fb}}]^T$. The carrier-phase is estimated according [9]:

$$\Phi_n(k) = \Im\{p_n(k)[d(k) - q(k)]^H\},$$

$$\delta_n(k+1) = \delta_n(k) + \mathrm{k}_P\Phi_n(k) + \mathrm{k}_I\sum_k \Phi_n(k), \tag{4.5}$$

where $\Im$ stands for the imaginary part, and k_P and k_I are proportional and integral constants, respectively.

In Fig. 4.1, the steps from noise normalization to PTR are illustrated only for a single vector sensor, although the multichannel DFE is also used for combining more than one vector sensor. This receiver structure, removing the noise normalization stage, can also be employed for a pressure-only array, which in that case is called p-ptr.

One can notice that the vs-ptr stage should enhance the signal-to-noise ratio (SNR) and mitigate ISI, where the advantage comes from the intrinsic directionality of the vector sensors components. However, except for the noise normalization stage, this structure can be considered as a standard receiver structure, where the source direction information is not used. Thus, the following section presents another pre-processing option that uses the steerability of vector sensors.

4.2 Vector sensor beam steering

This receiver structure is based on beamforming, which by combining correlated signals and uncorrelated noise enhances SNR [68]. The objective is to form beams, which results in

directional gains [34, 77]. Fig. 4.2 shows the receiver, named vector sensor beam steering (vs-

bs). The structure is composed of noise normalization, Doppler compensation, beam steering,

Figure 4.2: Vector sensor beam steering receiver. Pressure and horizontal particle velocity components are used to estimate azimuth angle $\hat{\theta}_0$. Three elevation angles are chosen ($\phi_k = -90°, 0°, 90°$), and three outputs are produced using the direction ($\hat{\theta}_0$, ϕ_k).

and multichannel DFE. Compared to the vs-ptr, the difference is the steering, which is

performed by combining weighted vector sensor components. The k-th output is given

by [40]:

$$y_k = z_p + z_{vx}\cos(\phi_k)\cos(\theta_0) + z_{vy}\cos(\phi_k)\sin(\theta_0) + z_{vz}\sin(\phi_k) = \mathbf{z}_n \begin{bmatrix} 1 & \mathbf{u}_k \end{bmatrix}^T, \qquad (4.6)$$

where, $\mathbf{u}_k = [\cos(\phi_k)\cos(\theta_0), \ \cos(\phi_k)\sin(\theta_0), \ \sin(\phi_k)]$. Thus, the weights are scalar values

calculated according to chosen angles. Here, DoA estimation is used to provide the azimuth

angle θ_0, whereas three elevation angles are fixed ($\phi_k = -90°, 0°, 90°$). Note that using

these elevation angles is equivalent to steer to surface ($\phi_0 = -90°$), source direction θ_0

with $\phi_0 = 0°$, and bottom ($\phi_0 = 90°$). The option of using DoA to estimate the elevation

was discarded for two reasons: first, steering to the source direction (in terms of elevation)

does not necessarily result in a minimum error for communications [78]; second, it was

already shown that conventional DoA estimation methods, such as intensity-based, Bartlett,

minimum variance distortionless response (MVDR), in a multipath environment, may not

provide accurate elevation angles [77].

The advantage of those three beam steering outputs is that we are providing combinations, as input for the equalizer, assuming a high correlation between pressure and vertical components, or pressure and the horizontal component (in the estimated source direction). For a moving source, the DoA provides an accurate estimation angle, which benefits SNR. Here, the Bartlett estimator is used, where the beam response in the f center frequency is given as:

$$\mathbf{B}(f, \theta) = [1 \ \cos\theta \ \sin\theta]^H \ \mathbf{R}(f) \ [1 \ \cos\theta \ \sin\theta], \tag{4.7}$$

where $\mathbf{R}(f) = \frac{1}{L}\sum_{f-\Delta f/2}^{f+\Delta f/2}[Z_p \ Z_{vx} \ Z_{vy}]^H[Z_p \ Z_{vx} \ Z_{vy}]$ is the data estimated cross-correlation matrix in the frequency domain, in the Δf bandwidth with L samples, where $Z \equiv Z(f)$. The estimated azimuth source direction angle is given by:

$$\hat{\theta}_0(f) = arg\max_\theta \mathbf{B}(f, \theta). \tag{4.8}$$

A final aspect to be noticed is that the number of steered outputs could be increased or decreased, or a single output is generated where the steering angle is dependent on an optimization process, as shown in [73, 78]. However, such optimization approach is outside the scope of a low-power consumption application since a high computational requirement is needed. Thus, motivated by the correlation hypothesis and simplicity, the option for generating the three outputs is adopted.

4.3 Joint vector sensor beam steering and passive time-reversal

The two previous receivers may present different performances depending on signal coherence. Whereas PTR can be seen as a generalized beamformer (matched to the channel),
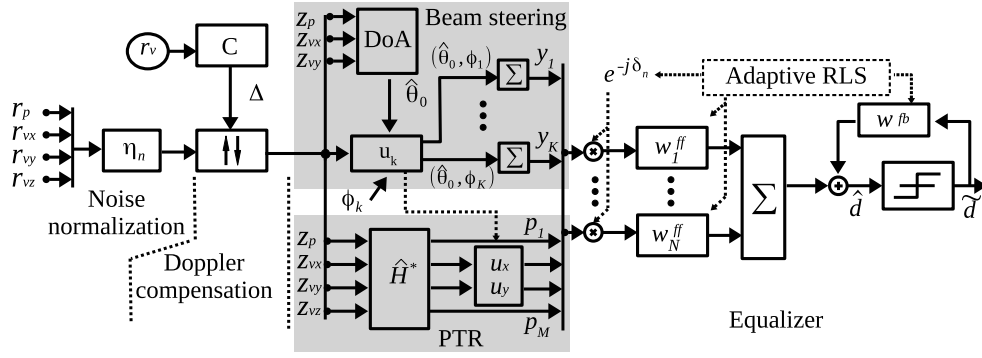
Figure 4.3: Joint vector sensor beam steering and passive time-reversal receiver structure for a single vector sensor. Input signals are pressure (r_p) and pressure-equivalent particle velocities (r_{vx}, r_{vy}, r_{vz}). In the beam steering segment, pressure and horizontal particle velocity components are used to estimate azimuth angle $\hat{\theta}_0$. Three elevation angles are chosen ($\phi_k = -90°, 0°, 90°$) and three outputs ($K = 3$) are produced using the directions $(\hat{\theta}_0, \phi_k)$. In the PTR segment, $\hat{H}$ is the estimated channel impulse response and * stands for conjugate. N feed-forwards and a single feedback filter are w_n^{ff} and w^{fb}, respectively, δ_n are phase-carries from PLL, and $\hat{d}$ and $\tilde{d}$ are soft and hard decision symbols, respectively.

beam steering provides a directional gain under the plane wave assumption. Thus, in theory, PTR should bring the best performance since the matched filter is the optimum receiver in additive white Gaussian noise (AWGN) that maximizes SNR. However, since there is no *a priori* knowledge of the channel, estimation errors may degrade performance. Moreover, using components of a 3D vector sensor indiscriminately in the PTR may not be a proper approach. For instance, if a sound wave arrives in the direction of one horizontal axis, this sound wave is substantially attenuated in the orthogonal axis direction, and thus, one horizontal component would simply add noise to the PTR without any benefit. Thus, we may think that a specific design for vector sensors, taking advantage of the directional information, could enhance performance in that case. For instance, by applying variable gains for the horizontal directional components in order to emphasize components in the source direction.

Figure 4.3 shows the proposed joint vector sensor beam steering and passive time-reversal

receiver structure (vs-bsptr), which puts together the previous two receivers. The idea is to take advantage of highly correlated channels by using the vector sensor beam steering and explore diversity by vs-ptr. For the vs-ptr segment, we employ a soft normalization, using the azimuth weights estimated for the beam steering. This approach attenuates possible noisy horizontal components. The n-th adapted PTR output ($m = 1 : M$, where $M = 4$) is given as:

$$p_m(t) = \hat{h}_m^*(-t)z_m(t)u_m. \tag{4.9}$$

where $u_m = 1$, for $m = 1$ and $m = 4$ (pressure and vertical particle velocity components), $u_m = u_x = \cos(\hat{\theta}_0)$ for $m = 2$, and $u_m = u_y = \sin(\hat{\theta}_0)$ for $m = 3$. z_m represents the Doppler compensated signals, where m from 1 to 4 are the pressure and particle velocity components (i.e., z_p, z_{vx}, z_{vy}, and z_{vz}), respectively. One can note that, since the multichannel DFE is also used for combining multiple vector sensors, the number of feed-forwards in total, N, is seven times the number of used vector sensors.

Compared to the previous two structures, the joint structure is expected to present robustness along the range. This expectation is based on the hypothesis that the vector sensor channel correlation varies along the range, as presented for extreme scenarios in section 3.3, and the vs-ptr and vs-bs together can handle a variable channel correlation. For instance, both pressure and horizontal particle velocity are uncorrelated to vertical particle velocity in long ranges, whereas the pressure component may be correlated to the vertical component at short-range. Such correlation aspects may favor the vs-ptr or beam steering segment depending on the source-receiver range, e.g., even if no channel diversity is found, the joint method would only take advantage of the beam steering, and the performance is not expected to degrade.

Chapter 5

Simulation and experimental results

Synopsis: *This chapter presents the main results by quantifying communication perfor-mance for the presented receiver structures. Data from two field experiments are analyzed us-ing either a three-axial accelerometer-based vector sensor array or a two-dimension pressure-gradient vector sensor. Section 5.1 shows results for the Makai experiment, where a point-to-point communication link between a vector sensor array tied to a ship and a bottom sound source is analyzed. A case study using simulated data based on the experiment provides an initial insight into the expected performance, which then is verified using real data. Finally, Section 5.2 shows results for the EMSO experiment, where a 2-D vector sensor is placed on the bottom and transmissions are made from a sound source tied to a ship.*

5.1   Makai Experiment

This section presents results and discussions for the tested receiver structures using a dataset from the Makai experiment (MakaiEx). Such analysis is also reported in a more compact format in [79]. The MakaiEx experiment was a four-week field experiment, which took place off the coast of Kauai Island, Hawai, in 2005. The present work analyzes the communication data from a test performed on September 23 rd, which started at 19h22 local time. A vector

sensor array (VSA) was deployed for receiving acoustic signals for various objectives, such

as DoA, source localization, geoacoustics, and communications [58, 73, 80]. The VSA used

in the experiment was composed of five vector sensors model TV-001 (Wilcoxon Research

Inc.). Due to technical issues, the closest to the bottom vector sensor did not work properly

during the experiment, thus, only data from the other four vector sensors was available. The

acquisition system had no pre-amplifier, and the raw data was sampled with a 24-bit dynamic

range at 48 kHz. Fig. 5.1 (a) shows the VSA used during MakaiEx. Each vector sensor is
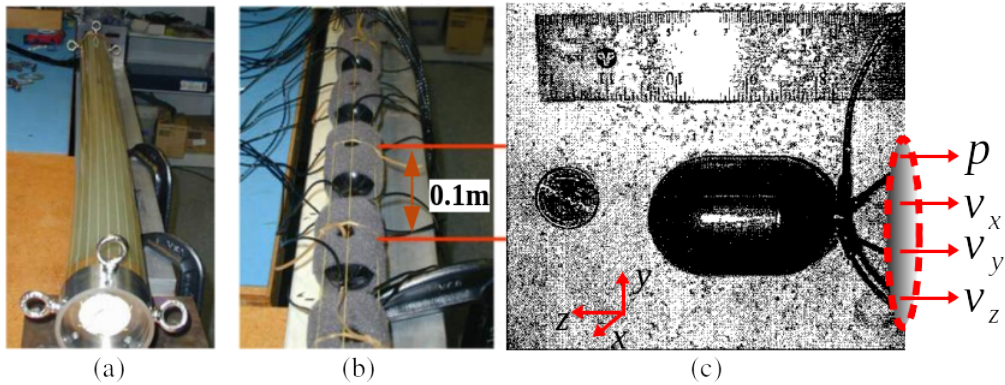
Figure 5.1: Three-axis accelerometer-based vector sensors model TV-001: enclosed inside a
flexible cylinder shell (a); covered by a synthetic foam and spaced of 0.1 m (b); size-compared
to a quarter dollar coin with pressure and particle velocity components (c).

covered by a synthetic foam, and the array is enclosed inside an oil-filled cylindrical shell

with a spacing of approximately 0.1 m, as shown in Fig. 5.1 (b). Fig. 5.1 (c) shows a single

vector sensor, which is composed of three uni-axial accelerometers and one omnidirectional

hydrophone. These are encapsulated in neutrally buoyant resin, forming a $3,81 \times 6,35$ cm

cylinder-type.

During the communication test, the VSA was suspended by a cable from the research

vessel Kilo Moana's stern, which was set in drift mode. Fig. 5.2 (a) shows the ship track over

the MakaiEx area bathymetry, which varies from 80 to 300 m in water depth. Source-receiver

ranges vary from approximately 20 m to 1.5 km, and two receiving intervals highlighted in (a),
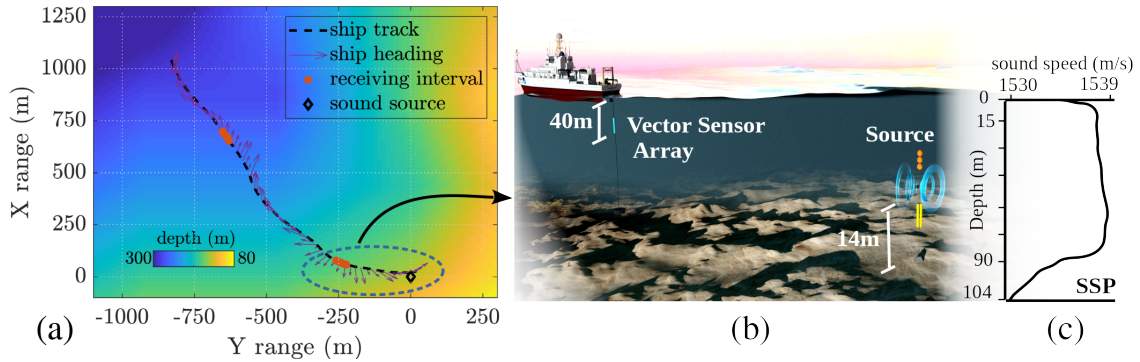
Figure 5.2: MakaiEx scenario: ship trajectory over X-Y area bathymetry centered at sound source position (22.1660 N;-159.7870 W), and receiving intervals (red dots) (a); vector sensor array tied at the ships' stern, sound source at approximately 90 m depth (b); and the sound speed profile (c).

at 230 and 907 m range, are used for testing and validation of the receiver structures. The x-axis reference is set to North, where the azimuth angle θ is measured clockwise from the x-axis, and the axis origin is at the sound source position (22.1660 N;-159.7870 W). The ship-track and ship-heading show that the vessel spun around itself in free drift. For analysis, we consider that the VSA does not have a yaw moment (spin around the vertical axis), i.e., it kept the same relative bearing to the ship's heading. In Fig. 5.2 (b), a lateral view shows the VSA tied to the ship's stern and the bottom moored sound source. The VSA was kept at approximately 40 m depth, where a 100-150 kg weight was used at the bottom extremity of the cable to keep the VSA as straight and vertical as possible. The bottom-moored sound source was placed at 90 m depth, where the local water column depth is 104 m. Fig. 5.2 (c) shows the sound speed profile, where the speed decreases by about 10 m/s from 80 m to the sea floor.

The spectrogram of Fig. 5.3 (a) shows several received signals at specific timestamps from participating institutions. The signals analyzed here were the sequences marked as UALg in Fig. 5.3 (a), and refer to minutes 52 and 112. The transmitted signal is a binary phase-shift
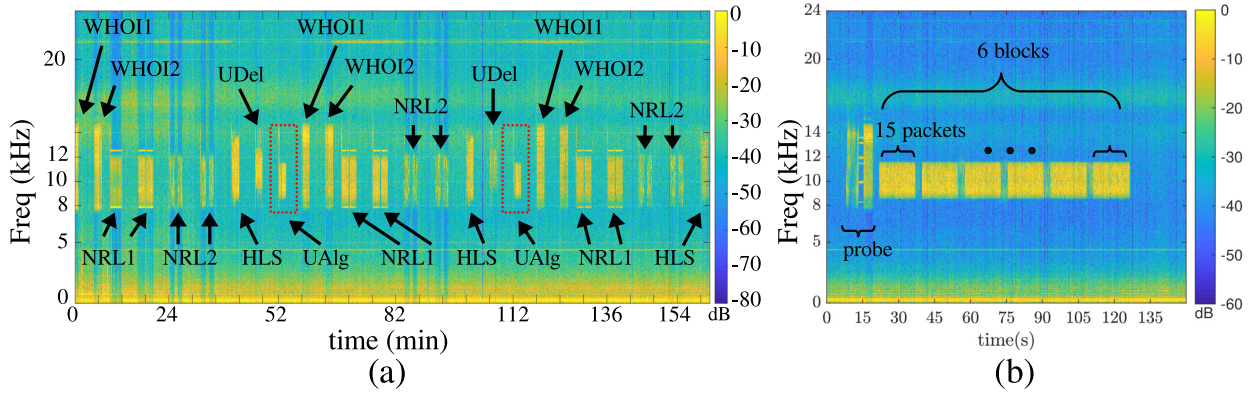
Figure 5.3: Spectrogram for pressure component of vector sensor 4: during the overall communication test on September 23 rd (a); and during the first UAlg receiving interval starting at min 52 (b). Woods Hole Oceanographic Institution (WHOI), U.S Naval Research Laboratory (NRL), Heat, Light, & Sound Research, Inc. (HLS), University of Delaware (UDel), and University of Algarve (UAlg) are the participating institutions.

keying (BPSK), in the carrier frequency of 10 kHz and with an effective bandwidth of 3 kHz, filtered by a square-root-raised-cosine pulse shape with a roll-off factor of 0.5. Fig. 5.3 (b) shows the spectrogram of the UAlg received signal in higher detail. This communication signal is composed of a main probe and 6 blocks, where each block contains fifteen packets of 1 s. Each packet contains 2000 symbols, the first 255 of which contain a m-sequence, used for Doppler compensation and time synchronization.

5.1.1   Case study simulation

Due to the potential complexity of working with real data and the variability of the underwater acoustic channel, it was important to first demonstrate that our receiver structures worked as expected on simulated data. Thus, the following case study simulation serves as a first test of the receiver structures. This test is especially important for those structures that depend on CIR estimation, where estimation errors in experimental data may impact the performance. The acoustic scenario is simulated using the Ocean Acoustic and Seismic Exploration Synthesis - OASES numerical model [81], where pressure, horizontal, and vertical

particle velocity CIR are estimated for discrete ranges from 100 to 1100 m. The simulation

uses the sound speed profile (SSP) measured during MakaiEx, as shown in Fig. 5.2 (c), and

the bottom properties shown in Table 5.1.

Table 5.1: MakaiEx bottom acoustic properties used in OASES model (from [48]).

Layer	Thickness(m)	$\rho(\mathrm{g}/cm^3)$	c_p(m/s)	c_s(m/s)	α_p(dB/λ)	α_s(dB/λ)
First	0.175	1.6	1570	67	0.6	1.0
Second	20	2.1	1700	700	0.1	0.2
Sub	$\cdots$	2.1	2330	1000	0.1	0.2

Figure 5.4 (a) shows the estimated CIR for pressure along range. The first arrival (5 ms)

is the direct path, followed by the bottom-bounce, surface-bounce, and bottom-surface

reflection. One can notice that late arrivals, from surface and bottom reflections, become

closer to the first arrival as the range increases, which is an expected result for the source-

receiver geometry. Fig. 5.4 (b) and (c) show the CIR of pressure (p), horizontal particle

velocity (v_y), and vertical particle velocity (v_z), normalized to unitary power, for 250 and

900 m, respectively. In Fig. 5.4 (b), pressure and horizontal particle velocity CIR present

similar amplitudes. Moreover, the first arrival amplitude is larger than late arrivals (i.e.,

minimum phase [82]). Contrarily, the vertical component has the highest amplitude for the

third arrival, which is expected since the surface reflection arrival has a steeper angle of

arrival (AoA). In Fig. 5.4 (c), the third arrival has a higher amplitude than the first one for

all components, which is probably due to the beginning of a "shadow zone" for direct paths

at this range, while the later (and steeper) arrival is still strong at this range due to the

sound refraction due to a non-isovelocity SSP.

Table 5.2 shows the RMS delay-spread (DS) and the cross-correlation among vector sensor

channels (see [83] for correlation and [84] for DS calculations). Results of Table 5.2 were
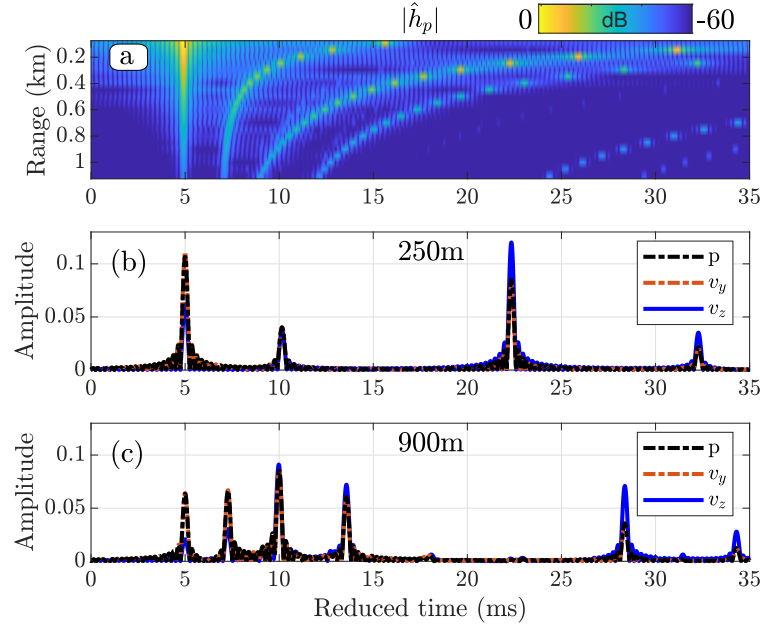
Figure 5.4: Channel impulse response for pressure versus range (a), and for pressure and particle velocity components (v_y, v_z) for 250 m (b) and 900 m (c).

obtained using a 35 ms window, as presented in Fig. 5.4. The horizontal particle velocity DS (DS-y) presents lower or equal values than the pressure DS (DS-p) for all calculated ranges. This is due to steeper paths being attenuated by dipole response of y-component, while the pressure channel has omnidirectional response. Considering DS as a channel severity measure, using the horizontal particle velocity component may be advantageous to the pressure component. Values of vertical particle velocity DS (DS-z) are lower than DS-p/DS-y for ranges from 250 to 550 m, but higher at other ranges. This can be related to steeper AoA at shorter ranges (<250 m), and late arrivals at longer ranges (>550 m).

Correlation between pressure and the horizontal particle velocity channel (C^{py}) shows values over 0.99, indicating high similarity, as predicted in section 3.3. Table 5.2 also shows the correlation between pressure and the vertical particle velocity channels (C^{pz}), and the particle velocity cross-correlation (C^{yz}). One can note that $C^{pz} \approx C^{yz} \approx 0.6$ for short ranges (<250 m). For other ranges, correlation becomes lower (<0.5), which is also an

expected result, according to the analysis of section 3.3.
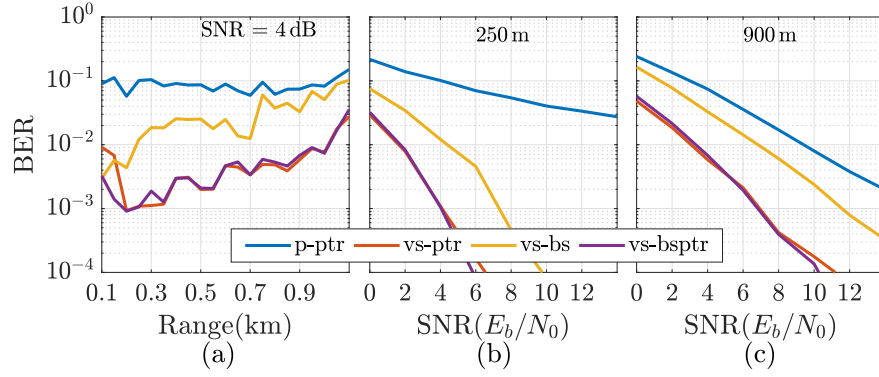
Figure 5.5: One pressure sensor and a single vector sensor comparison. BER versus range (a), and BER versus SNR for 250 m (b) and 900 m (c). p-ptr represents a single pressure sensor followed by PTR and equalizer; vs-ptr is the standard PTR using vector sensor channels; vs-bs is the beam steering method; vs-bsptr is the proposed joint method.

Figure 5.5 shows communication performance using bit error rate (BER) analysis: along range for fixed $SNR = 4\,dB$ (a) and versus SNR at ranges of 250 m (b) and 900 m (c). The tested receivers are: PTR using a single pressure component (p-ptr); standard PTR using the three vector sensor components (vs-ptr); beam steering (vs-bs); and the joint method (vs-bstpr). In this simulation, the transmitted signal with the MakaiEx setup was used, filtered by the CIR provided by OASES numerical model. Noise normalization, Doppler compensation, and the PLL were not used in the simulation. The number of feed-forward and feedback filters are set to 15 and 10, respectively, where the fractionally spaced equalizer

Table 5.2: RMS delay spread (DS-*) and vector sensor channel correlation (C^*) for several source-receiver ranges. Delay spread and correlation are calculated for/between pressure (p), horizontal (y) and vertical (z) particle velocity components.

Range (m)	100	250	400	550	700	850	1000
DS-p (ms)	14.25	9.72	7.71	6.87	8.78	8.84	9.05
DS-y (ms)	13.21	9.63	7.71	6.83	8.67	8.76	8.99
DS-z (ms)	15.10	9.36	7.23	6.68	10.22	10.06	9.51
C^{py}	0.99	1.00	1.00	1.00	1.00	1.00	1.00
C^{pz}	0.57	0.61	0.52	0.46	0.35	0.31	0.33
C^{yz}	0.61	0.64	0.53	0.46	0.36	0.31	0.34

has oversampling factor of 2. Furthermore, when PTR is used, CIR estimation is performed using a window duration of 35 ms.

In Fig. 5.5 (a), the performance of p-ptr is approximately 8%, whereas using a single vector sensor with PTR (vs-ptr), the error becomes lower than 1.5% at all ranges. The vs-ptr performance is better than vs-bs in general, except for short ranges (<150 m), where the correlation between pressure and vertical particle velocity channels is high. One can notice that such results were obtained using the CIR from OASES, and thus, it was expected that some variation could be present in the performance along range. Moreover, the equalizer parameters are kept the same for all tested ranges. This result suggests that the vs-bs may be better suited for short ranges than the vs-ptr. The vs-bsptr maintains the vs-ptr advantage when diversity can be explored at longer ranges and beamforming for shorter ranges, presenting errors lower than 1.5%, even for low SNR (4 dB). The BER versus SNR analysis of Fig. 5.5 (b) and (c) shows that using vs-bsptr, errors are lower than 10^{-4} for SNR > 6 dB at 250 m, and SNR > 10 dB at 900 m.

Although vs-bs shows higher errors than both vs-ptr and vs-bsptr, we should be aware that imprecision in the channel estimation can degrade performance of PTR in experimental data. Moreover, one can notice that azimuth estimation was not taken into account for the simulation, which is a vs-bs benefit. Thus, based on the simulation results, for the experimental data, we expect: an advantage of vs-bs in shorter ranges, boosted by the azimuth gain; a penalty in the PTR performance due to channel estimation imprecision; and a robust performance for vs-bsptr, taking advantage of both approaches. Thus, these simulation results serve, at least, to provide insight into the performance, which agrees with the theoretical assumption that beamforming may be more advantageous at shorter ranges

and diversity at longer ranges.

5.1.2 Experimental data analysis

For experimental data, we analyze 90 packets transmitted at 230 and 907 m source-receiver ranges. Each packet lasts 1 s and has 2 k symbols, in which the first 255 symbol m-sequence is used for Doppler compensation and channel impulse response estimation. The forget factor $\lambda = 0.998$, proportional and integral factors, $k_P = 0.01$ and $k_I = 0.001$, were set in RLS and PLL, respectively. These values are used for both ranges to check robustness empirically. The number of feed-forward and feedback filters, for a fractionally spaced equalizer, are 30 and 10, respectively. The BER is used to quantify performance for experimental data.
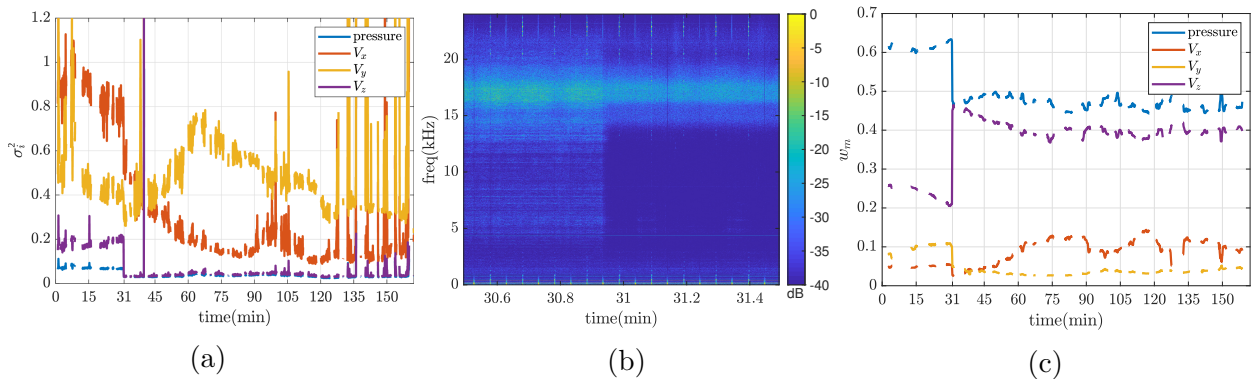
Figure 5.6: Denoising analysis. Estimated noise power (a); spectrogram for the vertical component of vector sensor 4 (b); and denoising weights (c).

The noise normalization (or denoising) analysis is done using Fig. 5.6. A high noise power variation due to the ship's self-noise (dynamic positioning system and auxiliary machinery) was not expected. However, Fig. 5.6 (a) shows a large power difference for the data until minute 31 compared to the rest of the data. The ship noise power was estimated with the following procedure [85]: the power is estimated for the 4 pressure channels in broadband; the average power of the 4 pressure channels is used for selecting the interval that corresponds to signal (during transmissions) and ship (intervals without transmission); a 5 dB threshold was

empirically chosen to select the ship's interval. It is known that the ship attempted to keep a specific positioning relative to the source until around minute 30. This is indicative that the dynamic positioning system could be active. This fact is also noticed by the spectrogram of the vector sensor vertical component in Fig. 5.6 (b). This spectrogram shows a sharp noise reduction at min 30.9. The result of this sharp variation is felt by the denoising weights shown in Fig. 5.6 (c). The estimated weight used in the receiver is the mean value ignoring the initial interference.

Another specificity noted in the data is that the pressure and vertical particle velocity channels have much larger amplitudes than the two horizontal channels (not shown). Thus, the estimated weights for these components tend to balance this noise power difference. According to Fig. 5.6 (c), the weights of both pressure and vertical components are higher than the weights of horizontal components, which emphasizes the pressure and vertical components. The emphasis on the vertical component has shown benefits, especially for the beam steering approach for shorter ranges, as presented in [73].
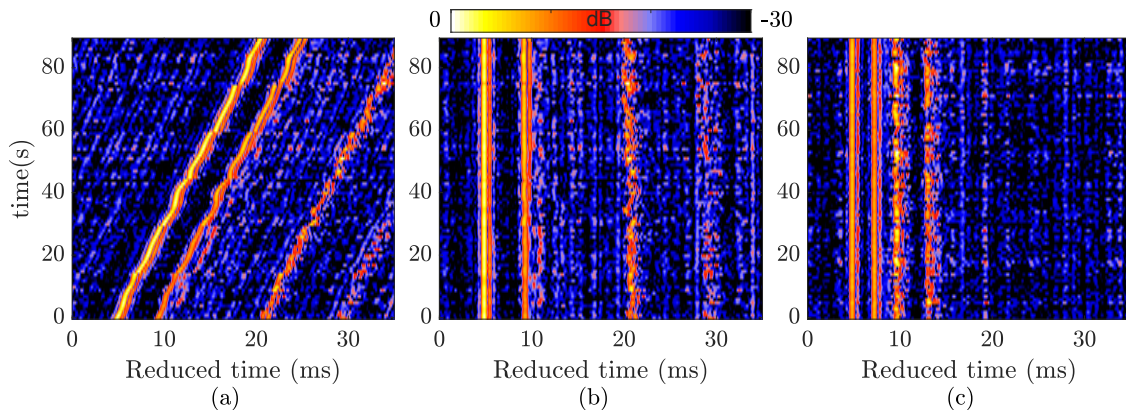
Figure 5.7: Estimated time-varying channel impulse response for y-axis of vector sensor #1 (the closest to the surface) using 255 symbols preamble, for source-receiver range of 230 m without Doppler alignment (a), and with CIR main arrival alignment at 230 m (b), and 907 m (c).

Figure 5.7 shows the estimated time-delay CIR for the y-axis of vector sensor #1, the

closest to the surface, for source-receiver ranges of 230 m (a)-(b) and 907 m (c). In Fig. 5.7 (a), the CIR is impacted by a small-scale Doppler effect caused by the ship drift. The CIR indicates that the ship is moving away from the source, and thus, a delay is verified for the arrivals. Note that some discontinuities are also seen, as there is a small gap between blocks. In Fig. 5.7 (b)-(c), the CIR alignment is performed using the first arrival. The use of the first arrival is justified by analyzing Fig. 5.8. This figure shows, for 907 m, the correlator output for two subsequent packets (a) and the estimated time for the strongest and the first arrival peaks (b). Due to similar amplitude among arrivals, the strongest peak may vary between packets, which causes a variable estimated time, as shown by the dashed lines in Fig. 5.8 (b). An uncommon late arrival is also shown in Fig. 5.8 (a) for packet 5, which can cause errors in the Doppler factor estimation. This time fluctuation issue is solved when the first arrival is chosen, as shown by full lines in Fig. 5.8 (b). Thus, the use of the first arrival was preferable to calculate the synchronization sample and the Doppler factor. Besides these estimated parameters, the time-delay CIR of Fig. 5.7 (b)-(c) does not present a strong fading effect for the first arrival, although the temporal coherence varies from 500 ms to 700 ms.

(a) (b)
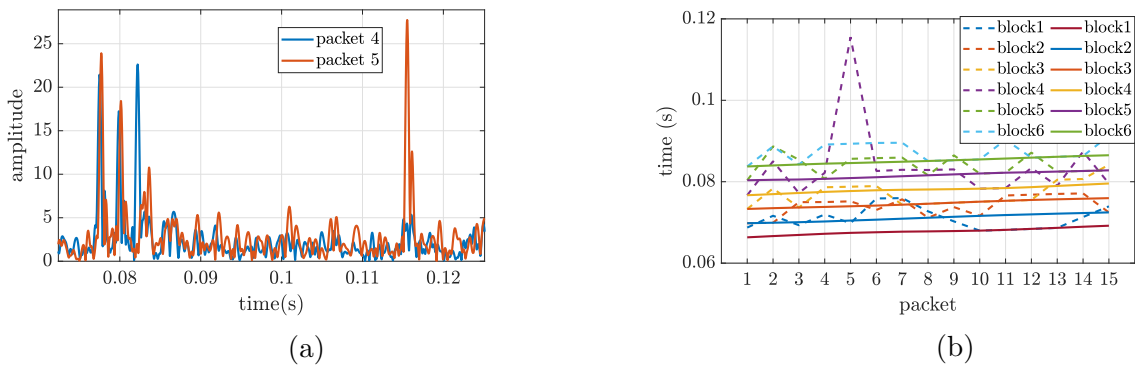
Figure 5.8: Sample synchronization and Doppler factor estimations for data at 907 m. Correlator output for packets 4 and 5, block 4 (a), and time expansion using the strongest arrival (dashed) and first arrival (b).

Figure 5.9 shows pressure and particle velocity CIR for the respective transmitted ranges
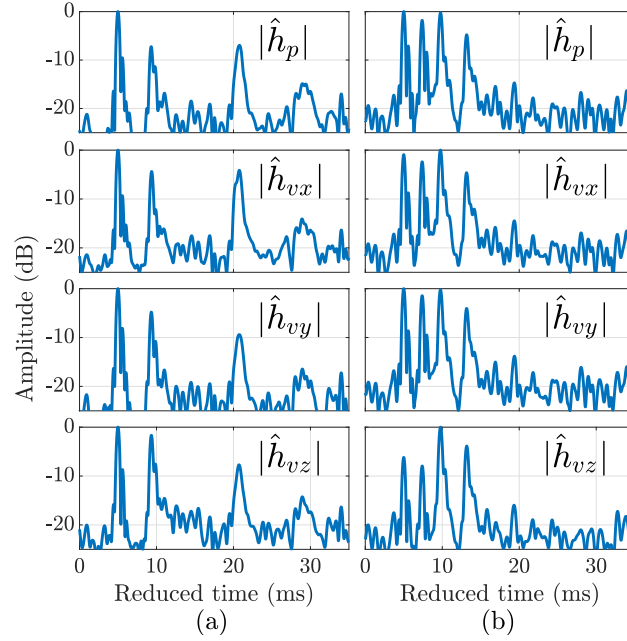
Figure 5.9: Estimated channel impulse response for pressure (p) and particle velocity channels (x,y,z) from top to bottom, for source-receiver ranges of 230 m (a) and 907 m (b).

estimated taking the 90 s time average. One can notice the ray arrival time coincidence to those predicted in simulation (see Fig. 5.4). However, the exact match in amplitude is hard to be guaranteed considering several surface and bottom effects present in real data, as noticed for the third arrival (surface reflection) difference between $|\hat{h}_{vz}|$ in Fig. 5.9 (a) and Fig. 5.4 (b). In this range, the multiple AoAs tend to be steeper than those found at 907 m, and the surface effects, such as scattering and roughness, may have a substantial impact, not considered in the simulation, which can justify the amplitude difference. For 907 m, the vertical component's amplitude $|\hat{h}_{vz}|$ shows the third arrival with a larger amplitude than the first one, as predicted in simulation. Since the vector sensor vertical component filters horizontal arrivals, the direct path is more attenuated than the surface reflection (third arrival) at 907 m. This explains the first two arrivals attenuated in Fig. 5.9 (b) for the vertical component. Moreover, comparing the CIR among vector sensor components in Fig. 5.9 (a) and Fig. 5.9 (b), the latter shows more diverse channels.
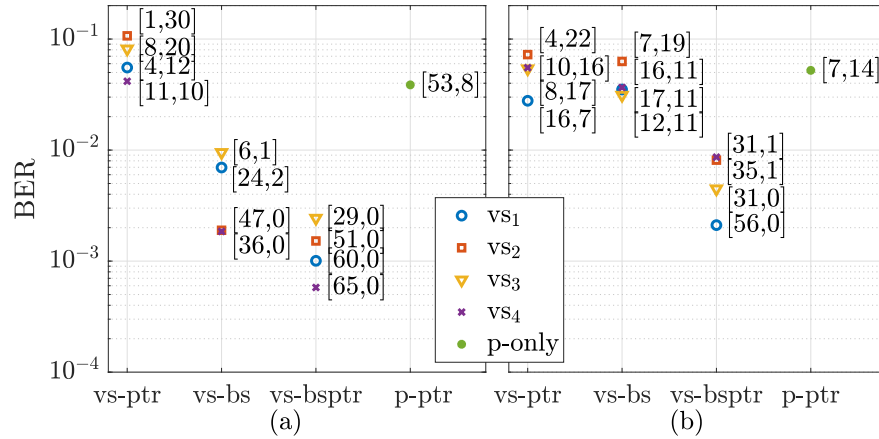
Figure 5.10: BER performance for the tested receivers for each vector sensor, for source-receiver range of 230 m (a) and 907 m (b). For reference, the pressure-only array performance (p-only, using 4 hydrophones) is shown using a standard PTR (p-ptr). The numbers next to each error represent [number of packets BER=0, number of packets BER>10%].

Figure 5.10 shows the BER performance for the tested receivers, for each vector sensor individually (vs_n), and for the four-element pressure-only array (p-only). A pair of numbers is printed next to each error. These two numbers represent, for a total of 90 packets, the number of packets with zero BER (i.e., it was not possible to measure errors for the considered number of samples) and the number of packets with BER>10%.

Figure 5.10 (a) shows the performance for 230 m range. For vs-ptr, performance varies from 4% to 10%, which is the worst performance among the tested receivers. However, the vs-ptr performance of vector sensor #4 is comparable to p-ptr, which means a size reduction improvement. Comparison between standard vs-ptr and a pressure-only array has already shown that the performance of a single vector sensor can be equivalent to a small pressure sensor array [58], and here, such performance is also seen. However, this work goes further to show that adapted structures, specifically designed for vector sensors, can enhance such performance. vs-bs presents BER from 0.2% to 1%, whereas vs-bsptr varies from 0.06% to 0.3%. For this source-receiver range, the beam steering segment is advantageous in the

vs-bsptr, resulting in the lowest error, on average, among vector sensors. In Fig. 5.10 (b), BER for 907 m range is shown, where similar performance is noticed between vs-ptr, vs-bs, and p-ptr, on average. vs-bsptr shows BER from 0.2% to 0.8% among vector sensors, which is about ten times less error than vs-ptr and vs-bs, separately. The obtained results for the tested ranges reinforce the hypothesis, predicted in simulation, that: the beamforming approach is beneficial at the shorter range; the vs-ptr approach may be degraded due to channel estimation variability; and that vs-bsptr can take advantage of both methods. An important aspect is that the performance varies up to eight times among vector sensors for the same structure. Thus, it is important to anticipate such differences in performance at individual VSA elements when analyzing and interpreting experiment data. This also suggests that we should exploit diversity when we can.
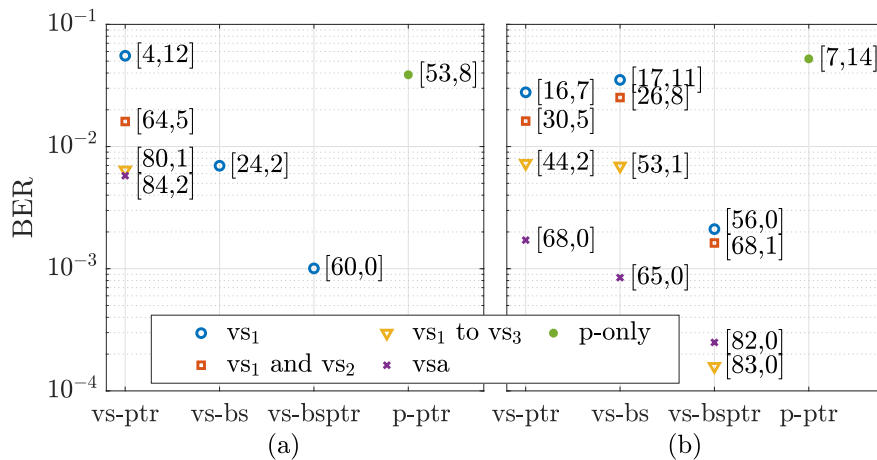
Figure 5.11: BER performance for the tested receivers combining vector sensors, for source-receiver range of 230 m (a) and 907 m (b). For reference, the pressure-only array performance (p-only, using 4 hydrophones) is shown using a standard PTR (p-ptr). The numbers next to each error represent [number of packets BER=0, number of packets BER>10%].

Figure 5.11 shows the BER performance combining the vector sensors. In this figure, performance is shown for a single vector sensor (enumerated as vector sensor #1), combining multiple vector sensors (up to four in the VSA), and the pressure-only array, for the

two mentioned source-receiver ranges. The objective now is to show the maximum achieved performance using the VSA, where we can get an insight between the array size and the performance increment. In Fig. 5.11 (a), except for vs-ptr, combining two vector sensors (vector sensor #1 and vector sensor #2) or more results in errors below 10^{-4} (not shown in the figure). These obtained results also reinforce that the beamforming approach is beneficial at this range. vs-ptr performance is improved as the number of sensors increases, which is an expected result as spatial diversity may be found among sensors of the array. Note that the vs-ptr using the VSA reduces the error from 4% to 0.5% compared to p-only, without size penalty. In Fig. 5.11 (b), vs-ptr shows similar performance to vs-bs, which indicates that diversity is better explored at this range. Combining the methods in vs-bsptr produces the best performance, which varies from 0.2% for vector sensor #1 to 0.016% for the VSA. The results also show that the joint method using a single vector sensor may outperform both vs-ptr and vs-bs using three vector sensors, which indicates the efficiency of the method since there are reductions in the number of channels for the equalizer and dimension. For instance, vs-bs produces 9 channels in total for the equalizer (3 vector sensors, each one produces 3 beam steering), vs-ptr produces 12 channels (3 vector sensors, each one produces 4 outputs), while vs-bsptr produces 7 outputs. Moreover, the length is reduced from approximately 0.3 m to 0.1 m, which is 77% of length reduction.

5.2 EMSO'21

This section presents the EMSO'21 experiment in subsection 5.2.1, signal processing and performance results for the receiver structures of chapter 4 in subsection 5.2.2, and analysis and discussions in subsection 5.2.3. A brief analysis of results using frequency-hopped

JANUS modulated signals is presented in subsection 5.2.4.

5.2.1   Experiment description

The EMSO'21 experiment took place off Vilamoura port, on the South coast of Portugal, on November 24th, 2021. In this experiment, a point-to-point communication test is performed, where the receiver is a single vector sensor placed on the bottom, and the sound source is tied to a ship. Fig. 5.12 (a) shows the satellite view of the experiment area, highlighting the ship sailing route and the vector sensor positioning (red dot). The ship used in the test is shown in Fig. 5.12 (b), which left the Vilamoura harbor at 9h00 (local) and went approximately 6 km in the South-West direction where the vector sensor was deployed. Fig. 5.12 (c) shows the Lubell-916C sound source, which transmitted signals in the band from 3 to 13 kHz. The vector sensor was attached on top of a tripod, and an autonomous recorder at one of the tripod's legs, as shown in Fig. 5.12 (d). A 10 kg weight was fixed at the tripod's center bar in order to guarantee a deployment as vertical as possible and prevent roll-over due to sea currents.

(a)   (b)   (c)   (d)
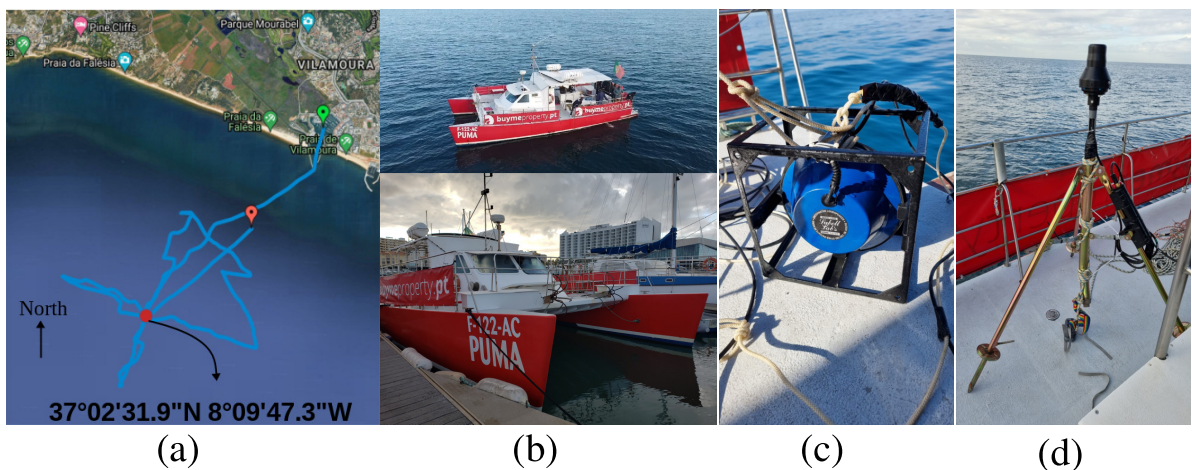
Figure 5.12: EMSO'21 experiment: satellite view with the ship sailing route and vector sensor positioning (red dot) (a); used ship (b); Lubell sound source (c); M35 vector sensor on top of the tripod, with the autonomous recorder at one of the tripod's legs (d).

The vector sensor is the two-axial pressure-gradient GeoSpectrum model M35, which measures pressure and two orthogonal directional components (x-y components) [86]. The directional components' axis references are considered true references, where the x-component is toward North and the y-component toward East. This axis compensation is performed by a clockwise rotation matrix using the North magnetic angle from an internal orientation sensor. The autonomous acquisition system was used to synchronously record the three vector sensor components (pressure, x, and y) at the sampling frequency of 39062 Hz with a 24-bit of dynamic range.

Figure 5.13 (a) shows the bathymetry in an X-Y range Cartesian plot with the vector sensor/tripod assembling position displayed at the origin (lat-lon 37.04235°N, -8.16359°W). The vector sensor was placed at approximately 2 m from the bottom, where the local water depth is 20 m. From the vector sensor deployment position, the ship goes along two tracks: leg1, which is an approximately 20 m depth isobathymetric transmission path, and leg2, which represents a downslope path. Notice that the figure's axes were established according
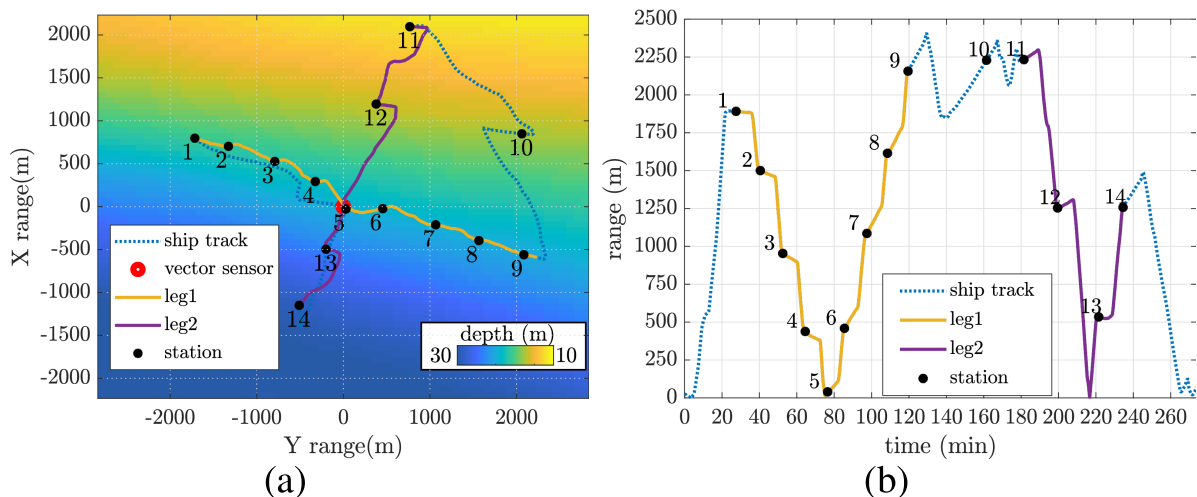
Figure 5.13: EMSO'21 experiment: ship track over area bathymetry in X-Y range centered at vector sensor/tripod position (37.04235°N, -8.16359°W), and transmitting stations (a); range between ship and vector sensor position along time (b).

to the M35 reference (x is toward North and the y toward East, with azimuth angle θ clockwise). The planned transmission stations (black dots) 1, 2, up to 14, are considered fixed stations even if small displacements were noticed due to the ship drift. In Fig. 5.13 (b), the ship to vector sensor range along time is shown, where the leg1, leg2, and the transmission stations are also highlighted. The communication signals transmitted at those stations were generated by the sound source suspended at approximately 7 m depth from a surface buoy tied at 3 m from the ship's stern. This work analyzes a binary phase-shift keying (BPSK) communication signal at 2 kbits/s data rate and carrier frequency of 5 kHz (effective 3 kHz bandwidth). Fifty packets of one second are transmitted, where each packet is a random series composed of 2000 symbols. A 255 symbol m-sequence preamble is used for synchronization and Doppler compensation. The signal is filtered by a square-root-raised-cosine pulse shape with a roll-off factor of 0.5.

5.2.2   Results

Differently from the vector sensor used in the MakaiEx, where directional outputs are particle velocity measures, the M35 outputs are pressure-difference Δp. Thus, the particle velocity components, p_v, are estimated using (2.8) with $c = 1516$ m/s and $s = 0.05$ m. A first check of the directional components (Δp or p_v) can be made by analyzing their phase, referenced
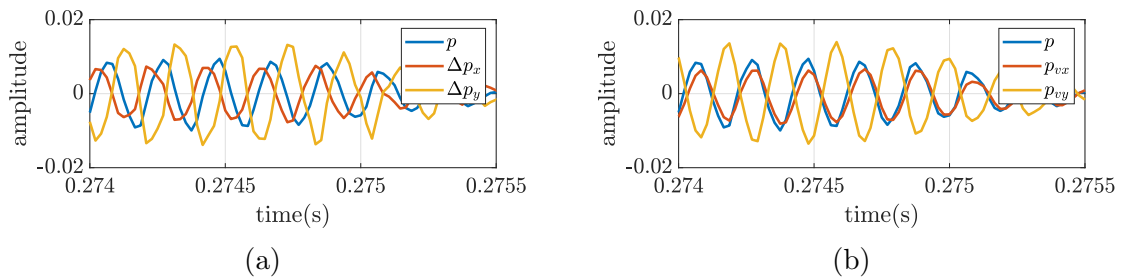
Figure 5.14: Received time series at station 3: pressure and pressure-difference channels (a); and pressure and estimated particle velocity components (b).

to the omnidirectional hydrophone. An example can be seen in Fig. 5.14, where the time series for pressure and the directional channels are shown for station 3. For Δp, a lead signal referenced to pressure represents North (for x-component) or East (for y-component), whereas a lag signal referenced to pressure represents South (for x-component) or West (for y-component). In Fig. 5.14 (a), Δp_x is lead, which represents North, whereas Δp_y is lag, representing West. Thus, it is clear that the source direction comes from the North-West quadrant. For p_v, if pressure and particle velocity are in-phase, it represents a signal from the North-East quadrant and vice-versa. In Fig. 5.14 (b), pressure and the estimated particle velocity p_{vx} are in-phase, whereas pressure and p_{vy} are in counter-phase. Thus, it represents a signal from the North-West quadrant as Δp.

The impact of the vector sensor channel combining on communications can be associated with the spatial filtering capability, analyzed here by the energy detection. Instead of the noise normalization step adopted for the accelerometer-based vector sensor in MakaiEx, here, a design factor δ is used, as presented in section 2.2. Thus, the estimated cross-correlation matrix used in (4.7) becomes $\mathbf{R}(f,\delta) = \frac{1}{L}\sum_{f-\Delta f/2}^{f+\Delta f/2}[Z_p\ \delta Z_{vx}\ \delta Z_{vy}]^H[Z_p\ \delta Z_{vx}\ \delta Z_{vy}]$. The beam response for station 3 is analyzed by varying the δ factor, where it is known that the source
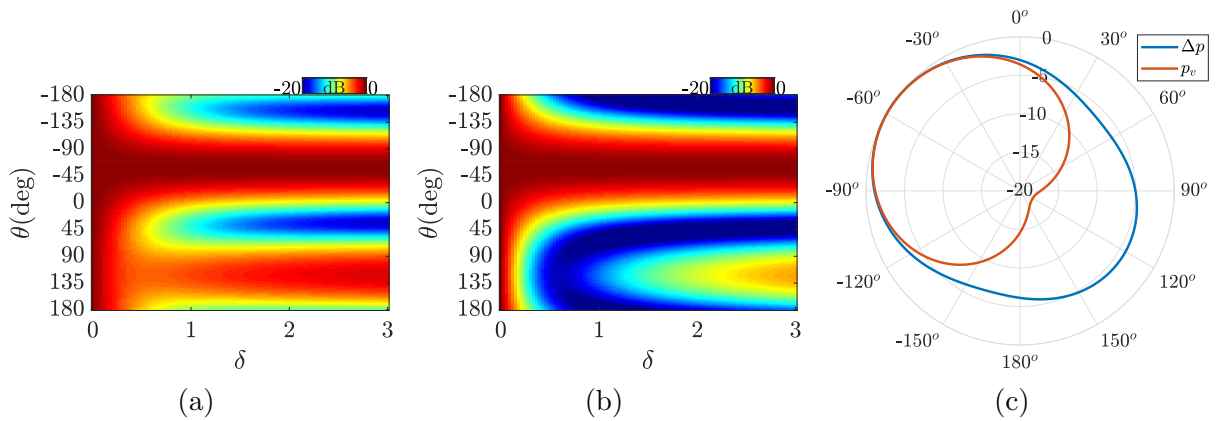
Figure 5.15: Energy detection for varying δ for station 3 using Δp (a) and p_v (b). In (c), the beam response for Δp and p_v is compared for $\delta = 0.5$.

is at approximately -60°. In Fig. 5.15 (a), Δp is used, and the main lobe is noticed in the

source direction, although ambiguity is verified as δ increases. In Fig. 5.15 (b), the ambiguity

is mitigated and the maximum ratio between the main lobe and the sidelobe is found for

$\delta = 0.5$. Fig. 5.15 (c) shows the beam response with $\delta = 0.5$ for both Δp and p_v, where the

ambiguity mitigation is apparent, and the cardioid-like shaped response is obtained. Thus,

one can conclude that the proper δ value is 0.5 for a backside ambiguity mitigation, which is

set for quantifying the communication performance. Note that p_{vx} and p_{vy} particle velocity

components are simply called x and y directional components hereafter.

Spectrograms of the received communication signals for the pressure (p), x and y-

components for stations 3 (a), 7 (b), 12 (c), and 14 (d) are shown in Fig. 5.16. The

spectrograms show the BPSK communication signals that also contain a sequence of linear

frequency modulation (chirp) as a probe for future use in automatic detection algorithms,

not treated here. The same normalization was used in the spectrograms with the objective to

show attenuated/amplified components. One can relate the power spectrum amplitude of the

components with the transmitting stations. For instance, in Fig. 5.16 (b), the x-component
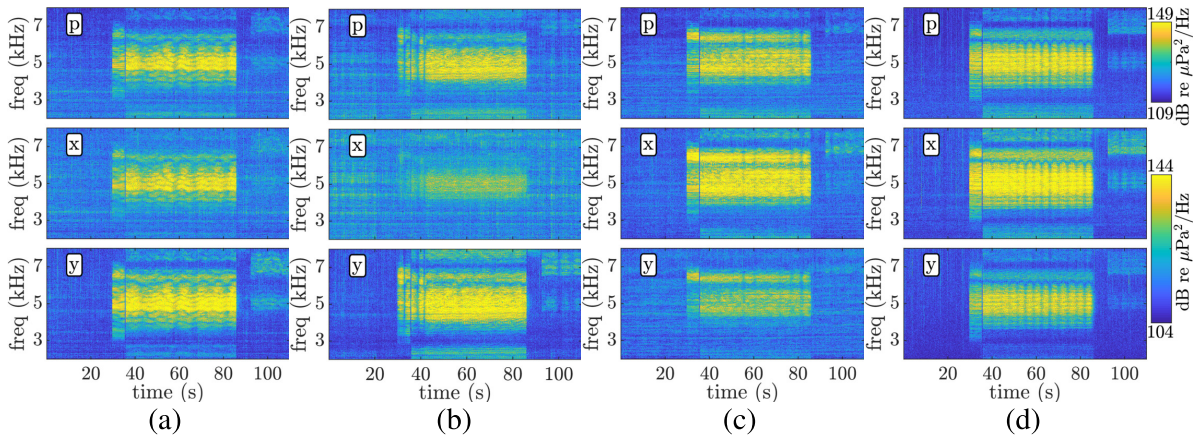
Figure 5.16: EMSO'21 spectrogram for pressure (p), x, and y components during stations 3, 7, 12, and 14, from (a) to (d), respectively.

is highly attenuated since the sound source is transmitting at approximately 100°, whereas in Fig. 5.16 (c), the y-components is the attenuated component since the sound source is emitting from North (20°).

Figure 5.17 shows the azigram of recorded data during the overall communication test (a), during stations 3, 7, 12, and 14, from top to bottom (b), and the overall energy detection (c). An azigram is a condensed way to show the directional information over frequency and time. In fact, an azigram is analogous to a spectrogram, although the latter shows the power spectral density instead of the source direction estimation as a colormap. Interested readers can find a full study on azigrams in [52] and references therein. Here, the azigram is used as an analysis tool for a first check of transmitting directions and ambiguity issues. Fig. 5.17 (a) and (b) were obtained using the Bartlett estimator, where (4.7) and (4.8) are used with a
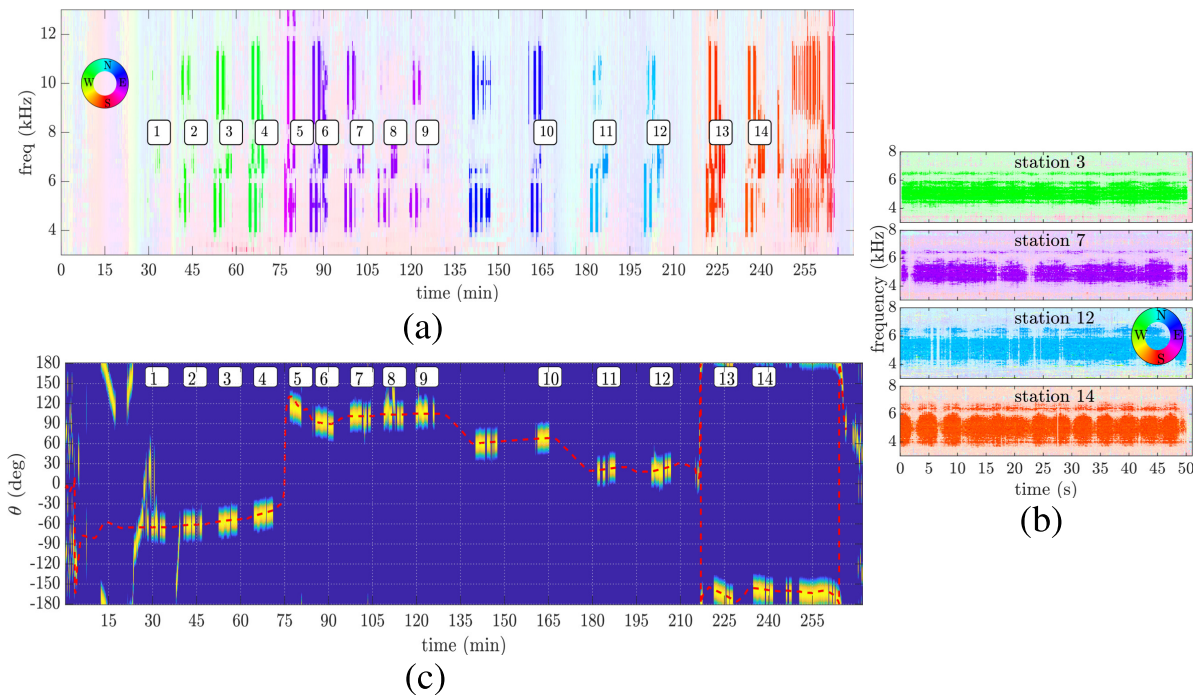
Figure 5.17: EMSO'21 azigram: during the overall communication test, where the number in boxes indicate transmitting stations (a); during transmissions at stations 3, 7, 12, and 14 (from top to bottom) (b); and energy detection using Bartlett estimator with estimated azimuth angle using GPS info (dashed red line) (c).

frequency step of $50\,\mathrm{Hz}$, $\Delta f = 100\,\mathrm{Hz}$, and integration time of $0.34\,\mathrm{s}$ (a) and $0.08\,\mathrm{s}$ (b). Alpha transparency is used for clear visualization, taking into account the intensity of (4.7). For comparison purposes, the broadband energy detection using the Bartlett estimator is shown in Fig. 5.17 (c), where the estimated azimuth angle using GPS info is shown in dashed red line. An empirical threshold of 80% is used for better visualization of transmission intervals, although some fishing vessels are also detected up to minute 45. Comparing Fig. 5.17 (c) with the estimated directions in Fig. 5.17 (a), it is possible to assimilate the transmitting stations with the source direction and frequency. Note that other communication signals were transmitted in different bands and modulations. In Fig. 5.17 (b), besides the directional information, a fading effect is observed within the fifty seconds of transmission. However, this figure clearly shows that there is no directional ambiguity over the communication bandwidth. This fact is important since the azimuth angle, used for beam steering, is estimated using the full bandwidth, and such estimation could be impacted when some frequency presents ambiguity.

Figure 5.18 shows the channel impulse response (CIR) of the vector sensor components for stations 3 and 6 for pressure (top), x (middle), and y (bottom) components in a normalized scale. The CIR estimation is based on a correlation estimator, where the m-sequence was used as a replica. An alignment for the Doppler is performed using the synchronization sample. In Fig. 5.18 (a), the CIR of station 3 is not aligned, and the Doppler effect due to ship drift is noticed. Since the ship is moving toward the vector sensor (see Fig. 5.13 (b)), time compression is observed. Fig. 5.18 (b) shows the CIR of station 3, where the alignment is performed using the synchronization sample. In Fig. 5.18 (c), the aligned CIR of station 6 is shown, where one can notice the CIR amplitude difference between the components.
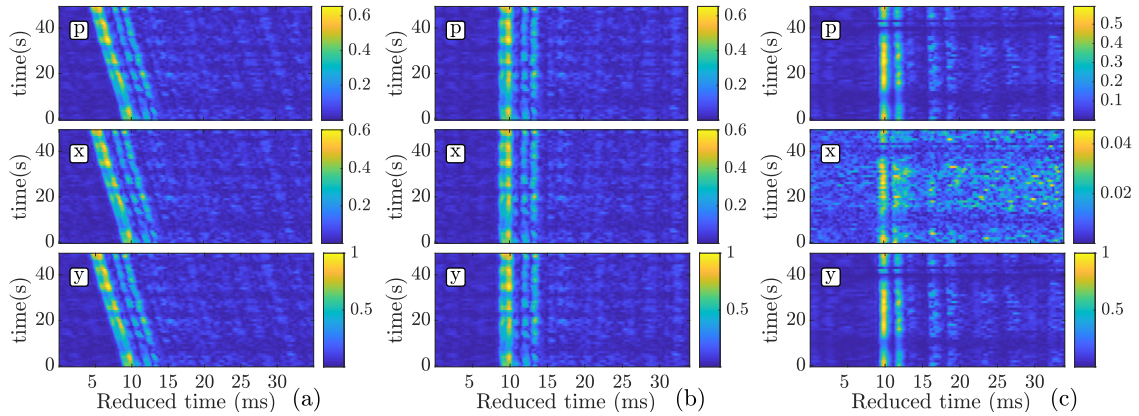
Figure 5.18: Estimated CIR for stations 3 (a)-(b) and 6 (c) for pressure (p), x, and y components (from top to bottom).

The CIR of station 6 demonstrates the attenuation of the x-axis, where the performance of methods that use such a noisy channel may be degraded.

Figure 5.19 (a) shows the estimated input SNR for pressure (p), directional components x and y, and vector sensor beam steering (vs-bs). The SNR for vs-bs is estimated using the steered output. The SNR for the passive time-reversal outputs is not shown since the combining gain is achieved after the equalizer. The SNR estimation is performed in the band from 4 to 6 kHz, and it uses a 50 s interval of the received signal and ambient noise starting
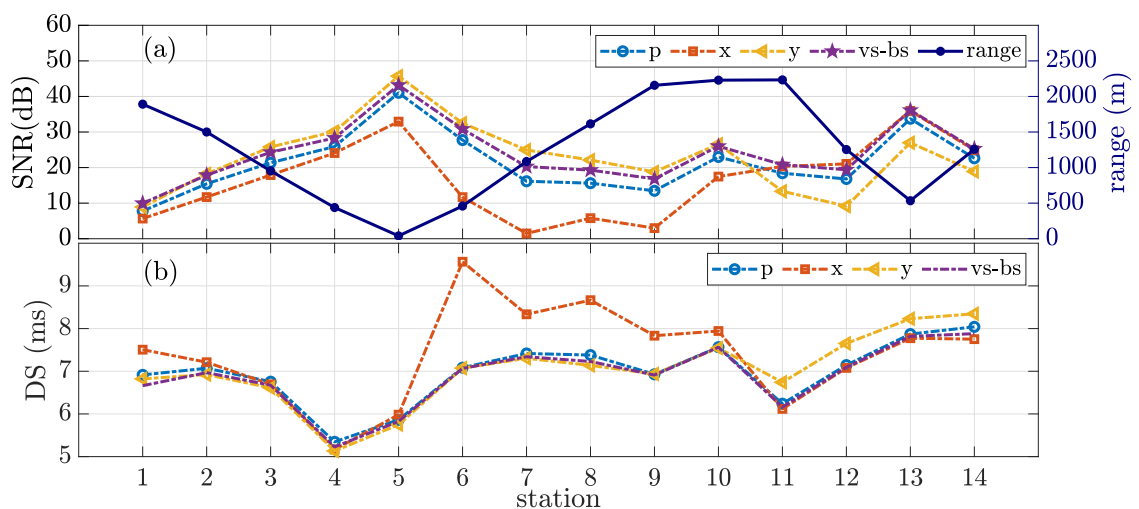
Figure 5.19: Estimated SNR (a) and RMS delay spread (b) along stations for pressure (p) and directional (x and y) components, and for vector sensor beam steering method (vs-bs).

1 min before the received signal. For convenience, the vertical right-hand side dark-blue color axis shows the vector sensor to source range. The RMS delay spread (DS) is shown in Fig. 5.19 (b), which characterizes the "severity" of the CIR, where a more extended time spread may represent a more severe channel [58]. The DS is calculated using the time-invariant CIR (power-delay profile [28]), where a -20 dB threshold is used. The DS for the passive time-reversal output is not shown since the ISI mitigation is achieved after the equalizer stage.

Figure 5.20 shows the bit error rate (BER) performance for each station. The BER results refer to the receiver structures presented in chapter 4, reduced to 2D versions since the M35 vector sensor does not measure the vertical particle velocity component. The DFE uses 34 feed-forward and 20 feedback taps for adaptive fractionally spaced equalization with oversampling factor 2. The RLS forgetting factor is set empirically to 0.997. Moreover, the integral and proportional PLL coefficients are 0.01 and 0.0001, respectively. The fifty packets are treated as independent, and the BER is estimated as a median value. The sample
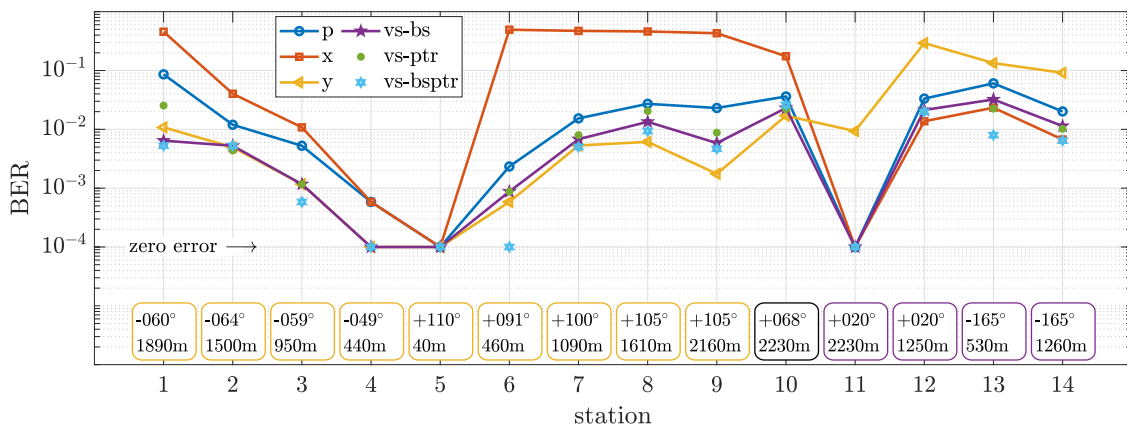
Figure 5.20: BER performance for pressure (p), directional (x and y) components, vector sensor beam steering (vs-bs), vector sensor passive time-reversal (bs), and the joint vector sensor beam steering and passive time-reversal (vs-bsptr). Bottom boxes display the source direction and range for convenience.

correlation matrix uses a full data packet interval for DoA estimation. Previous analysis has shown that the angle estimation using a shorter integration time may present fluctuation, which is not advantageous for the BER performance. In Fig. 5.20, the performance is quantified separately for the pressure, x and y components, vector sensor beam steering (vs-bs), vector sensor passive time-reversal (vs-ptr), and the joint vector sensor beam steering and passive time-reversal (vs-bsptr). Note that bottom boxes show the source direction and range, highlighting leg1 and leg2 routes. Moreover, a zero error indicator shows the lower bound to account for errors that cannot be estimated with the limited number of samples available.

Figure 5.21 shows BER in polar plots using (4.6) for discrete angles $-\pi \leq \theta_0 \leq \pi$ in y_k (ϕ_k was set to zero since the M35 is a horizontal 2D vector sensor). Performance of the pressure sensor (p) is shown for reference. From (a) to (d), the BER performance is shown for stations 3, 7, 12, and 14, respectively. These transmitting stations were chosen for analysis since they are in different geographic quadrants, where steerability can be verified. Note that the polar graphs have a logarithm inverted axis, where the highest BER value (0.5) is at the center. The similarity between BER and beam pattern can be observed using the axis in this format.
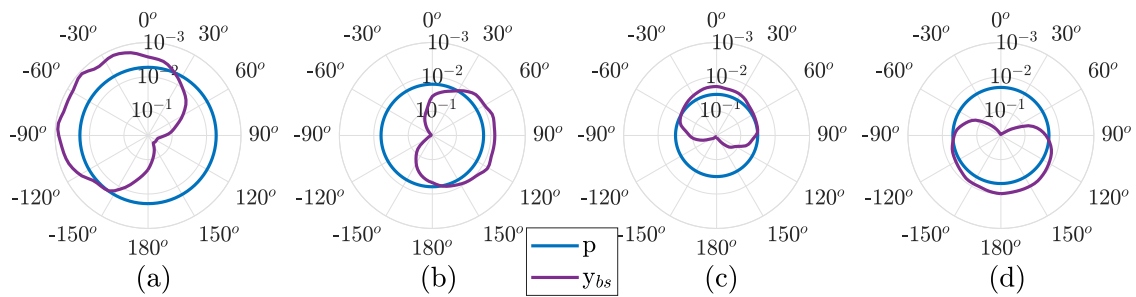
Figure 5.21: Polar BER for pressure (p) and beam steering (y_{bs}) using (4.6), for stations 3, 7, 12, and 14, from (a) to (d), respectively.

5.2.3   Analysis and discussion

5.2.3.1   Leg1 sailing route

For leg1, from stations 1 to 9, the source approaches the vector sensor from 1890 m range (station 1), passing at the closest range (40 m, station 5), and moves away up to 2160 m range (station 9). A direct relation between SNR and range is expected since the source level is kept constant throughout the experiment. The SNR curve for the pressure component of Fig. 5.19 (a) confirms this relation, where the maximum SNR was obtained at the closest range. Regarding the SNR of directional components, it is essential to consider that the source follows a predominantly West-East path. Thus, a higher SNR is expected for the y-component than for the pressure and a lower SNR for the x-component than for the pressure, which is also verified. A visual example of the SNR for each component is shown by the spectrograms of Fig. 5.16 (b) for station 7, where the power spectrum amplitude of the x-component is strongly attenuated.

In Fig. 5.19 (b), the DS values for the pressure, y-component, and beam steering (vs-bs) indicate similar channel complexity. The DS is about 7 ms long for pressure, y-component, and beam steering during leg1, except for stations 4 and 5. This result suggests that the equalizer deals with similar channel complexity, and SNR could be predominant for the achieved performance. The DS for the x-component presents similar values to pressure, y-component, and vs-bs, up to station 5. Then, the DS values for the x-component are higher than pressure/y-component/vs-bs from stations 6 to 9. These higher values are associated with imprecise CIR estimation due to x-component high attenuation, as shown in the CIR of Fig. 5.18 (c) for station 6. The DS for the beam steering presents similar values compared to pressure and y-component's DS, which is expected since these are the

predominant components in the combination.

In Fig. 5.20, the BER analysis for the pressure component shows a direct relationship between performance and range. The SNR impact is perceptible since the performance is inversely proportional to the SNR curve. However, the CIR variation among stations also affects the performance. For instance, stations 4 and 6 have similar ranges and also SNR but present different performances. In fact, the DS for these two stations indicates that the CIR of station 6 is more severe than that of station 4, which may be related to a slight change in the SSP and bathymetry. For the y-component, the SNR gain of approximately $6\,\mathrm{dB}$ ($\pm 3\,\mathrm{dB}$) relative to the pressure component reflects a BER performance improvement up to 10 times (station 1). The BER for the x-component is harshly degraded from stations 6 to 9. In these stations, the received signal is highly attenuated for the x-component since the source direction is approximately $+90°$.

The vector sensor beam steering receiver presents similar BER performance to the y-component. From stations 1 to 5, a better or equal performance than that of the y-component is noticed, and up to 10 times less error than the pressure component (station 1). However, from stations 6 to 9, the y-component SNR is higher than the vector sensor beam steering SNR, reflecting a slight outperformance. In general, the beam steering method and the y-component show a constant performance gain of about five times less errors compared to the pressure component. One can notice the relation of the steering angle to the BER by analyzing Fig. 5.21. As expected, the cardioid-like shape beam pattern reflects a BER with a similar cardioid shape, turned to the source direction. Although some distortions in the cardioid are noticed, as ISI also impacts the performance, the steerability is clear, where pointing to the source provides the lowest error.

The vs-ptr presents a slight degradation compared to vs-bs, but performance can be considered similar except for station 1, where all vector sensor components present low SNR (<10 dB). An interesting aspect regards the vs-ptr performance for station 6, where even for the noisy x-component CIR (see Fig. 5.18 (c)), the high SNR of the other components is enough to produce a similar performance to vs-bs. However, it is clear that using such a noisy component is not advantageous, and weighting the azimuth components (for this station, the x-component is practically zeroed) as in the vs-bsptr produces the best performance. The vs-bsptr provides similar or better performance than the vs-ptr and vs-bs, which supports the idea that using the source direction information is advantageous.

5.2.3.2   Changing direction sailing route

After leg1, the ship moves towards North of the vector sensor location, transmitting at station 10 and then at station 11. Stations 9, 10, and 11 are at approximately 2200 m range but onto orthogonal directions (from 105° to 20°). Thus, an inversion of the directional components' SNR is expected and verified in Fig. 5.19 (a). A BER inversion is also noticed between the x and y-components in Fig. 5.20. In fact, superior performance is verified at station 11, which can be partially explained by the small DS for this station.

5.2.3.3   Leg2 sailing route

During leg2, the ship approaches the vector sensor from 2230 m range (station 11), passes through the vector sensor, and moves away up to 1260 m range (station 14). The BER performance reflects the North-South path, where the x-component shows the highest SNR. From stations 12 to 14, the BER for both vs-bs and vs-ptr varies from 1% to 3%, whereas for the vs-bsptr from 0.6% to 2%. A substantial fading effect is verified in these stations,

and the DS increased from 6 to 8 ms, indicating more severe channels.

5.2.3.4 Summary of the receiver structures' performance

The BER analysis shown in Fig. 5.20 provides a relation between communication performance, direction, and range. One aspect we noticed from the results was that the beam steering has provided a noticeable gain for all the tested transmission stations. Even for different CIR along the stations, we are tempted to say that the performance gain is constant, which it is not. Such results empirically indicate that the receiver with the beam steering could present a predictable performance, suggesting that such relative performance (between a vector sensor and a pressure sensor) could be found to persist, even under different experimental conditions. The vs-ptr provides comparable performance to vs-bs, except for station 1. However, the slightly degraded performance can be associated to noisy components, which also results in inaccurate CIR estimations. The vs-bsptr presents the best performance, where weighting the components according to the source direction suggests to be advantageous.

5.2.4 JANUS: results and analysis

In the EMSO'21 experiment, the frequency-hopped JANUS modulation, a well-known robust communication option, was also transmitted to investigate the gain of combining vector sensor components [87]. Although the main purpose of this work is to test coherent modulation schemes using the receiver structures of chapter 4, the use of JANUS modulation signals is also interesting since the UWAC community widely uses JANUS. Moreover, it is expected that we can compare, qualitatively, results of JANUS and the results presented for coherent modulation. Advantages of JANUS are: standardization, interoperability, and

its easy employment with open-source codes [22, 23, 88, 89]. The use of a vector sensor for JANUS has the objective of allowing a faster bit rate by improving SNR [89]. However, one can think of a scenarios with multiple sources, where the spatial filter may also be useful for reducing interference. The objective here is not focused on the frequency-hopped modulation itself and its particularities, which readers can find technical information in [23, 88], but to quantify the channel combining gain for JANUS performance. Since we use embedded JANUS synchronization process, here we will only quantify the beam steering method. Two analyses quantify the communication performance: BER varying the azimuth angle of (4.6); and BER using individual vector sensor channels or beam steering for six stations. The BER is quantified before the JANUS interleaved stage, and the transmitted signals are modulated in center frequencies (f_c) of 5 and 10 kHz, and include the cargo sentence "acoustic vector sensors". Different from the JANUS description manual [88], which states about using a bandwidth of $W \approx f_c/3$, here, the bandwidth is fixed in 2 kHz. Such configuration was proposed taking into account two aspects: we have opted to use bands with approximately constant amplitudes, based on the Lubell-916C sound source transmission response; we expect to compare the JANUS with coherence modulation schemes, where the adopted BPSK signals were defined with these frequency bands. Due to these aspects, we were not able to test the standardized JANUS frequency (11520 Hz). However, considering a fixed beam steering gain over the frequency range, we expect that the performance in the standardized frequency (compared to the pressure channel) can be similar to that presented.

Figure 5.22 shows the BER in a polar graphic from station 3, 7, 9, 10, 11, and 14, from (a) to (f), for the first analyzed band ($f_c = 5$ kHz). Note that, as in Fig. 5.21, the figure axis is inverted, where the error grows toward the center, which is normalized at 0.5. The BER
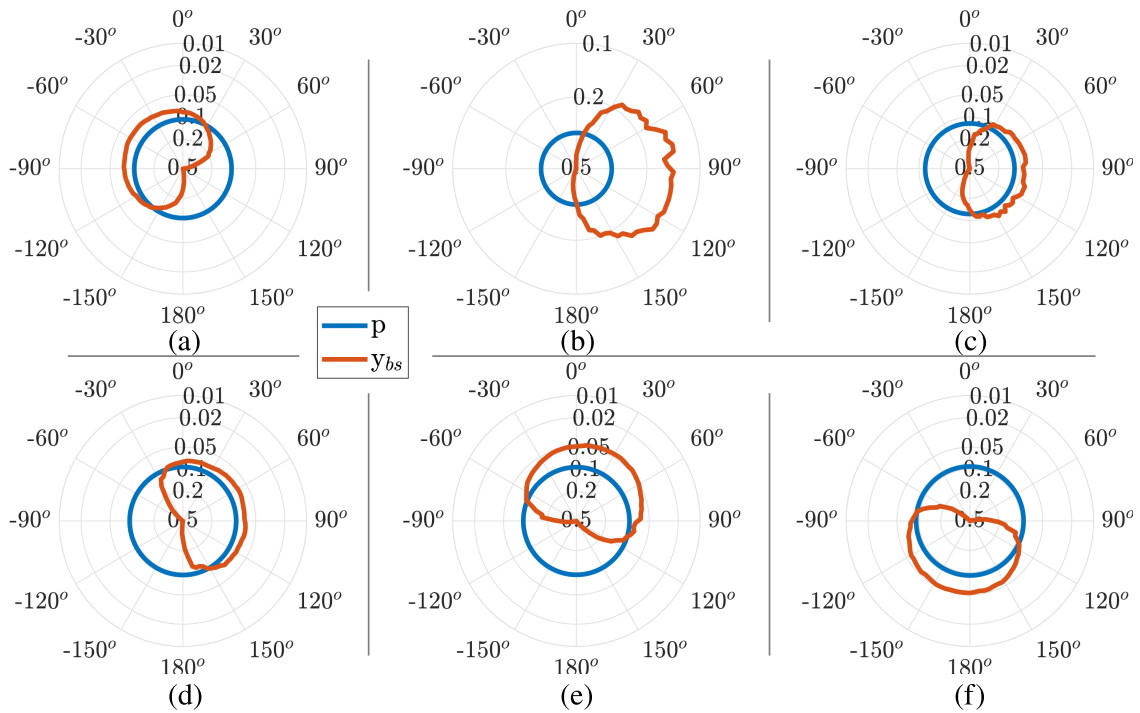
Figure 5.22: Polar BER for pressure (p) and beam steering (y_{bs}) using (4.6), for stations 3, 7, 9, 10, 11, and 14, from (a) to (f), respectively.

is calculated by combining the vector sensor channels in the beam steering (y_{bs}), and it can be compared to the pressure channel. The figure is quite illustrative, combining directional information with BER performance. One can notice that a similar cardioid-like pattern is found but with some fluctuation. These are expected results since we are measuring the error that is also impacted by multipath. In general, for the beam steering, the minimum error is found in the source direction and is reduced by around 5% compared to the pressure channel. Comparing the BER patterns with those found for coherent modulation in Fig. 5.21, a similar cardioid-like pattern is verified.

Figure 5.23 shows the BER along the stations for $f_c = 5\,\text{kHz}$ (a) and $f_c = 10\,\text{kHz}$ (b). The BER was quantified for the pressure-sensor, individual particle velocity channels, and vector sensor beam steering (vs-bs). The overall BER performance for $f_c = 10\,\text{kHz}$ is better than for $f_c = 5\,\text{kHz}$. Such result can be assigned to higher SNR, where the ambient noise
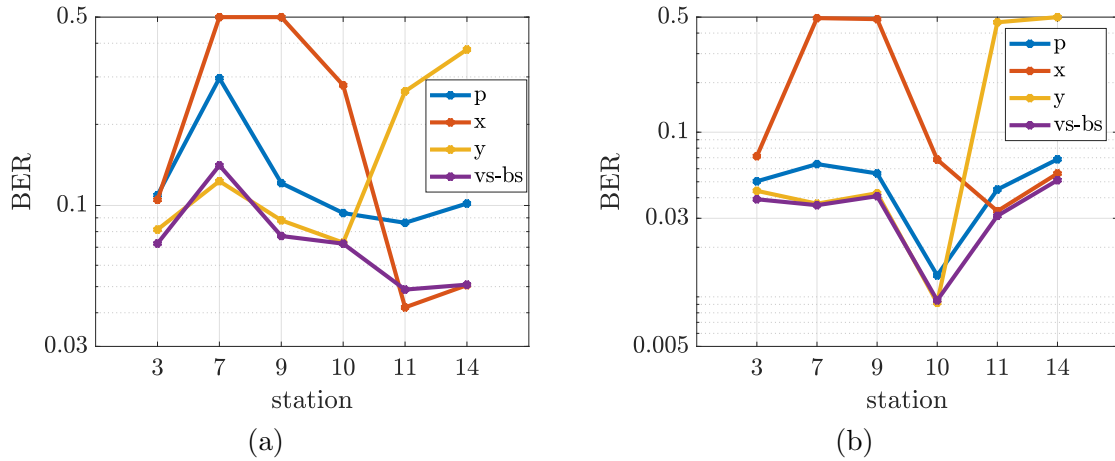
Figure 5.23: BER along stations for pressure, individual particle velocity channels, and vector sensor-beam steering (vs-bs), for $f_c = 5\,\text{kHz}$ (a) and $f_c = 10\,\text{kHz}$ (b).

is observed to be higher at lower frequencies ($< 5\,\text{kHz}$) and the sound source transmission response has a higher amplitude in the frequency band centered at $10\,\text{kHz}$. The beam steering approach resulted in a concise error reduction along the stations compared to the pressure, demonstrating its advantage. Transmissions at stations 7 and 9 were predominantly towards the y-component, where the x-component SNR is decreased, resulting in the highest error. Among stations 9, 10, and 11, the transmissions were performed approximately at a radius of $2.2\,\text{km}$ and varied the direction by $90°$. As expected, the performance of the individual directional components changes, whereas the beam steering keeps the performance by combining the channels with the source direction. Another noticed aspect is that the outperformance of the beam steering is more perceptible in the lowest band. Since the overall SNR is lower at $5\,\text{kHz}$, the SNR gain of the beam steering produces a more significant impact on performance.

Chapter 6

Conclusions

Synopsis: *This chapter summarizes analyzes, understandings, and findings within the framework of this research work. Section 6.1 shows the work overview with concluding remarks based on previous chapters. Contributions are presented in section 6.2, whereas perspectives for future investigations are highlighted in section 6.3.*

6.1 Concluding remarks

The present work investigated the usage of vector sensors for underwater acoustic communications. Motivated by its compactness in a single collocated device and its directional information, the rich literature on vector sensors has shown diverse applications that make use of such a device. We can observe that small, light, and low-power acoustic devices are in a demand that surges with the increased usage of mobile unmanned underwater platforms, where UWAC is particularly challenging. In this context, a vector sensor device fits the current technological tendency. Although some applications, such as sonar systems, have used vector sensors over the last three decades, its usage for underwater communications is relatively new. Considering that the two main issues of UWAC are related to SNR and/or ISI, the general question is how to take advantage of the directional components of vec-

tor sensors to enhance UWAC performance. Thus, this work has sought answers based on understanding particle velocity components, using simulations and experimental data, and testing receiver structures designed for vector sensors.

Important aspects were introduced regarding particle velocity measurements, where the vector sensor conversion technology cannot obscure the physics. We have seen that pressure-gradient vector sensors provide an estimation of the particle velocity by using pairs of hydrophones. Although the difference-operation limits the dynamic range, they are less sensitive to non-acoustic interference, such as flow noise and mechanical vibration. Thus, this type of vector sensor may preferably be employed on fixed positions or onboard underwater vehicles, considering that flow noise is greater for a fixed sensor than a drifting sensor, and also on platforms moving through the water. Using other conversion technology, inertial sensors, usually referred to as accelerometer-based vector sensors, have wide and constant bandwidth, where a directional gain can be achieved even for very low frequency (under 300 Hz). Their main issue regards the non-acoustic interference since they respond to movement. Thus, this type of vector sensor may be more appropriately employed in drifting buoys, such as sonobuoys, or in fixed structures that keep the sensor body in free mode. Such aspects regarding the types of vector sensors are followed by the analysis of vector sensors' directional characteristics, where beam patterns for both a single vector sensor and a vector sensor array are quantified.

Complementary to the directivity analysis, a communication system is briefly reviewed to put in context the challenges of UWAC channels. Then, a statistical approach for modeling the vector sensor components is derived, showing channel correlation for a shallow-water case study. Such theoretical analysis of correlation among pressure and particle velocity

channels supports the concepts of the tested receiver structures. These structures are based on standard structures, which are adapted to take advantage of diversity and/or beamforming methods considering the directional components.

The first analyzed receiver structure is based on passive time-reversal. This standard structure is used as a reference, and channel diversity gain is expected if channel correlation is low. A second structure is based on beamforming, where the idea is to explore high correlated vector sensor components. For this latter structure, it is proposed three steered outputs when a 3D vector sensor is employed, which, in theory, combines correlated components. The last structure joins the beam steering with passive time-reversal, where the azimuth components of the PTR are weighted according to the source direction angle. To the best of our knowledge, this is the first work that uses a vector sensor joining beam steering and passive time-reversal. Although the concepts of the two first methods were already reported in the literature, the presented structures are different. In general, such structures differ from standard communication structures in the following aspects: noise normalization, which has demonstrated an advantage for balancing vector sensor channels when using experimental data; beam steering, where directions are properly chosen to improve the coherence of vertical and horizontal component combinations; and the passive time-reversal, which has horizontal components weighted according to the joint direction information, attenuating possible noisy components, and the channels combining is performed after the first stage of the equalizer, enhancing coherence combination.

Those receiver structures were tested in two experiments with two different types of vector sensors. In the first experiment (MakaiEx), an accelerometer-based vector sensor array is used in free movement with a fixed bottom sound source. Prior to analyzing the

experiment data, we worked with simulations of the Makai experiment site to provide an initial insight of the various receivers' performance. Results have indicated the advantage of the beam steering at shorter ranges and the PTR at longer ranges, which was also verified with field data acquired during the MakaiEx. For real data, the joint method has reduced the error by around ten times compared to separate approaches, using a single vector sensor for the longer range. It has also been shown that a single vector sensor (or VSA) outperforms a pressure-only array having an adequate aperture for beamforming. However, here, it is shown that the joint method can achieve further performance enhancement. In the second experiment (EMSO), a 2D pressure-gradient vector sensor is deployed in a tripod moored to the ocean seabed and used as a receiver for a source deployed from a ship. Communication performance was quantified for several ranges and directions using the tested receiver structures and also individual vector sensor components. Moreover, the EMSO field experiment has played a crucial role in allowing us to test and relate the directional components by analyzing almost 360° of the vector sensor steering ability. Such structures using the vector sensors components have shown performance from 2 to 10 times higher than that using only the pressure component. The beam steering method has mitigated ambiguities from the opposite direction and showed robustness for transmissions from different geographic quadrants. Moreover, a consistent performance gain was verified for the tested transmission stations, even for different CIR along the stations. Such a result indicates that the receiver with beam steering could provide predictably improved performance using a vector sensor, even across different experimental conditions. An example of applicability of the beam steering was also tested for JANUS modulated signals, which has shown that JANUS performance can be enhanced. The joint method has presented the

best performance for all transmitting stations, which reinforces that weighting the vector sensor components for PTR is advantageous.

In summary, taking into account the theoretical analysis, simulation, and experimental results, the present work has shown evidence to support that:

- Vector sensor components can be explored either by diversity or beamforming approaches, although exploring both methods together seems to be the best option to reduce communication error. For the tested acoustic scenarios, vector sensor channel diversity is clearer between pressure/horizontal components and the vertical component for longer source-receiver ranges (say, more than 300 m).

- The passive time-reversal takes its best advantage of diversity when vector sensor channels are uncorrelated, or at least, it may be reduced to beamforming when channels are correlated. However, for communications, if inaccuracy in channel impulse response estimation starts to degrade performance, beamforming may be advantageous.

- The use of a single vector sensor in such tested structures may provide similar performance to a small pressure-only array. Certainly, there is no guarantee of the vector sensor outperformance since the length, spacing, and channel correlation of the pressure-only array are factors that influence the performance. Although such a positive statement has already been reported, we showed that an adapted design taking into account the directional characteristics of the vector sensor components further improves the performance.

- It was shown that channel diversity of a single point-like vector sensor may not be properly-interpreted as spatial diversity, as stated by some authors [59, 74]. We saw

that vector sensor channel diversity is related to the orthogonality of the particle velocity components, which comes from its inherent directionality.

- The use of vector sensor components forming steered outputs has been closely investigated, where using azimuth DoA information is advantageous. The DoA was used both in the beam steering method and in the joint beam steering and passive time-reversal. Whereas the performance of the former was directly related to the steerability, the latter, weighted azimuth components, provided more influence of the components in the source direction. Two aspects were noted: (1) In the MakaiEx dataset with the 3D vector sensors, the use of elevation angle is not advantageous since the error is not mitigated and DoA may not be accurate; (2) In the EMSO dataset with the 2D vector sensor, pointing to source direction increases SNR and reduces the error.

One can note that the above statements are answers for some of the motivation questions presented in section 1.2.

6.2   Contributions

In summary, the contributions of this work are:

1. Strongly support the proper use of vector sensor directional information, where theoretical analysis of correlation among acoustic pressure and particle velocity channels helps to understand how to advantageously combine vector sensor components on each tested structure;

2. Propose a joint method structure designed for vector sensors and compare it to standard structures. It was possible to see that structures designed for vector sensors

outperform a small pressure-only array or standard ones.

3. Shows a broad comparison, using vector sensors individually and/or combining multiple vector sensors. Two vector sensor types were used in two different experiment scenarios, where structure receivers were carefully investigated, exploring diversity or/and beamforming approaches.

These contributions are the results of studies progressively presented to the scientific community in the following publications [73, 78, 79, 87, 90, 91]:

1. F. A. Bozzi and S. M. Jesus, "Vector sensor beam steering for underwater acoustic communications," in *Proc. of Meetings on Acoustics*, vol. 42. ASA, 2020, p. 070002.

2. F. A. Bozzi and S. M. Jesus, "Acoustic vector sensor underwater communications in the makai experiment," in *Proc. of Meetings on Acoustics, 6th UACE*. ASA, Jul. 2021, p. 070029.

3. F. A. Bozzi and S. M. Jesus, "Vector hydrophone passive time reversal for underwater acoustic communications," in *OCEANS 2022*. Chennai, India: IEEE, Feb. 2022, pp. 1–5.

4. F. A. Bozzi and S. M. Jesus, "Joint Vector Sensor Beam Steering and Passive Time Reversal for Underwater Acoustic Communications," in *IEEE Access*. DOI 0.1109/ACCESS.2022.3183348.

5. F. A. Bozzi, F. Zabel, and S. M. Jesus, "Frequency-dependent underwater acoustic communications performance using a pressure-gradient vector sensor," accepted in *Int. Conf. on Acoustics, Gyeongju (South Korea)*, vol. 42. ICA, 2022.

6. F. Bozzi and S.M. Jesus, "Experimental Demonstration of a Single Acoustic Vector Sensor for JANUS Performance Enhancement," accepted in *6 th Underwater Communications and Networking Conf. (UComms), Lerici (Italy)*, September.

6.3   Future work

Besides the findings presented in the present research, we can highlight some possible investigations, which are out of the scope of this work, but may also be interesting in further studies:

- Optimized channel selection: the receiver structures tested in this work are expected to work as practical tools for real-time applications in size-restricted platforms. We have seen that superior performance is achieved by combining vector sensors in a vector sensor array. However, it comes with computational expenses as the number of channels increases in the multichannel equalizer. Thus, future investigations could be performed by optimizing the channel selection instead of using all VSA channels.

- Multiusers adaptation using artificial intelligence (AI) approaches: in the context of multi-user networks, multiple steered outputs could be required, and it would be, most likely, preferable to mitigate the interference than to point to the source direction. In this topic, the use of AI optimization could be interesting either for sources detection and tracking, or for network management including the spatial filtering capability of vector sensors.

- Channel sounding: an effective strategy to validate communication receiver structures uses a benchmark with realistic underwater channels. A possible and current approach

is the replay-based method using channel soundings [92]. Although the library of underwater acoustic channel is growing, the CIR are only for pressure sensors. Thus, data collection for CIR estimation that includes particle velocity channels would also be a valuable contribution.

- Active vector sensors: this study's scope uses vector sensors as a receiver for UWAC. However, the active version is also a possibility. A small number of studies cover this topic, where investigations may add great value in this research field [93, 94].

Bibliography

[1] H. Medwin and C. S. Clay, *Fundamentals of acoustical oceanography*, ser. Applications of modern acoustics. Boston: Academic Press, 1998.

[2] F. B. Jensen, W. A. Kuperman, M. B. Porter, and H. Schmidt, *Computational Ocean Acoustics*. New York, NY: Springer New York, 2011.

[3] J. G. Proakis and M. Salehi, *Digital communications*, 5th ed. Boston: McGraw-Hill, 2008.

[4] M. Chitre, S. Shahabudeen, and M. Stojanovic, "Underwater acoustic communications and networking: Recent advances and future challenges," *Mar Technol Soc J*, vol. 42, no. 1, pp. 103–116, Mar. 2008.

[5] S. Sendra, J. Lloret, J. M. Jimenez, and L. Parra, "Underwater acoustic modems," *IEEE Sensors J.*, vol. 16, no. 11, pp. 4063–4071, Jun. 2016.

[6] A. Baggeroer, "Acoustic telemetry - an overview," *IEEE J. Oceanic Eng.*, vol. 9, no. 4, pp. 229–235, Oct. 1984.

[7] J. Catipovic, "Performance limitations in underwater acoustic telemetry," *IEEE J. Oceanic Eng.*, vol. 15, no. 3, pp. 205–216, Jul. 1990.

[8] J. Catipovic and L. Freitag, "Spatial diversity processing for underwater acoustic teleme-try," *IEEE J. Oceanic Eng.*, vol. 16, no. 1, pp. 86–97, Jan./1991.

[9] M. Stojanovic, J. Catipovic, and J. G. Proakis, "Adaptive multichannel combining and equalization for underwater acoustic communications," *J. Acoust. Soc. Am.*, vol. 94, no. 3, pp. 1621–1631, Sep. 1993.

[10] M. Stojanovic, J. Catipovic, and J. Proakis, "Phase-coherent digital communications for underwater acoustic channels," *IEEE J. Oceanic Eng.*, vol. 19, no. 1, pp. 100–111, Jan./1994.

[11] T. Yang and A. Al-Kurd, "Performance limitations of joint adaptive channel equalizer and phase locking loop in random oceans: initial test with data," in *OCEANS 2000 MTS/IEEE Conference and Exhibition. Conference Proceedings (Cat. No.00CH37158)*, vol. 2.   Providence, RI, USA: IEEE, 2000, pp. 803–808.

[12] T. Yang, "Differences between passive-phase conjugation and decision-feedback equal-izer for underwater acoustic communications," *IEEE J. Oceanic Eng.*, vol. 29, no. 2, pp. 472–487, Apr. 2004.

[13] T. C. Yang, "A study of spatial processing gain in underwater acoustic communica-tions," *IEEE J. Oceanic Eng.*, vol. 32, no. 3, pp. 689–709, Jul. 2007.

[14] A. Song, M. Badiey, H. C. Song, W. S. Hodgkiss, and M. B. Porter, "Impact of ocean variability on coherent underwater acoustic communications during the kauai experiment (kauaiex)," *The Journal of the Acoustical Society of America*, vol. 123, no. 2, pp. 856–865, Feb. 2008.

[15] J. Flynn, J. Ritcey, D. Rouseff, and W. Fox, "Multichannel equalization by decision-directed passive phase conjugation: experimental results," *IEEE J. Oceanic Eng.*, vol. 29, no. 3, pp. 824–836, Jul. 2004.

[16] J. Gomes, A. Silva, and S. Jesus, "Joint passive time reversal and multichannel equalization for underwater communications," in *OCEANS 2006*. Boston, MA: IEEE, Sep. 2006, pp. 1–6.

[17] ——, "Adaptive spatial combining for passive time-reversed communications," *The Journal of the Acoustical Society of America*, vol. 124, no. 2, pp. 1038–1053, Aug. 2008.

[18] W. A. Kuperman, W. S. Hodgkiss, H. C. Song, T. Akal, C. Ferla, and D. R. Jackson, "Phase conjugation in the ocean: Experimental demonstration of an acoustic time-reversal mirror," *The Journal of the Acoustical Society of America*, vol. 103, no. 1, pp. 25–40, Jan. 1998.

[19] S. Zhou and Z. Wang, *OFDM for underwater acoustic communications*. Chichester, West Sussex, United Kingdom: Wiley, 2014.

[20] Z. Liu and T. C. Yang, "On overhead reduction in time-reversed ofdm underwater acoustic communications," *IEEE J. Oceanic Eng.*, vol. 39, no. 4, pp. 788–800, Oct. 2014.

[21] G. Qiao, Z. Babar, L. Ma, S. Liu, and J. Wu, "Mimo-ofdm underwater acoustic communication systems—a review," *Physical Communication*, vol. 23, pp. 56–64, Jun. 2017.

[22] J. Potter, J. Alves, D. Green, G. Zappa, I. Nissen, and K. McCoy, "The janus underwater communications standard," in *2014 Underwater Communications and Networking (UComms).*   Sestri Levante, Italy: IEEE, Sep. 2014, pp. 1–4.

[23] K. McCoy, V. Djapic, and M. Ouimet, "Janus: Lingua franca," in *OCEANS 2016 MTS/IEEE Monterey.*   Monterey, CA, USA: IEEE, Sep. 2016, pp. 1–4.

[24] G. Zappa, *JANUS Tool Kit 3.0.1*, Online: http://www.januswiki.com, Mar. 2013.

[25] A. Song, M. Stojanovic, and M. Chitre, "Editorial underwater acoustic communications: Where we stand and what is next?" *IEEE J. Oceanic Eng.*, vol. 44, no. 1, pp. 1–6, Jan. 2019.

[26] D. Wübben, A. Könsgen, A. Udugama, A. Dekorsy, and A. Förster, "Challenges and opportunities in communications for autonomous underwater vehicles," in *AI Technology for Underwater Robots*, F. Kirchner, S. Straube, D. Kühn, and N. Hoyer, Eds.   Cham: Springer International Publishing, 2020, vol. 96, pp. 83–93.

[27] A. Hamilton, S. Holdcroft, D. Fenucci, P. Mitchell, N. Morozs, A. Munafò, and J. Sitbon, "Adaptable underwater networks: The relation between autonomy and communications," *Remote Sensing*, vol. 12, no. 20, p. 3290, Oct. 2020.

[28] P. A. van Walree, "Channel sounding for acoustic communications: Techniques and shallow-water examples," Norwegian Defence Research Establishment (FFI), Tech. Rep. 2011/00007, Apr. 2011.

[29] P. van Walree, R. Otnes, and T. Jenserud, "Watermark: A realistic benchmark for

underwater acoustic modems," in *2016 IEEE Third Underwater Communications and Networking Conference (UComms)*. Lerici, Italy: IEEE, Aug. 2016, pp. 1–4.

[30] H. F. Olson, "Mass controlled electrodynamic microphones: The ribbon microphone," *The Journal of the Acoustical Society of America*, vol. 3, no. 1A, pp. 9–9, Jul. 1931.

[31] C. B. Leslie, J. M. Kendall, and J. L. Jones, "Hydrophone for measuring particle velocity," *The Journal of the Acoustical Society of America*, vol. 28, no. 4, pp. 711–715, Jul. 1956.

[32] B. Cray, E. Roy C, G. D'Spain, T. Gabrielson, and M. Silvia, "Workshop on directional acoustic sensors," Naval Undersea Warfare Center Division and Office of Naval Research, Newport, Rhode Island, Proceedings of the Workshop on Directional Acoustic Sensors, Apr. 2001.

[33] J. Nickles, G. Edmonds, R. Harriss, F. Fisher, W. Hodgkiss, J. Giles, and G. D'Spain, "A vertical array of directional acoustic sensors," in *OCEANS 92 Mastering the Oceans Through Technology*, vol. 1. Newport, RI: IEEE, 1992, pp. 340–345.

[34] A. Nehorai and E. Paldi, "Acoustic vector-sensor array processing," *IEEE Trans. Signal Process.*, vol. 42, no. 9, pp. 2481–2491, Sept./1994.

[35] M. Hawkes and A. Nehorai, "Surface-mounted acoustic vector-sensor array processing," in *1996 IEEE International Conference on Acoustics, Speech, and Signal Processing Conference Proceedings*, vol. 6. Atlanta, GA, USA: IEEE, 1996, pp. 3169–3172.

[36] ——, "Effects of sensor placement on acoustic vector-sensor array performance," *IEEE J. Oceanic Eng.*, vol. 24, no. 1, pp. 33–40, Jan./1999.

[37] S. M. Jesus, F. C. Xavier, R. P. Vio, J. Osowsky, M. V. S. Simões, and E. B. F. Netto, "Particle motion measurements near a rocky shore off cabo frio island," *The Journal of the Acoustical Society of America*, vol. 147, no. 6, pp. 4009–4019, Jun. 2020.

[38] L. E. Kinsler, Ed., *Fundamentals of acoustics*, 4th ed.   New York: Wiley, 2000.

[39] B. Cray, A. Nuttall, and N. U. W. C. N. D. RI., "A comparison of vector-sensing and scalar-sensing linear arrays," Defense Technical Information Center, Tech. Rep., 1997.

[40] P. Felisberto, P. Santos, and S. M. Jesus, "Acoustic pressure and particle velocity for spatial filtering of bottom arrivals," *IEEE J. Oceanic Eng.*, vol. 44, no. 1, pp. 179–192, Jan. 2019.

[41] K. B. Smith and A. V. van Leijen, "Steering vector sensor array elements with linear cardioids and nonlinear hippioids," *J. Acoust. Soc. Am.*, vol. 122, no. 1, pp. 370–377, Jul. 2007.

[42] D. Levin, E. A. P. Habets, and S. Gannot, "Maximum likelihood estimation of direction of arrival using an acoustic vector-sensor," *J. Acoust. Soc. Am.*, vol. 131, no. 2, pp. 1240–1248, Feb. 2012.

[43] H. Lai, K. Bell, and H. Cox, "Doa estimation using vector sensor arrays," in *2008 42nd Asilomar Conference on Signals, Systems and Computers*.   Pacific Grove, CA, USA: IEEE, Oct. 2008, pp. 293–297.

[44] S. S. Du, K. T. Wong, Y. Song, C. J. Nnonyelu, and Y. I. Wu, "Higher-order figure-8 microphones/hydrophones collocated as a perpendicular triad—their "spatial-matched-

filter" beam steering," *The Journal of the Acoustical Society of America*, vol. 151, no. 2, pp. 1158–1170, Feb. 2022.

[45] H. Cao, W. Wang, L. Su, H. Ni, P. Gerstoft, Q. Ren, and L. Ma, "Deep transfer learning for underwater direction of arrival using one vector sensor," *J. Acoust. Soc. Am.*, vol. 149, no. 3, pp. 1699–1711, Mar. 2021.

[46] K. Wong and M. Zoltowski, "Orthogonal velocity-hydrophone esprit for sonar source localization," in *OCEANS 96 MTS/IEEE Conference Proceedings. The Coastal Ocean - Prospects for the 21st Century*, vol. 3.   Fort Lauderdale, FL, USA: IEEE, 1996, pp. 1307–1312.

[47] M. Hawkes and A. Nehorai, "Acoustic vector-sensor beamforming and capon direction estimation," *IEEE Trans. Signal Process.*, vol. 46, no. 9, pp. 2291–2304, Sept./1998.

[48] P. Santos, O. C. Rodríguez, P. Felisberto, and S. M. Jesus, "Seabed geoacoustic characterization with a vector sensor array," *J. Acoust. Soc. Am.*, vol. 128, no. 5, pp. 2652–2663, Nov. 2010.

[49] S. M. Jesus and P. Felisberto, "Dual accelerometer vector sensor," Portugal Patent 2018/178 913, Mar., 2017.

[50] P. J. M. Santos, P. Felisberto, F. Zabel, S. Jesus, and L. Sebastião, "Dual accelerometer vector sensor mounted on an autonomous underwater vehicle (auv) - experimental results," in *173rd Meeting of Acoustical Society of America and 8th Forum Acusticum*, Boston, Massachusetts, 2017, p. 055011.

[51] S. L. Nedelec, J. Campbell, A. N. Radford, S. D. Simpson, and N. D. Merchant, "Particle

motion: the missing link in underwater acoustic ecology," *Methods Ecol Evol*, vol. 7, no. 7, pp. 836–842, Jul. 2016.

[52] A. M. Thode, T. Sakai, J. Michalec, S. Rankin, M. S. Soldevilla, B. Martin, and K. H. Kim, "Displaying bioacoustic directional information from sonobuoys using "azi-grams"," *J. Acoust. Soc. Am.*, vol. 146, no. 1, pp. 95–102, Jul. 2019.

[53] A. Abdi, H. Guo, and P. Sutthiwan, "A new vector sensor receiver for underwater acoustic communication," in *OCEANS 2007*. Vancouver, BC: IEEE, Sep. 2007, pp. 1–10.

[54] A. Abdi and Huaihai Guo, "Signal correlation modeling in acoustic vector sensor arrays," *IEEE Trans. Signal Process.*, vol. 57, no. 3, pp. 892–903, Mar. 2009.

[55] H. Guo, A. Abdi, A. Song, and M. Badiey, "Correlations in underwater acoustic particle velocity and pressure channels," in *2009 43rd Annual Conference on Information Sciences and Systems*. Baltimore, MD, USA: IEEE, Mar. 2009, pp. 913–918.

[56] F. Fauziya, B. Lall, and M. Agrawal, "Impact of vector sensor on underwater acoustic communications system," *IET Radar, Sonar & Navigation*, vol. 12, no. 12, pp. 1500–1508, Dec. 2018.

[57] M. Hawkes and A. Nehorai, "Acoustic vector-sensor correlations in ambient noise," *IEEE J. Oceanic Eng.*, vol. 26, no. 3, pp. 337–347, Jul. 2001.

[58] A. Song, A. Abdi, M. Badiey, and P. Hursky, "Experimental demonstration of underwater acoustic communication by vector sensors," *IEEE J. Oceanic Eng.*, vol. 36, no. 3, pp. 454–461, Jul. 2011.

[59] L.-x. Guo, X. Han, J.-w. Yin, and X.-s. Yu, "Underwater acoustic communication by a single-vector sensor: performance comparison using three different algorithms," *Shock and Vibration*, vol. 2018, pp. 1–8, Nov. 2018.

[60] X. Han, J. Yin, Y. Tian, and X. Sheng, "Underwater acoustic communication to an unmanned underwater vehicle with a compact vector sensor array," *Ocean Engineering*, vol. 184, pp. 85–90, Jul. 2019.

[61] M. Chitre, "A high-frequency warm shallow water acoustic communications channel model and measurements," *J. Acoust. Soc. Am.*, vol. 122, no. 5, p. 2580, 2007.

[62] D. S. Terracciano, "Towards new capabilities for passive acoustics in underwater surveillance and signature measurement applications: the autonomous way." Ph.D. dissertation, University of Pisa, Italy, Jun. 2021.

[63] G. D'Spain, J. Luby, G. Wilson, and R. Gramann, "Vector sensors and vector sensor line arrays: comments on optimal array gain and detection," *J. Acoust. Soc. Am.*, vol. 120, p. 171, Jul. 2006.

[64] T. Gabrielson, "Design problems and limitations in vector sensors," Naval Undersea Warfare Center Division and Office of Naval Research, Newport, Rhode Island, Proceedings of the Workshop on Directional Acoustic Sensors, Apr. 2001.

[65] B. A. Cray and A. H. Nuttall, "Directivity factors for linear arrays of velocity sensors," *The Journal of the Acoustical Society of America*, vol. 110, no. 1, pp. 324–331, Jul. 2001.

[66] C. H. Sherman and J. L. Butler, *Transducers and Arrays for Underwater Sound.* New York, NY: Springer New York, 2007.

[67] G. D'Spain, W. Hodgkiss, G. Edmonds, J. Nickles, F. Fisher, and R. Harriss, "Initial analysis of the data from the vertical difar array," in *OCEANS 92 Proceedings@m_Mastering the Oceans Through Technology*, vol. 1. Newport, RI: IEEE, 1992, pp. 346–351.

[68] H. Van Trees, *Optimum array processing: Part IV of detection, estimation, and modulation theory*, ser. Detection, estimation, and modulation theory. Wiley, 2004.

[69] W. Kuperman and P. Roux, "Underwater acoustics," in *Springer Handbook of Acoustics*, T. D. Rossing, Ed. New York, NY: Springer New York, 2007, pp. 149–204.

[70] W. S. Burdic, *Underwater acoustic system analysis*, 2nd ed., ser. Prentice Hall signal processing series. Englewood Cliffs, N.J: Prentice Hall, 1991.

[71] F. Hlawatsch and G. Matz, *Wireless communications over rapidly time-varying channels*. Elsevier Science, 2011.

[72] J. Cao, J. Liu, J. Wang, and X. Lai, "Acoustic vector sensor: reviews and future perspectives," *IET signal process.*, vol. 11, no. 1, pp. 1–9, Feb. 2017.

[73] F. A. Bozzi and S. M. Jesus, "Acoustic vector sensor underwater communications in the makai experiment," in *Proceedings of Meetings on Acoustics, 6th UACE*. Virtual Meeting: ASA, Jul. 2021, p. 070029.

[74] A. Song, M. Badiey, P. Hursky, and A. Abdi, "Time reversal receivers for underwater

acoustic communication using vector sensors," in *OCEANS 2008*. Quebec City, QC, Canada: IEEE, Sep. 2008, pp. 1–10.

[75] B. Sharif, J. Neasham, O. Hinton, and A. Adams, "A computationally efficient doppler compensation system for underwater acoustic communications," *IEEE J. Oceanic Eng.*, vol. 25, no. 1, pp. 52–61, Jan. 2000.

[76] G. Zhang and H. Dong, "Joint passive-phase conjugation with adaptive multichannel combining for coherent underwater acoustic communications," *Applied Acoustics*, vol. 73, no. 4, pp. 433–439, Apr. 2012.

[77] P. Felisberto, O. Rodriguez, P. Santos, E. Ey, and S. Jesus, "Experimental results of underwater cooperative source localization using a single acoustic vector sensor," *Sensors*, vol. 13, no. 7, pp. 8856–8878, Jul. 2013.

[78] F. A. Bozzi and S. M. Jesus, "Vector sensor beam steering for underwater acoustic communications," in *Proceedings of Meetings on Acoustics*, vol. 42. ASA, 2020, p. 070002.

[79] ——, "Joint vector sensor beam steering and passive time reversal for underwater acoustic communications," *IEEE Access*, vol. 10, pp. 66 952–66 960, Jun. 2022.

[80] M. Porter, B. Abraham, M. Badiey, M. Buckingham, T. Folegot, P. Hursky, S. Jesus, B. Kraft, V. McDonald, and W. Yang, "The makai experiment: high-frequency acoustics," in *ECUA*, Carvoeiro, Portugal, 12, p. 10.

[81] H. Schmidt, *OASES - user guide and reference manual*, Online: http://acoustics.mit.edu/faculty/henrik/oases.pdf, Oct. 2019.

[82] T. Yang, "Correlation-based decision-feedback equalizer for underwater acoustic communications," *IEEE J. Oceanic Eng.*, vol. 30, no. 4, pp. 865–880, Oct. 2005.

[83] T. C. Yang, "Measurements of temporal coherence of sound transmissions through shallow water," *The Journal of the Acoustical Society of America*, vol. 120, no. 5, pp. 2595–2614, Nov. 2006.

[84] T. S. Rappaport, *Wireless communications: principles and practice*, 2nd ed., ser. Prentice Hall communications engineering and emerging technologies series. Upper Saddle River, N.J: Prentice Hall PTR, 2002.

[85] P. Felisberto, P. Santos, and S. M. Jesus, "Tracking source azimuth using a single vector sensor," in *2010 Fourth International Conference on Sensor Technologies and Applications*. Venice, Italy: IEEE, Jul. 2010, pp. 416–421.

[86] B. Armstrong, "Directional hydrophones," GeoSpectrum, 10 Akerley Blvd, Unit 19,Dartmouth, Nova Scotia, Canada, B3B 1J4, Technical Document 2018-464, May 2018.

[87] F. A. Bozzi and S. M. Jesus, "Experimental demonstration of a single acoustic vector sensor for janus performance enhancement," in *6th Underwater Communications and Networking Conference*. La Spezia, Italy: IEEE, Sep. 2022, p. 5.

[88] "Anep-87 - digital underwater signalling standard for network node discovery and interoperability," NATO standardization office, Tech. Rep., Mar. 2017.

[89] K. Pelekanakis, "Extending janus for faster bit rates," in *4th JANUS International Workshop*, La Spezia, Italy, May 2018.

[90] F. A. Bozzi and S. M. Jesus, "Vector hydrophone passive time reversal for underwater acoustic communications," in *OCEANS 2022 - Chennai.* Chennai, India: IEEE, Feb. 2022, pp. 1–5.

[91] F. A. Bozzi, F. Zabel, and S. M. Jesus, "Frequency-dependent underwater acoustic communications performance using a pressure-gradient vector sensor," in *Int. Conf. on Acoustics (ICA).* Gyeongju (South Korea): IEEE, Oct. 2022.

[92] P. A. van Walree, F.-X. Socheleau, R. Otnes, and T. Jenserud, "The watermark benchmark for underwater acoustic modulation schemes," *IEEE J. Oceanic Eng.*, vol. 42, no. 4, pp. 1007–1018, Oct. 2017.

[93] C. Chen and A. Ali, "Utilization of underwater particle velocity channels for data transmission: Signals, channels and system performance," in *2012 IEEE International Conference on Communications (ICC).* Ottawa, ON, Canada: IEEE, Jun. 2012, pp. 3816–3820.

[94] E. Zhang and A. Abdi, "Experimental results on underwater communication using vector transducers," in *169th Meeting of the Acoustical Society of America*, Pittsburgh, Pennsylvania, 2015, p. 070011.

[95] G. F. Knoll, *Radiation detection and measurement*, 2nd ed. New York: Wiley, 1989.

[96] S. X. Wang, "Maximum weighted likelihood estimation," Ph.D. dissertation, University of British Columbia, Canada, 2001.

Appendices

Appendix A

Maximum likelihood estimation

The maximum likelihood estimation is used in this work to compensate or balance power noisy channels. Consider a probability density function (PDF) $f(x; \alpha)$, where the objective is to find the unknown parameter α by searching the maximum point of the likelihood function $\zeta(\alpha)$ given by [95, 96]:

$$\zeta(\alpha) = \prod_{i=1}^{L} f(x_i; \alpha). \tag{A.1}$$

Considering x_i Gaussian measures with error σ_i, i.e.,

$$x[l] = A + w[l], \tag{A.2}$$

where A is the parameter to be estimated and $w[l]$ is the Gaussian white noise with variance σ_i^2, the PDF is given by:

$$f(x_i; A) = \frac{1}{(2\pi\sigma_i^2)} exp\left[-\frac{(x_i - A)^2}{2\sigma_i^2}\right]. \tag{A.3}$$

For L samples of x_i, the maximum likelihood function is

$$\zeta(A) = \prod_{i=1}^{L} \frac{1}{\sqrt{2\pi\sigma_i^2}} exp\left[-\frac{(x_i - A)^2}{2\sigma_i^2}\right], \tag{A.4}$$

where taking the natural logarithm becomes

$$p = \sum_{i=1}^{L} \ln \frac{1}{\sqrt{2\pi\sigma_i^2}} - \frac{1}{2}\sum_{i=1}^{L}\left[-\frac{(x_i - A)^2}{\sigma_i^2}\right]. \tag{A.5}$$

The derivative of (A.5) in A gives

$$\frac{\partial p}{\partial A} = \sum_{i=1}^{L} \frac{x_i - A}{\sigma_i^2},$$

(A.6)

which setting equal to zero, it is found the optimum estimated value of A:

$$\hat{A} = \sum_{i=1}^{L} \frac{x_i}{\sigma_i^2} \left(\sum_{i=1}^{L} \frac{1}{\sigma_i^2} \right)^{-1},$$

(A.7)

or,

$$\hat{a}_i = \frac{1}{\sigma_i^2} \left(\sum_{i=1}^{L} \frac{1}{\sigma_i^2} \right)^{-1}.$$

(A.8)

Equations (A.7) or (A.8) show that the optimum parameter is achieved weighting individual measures with their inverted squared errors. One can notice that if all measures have the same error, the optimum estimated value becomes the arithmetical mean.